NUMERICAL INVESTIGATIONS OF THE HYDROGRAPHY, DYNAMICS, AND ICE DISTRIBUTIONS OF CHUKCHI SEA SHELF

By

Kofan Lu M.S.

A Dissertation Submitted in Partial Fulfillment of the Requirements

for the Degree of

Doctor of Philosophy

in

Oceanography: Physical

University of Alaska Fairbanks

August 2019

APPOVED:

Dr. Seth Danielson, Committee Chair
Dr. Thomas Weingartner, Committee Co-Chair
Dr. Kate Hedstrom, Committee Member
Dr. Koji Shimada, Committee Member
Dr. Peter Winsor, Committee Member

Dr. Mark Johnson, Chair
Department of Oceanography
Dr. Bradley Moran, Dean
College of Fisheries and Ocean Sciences
Dr. Michael Castellini,
Dean of the Graduate School

Abstract

Warm, moderately salty Bering Sea Water (BSW) carried into the Chukchi Sea through Bering Strait provides an oceanic heat flux for melting sea ice comparable to that of the solar heat flux. Intrusions of BSW transport heat and nutrients via intrapycnocline eddies vertically beneath the sea ice and laterally across structural fronts near the ice edge, setting up hydrographic features important to ice edge communities and the seasonal evolution of the ice melt-back. However, the intrapycnocline eddy dynamics and associated hydrography near the fronts have not previously been well described or characterized. Three numerical models using the Regional Ocean Model System (ROMS) are integrated to systematically investigate the importance of the intrapycnocline eddy field and the factors that affect its dynamics. The models suggest that the heat transported by eddies depends on frontal stratification, which is influenced primarily by the Bering Strait inflow discharge and salinity. The eddy field is also indirectly modified by the sea surface height, which varies with strong winds. Two frontal zones near the ice edge are identified according to the model-derived hydrographic structures and eddy dynamics: the Shelf Water Transition Zone (SWTZ) and the Melt Water Transition Zone (MWTZ). Improved understanding of these frontal zones will benefit future research of the ice edge ecosystem. Our models show a noticeable effect of strong wind events on ice edge displacement and vertical transports, both of which may be important to primary production in the frontal zones. Changing winds associated with increasing sea surface temperatures could alter the manifestation of the processes highlighted in this study.

Table of Contents

Page

List of Figures

Chapter 1

Chapter 2

Chapter 3

List of Tables

Introduction

The Chukchi Sea continental shelf is an important basin as a linkage between the warm North Pacific and the Arctic Ocean (Woodgate, 2018). Over the Chukchi shelf, the Bering Strait inflow transports heat and nutrients into the Arctic Ocean, influencing not only the summer ice retreat but the water masses that are essential to ecosystems and fisheries (Sigler et al., 2012). As spring evolves into summer, the northern boundary of the Bering Strait inflow forms frontal zones where the dynamics and hydrography are complex and rarely documented. This thesis includes three studies that investigate mechanisms of heat transport and associated dynamical processes on the Chukchi Shelf using the Regional Ocean Modeling System (ROMS) (Shchepetkin and McWilliam, 2005). A set of systematic model tests is designed and analyzed in each study to hierarchically reveal the story of Chukchi shelf ice edge.

The first study, motivated by in situ observations, discusses the heat transport below meltwater plumes by intrapycnocline eddies (Lu et al., 2015). The heat transported northward from Bering Strait is sufficient to melt the entire Chukchi Shelf ice cover in principle. However, the water properties of this inflow and ambient shelf waters combine to reduce the efficiency by which heat is transferred from the Bering Sea Waters to the ice. Melting sea ice naturally stratifies the water column so the initiation of ice melt provides a dampening feedback against the amplifying feedback of the ice-ocean albedo change of ice ablation. Three primary water masses occur: cold (<1°C), low-salinity (<28) meltwater (MW), warm (2-6°C), moderately salty (~30-32) Bering Sea Water (BSW), and near-freezing (-1.5-0°C), salty (>32.5) winter waters (WW) that forms in winter from ice formation over the Bering and Chukchi Seas. A frontal zone occurs where any two of BSW, MW and WW meet. Unless the front is disrupted, the BSW

cannot mix laterally with the other water masses or affect ice melt. Interactions between these water masses are believed to generate baroclinic instabilities suggested from the observations of intrapycnocline eddies (Pickart et al., 2005; Timmermans et al., 2008; Shroyer and Plueddemann, 2012; Lu et al., 2015), which leads to lateral mixing of heat on the Chukchi shelf.

Eddy transport induced by baroclinic instabilities is evaluated from density gradient and lateral variation of pycnocline depths on fronts (Haine and Marshall, 1998; Spall and Chapman, 1998). Both factors correspond to Bering Strait inflow properties and the ice melting rate. In second study, a combination of varied inflow temperatures and discharges are tested in an idealized model with a simplified bathymetry of the Central Channel on Eastern Chukchi Shelf under the influence of representative atmospheric heating from June to August (Lu et al., in review). With varied Bering Strait inflows, associated eddy heat transports are assessed and compared to the mean flow heat transport and seasonal solar radiations.

Baroclinic eddies are accompanied by three-dimensional motions (Spall, 2007; von Appen and Pickart, 2012; Brugler et al., 2014), which influence the vertical transport of heat and nutrients associated with BSW intrusions into the euphotic zone beneath the sea ice. Moreover, circulation on Chukchi Shelf is believed to be bathymetrically steered and dominates the heat transport routes (Winsor and Chapman 2004; Spall, 2007; Weingartner et al., 2013). Dynamics associated with eddies supply the vertical motions that tend to spread the BSW heat eastward across isobaths from the Chukchi Central Channel. This cross-isobath transport is also examined in the second study.

Circulations that dominate heat transport pathway on Chukchi Shelf can also be impacted by wind stress (Weingartner et al., 1998, 2005; Winsor and Chapman 2004; Danielson et al., 2014). However, strong winds from observations are typically short-term events that occur

over a few days to one week. A set of wind forcings are imposed into the model in a third study for 10 days in mid-summer. Flow patterns, ice distributions and frontal stratifications are analyzed with combinations of distinct wind magnitudes and directions. Frontal stratification in particular is highly related to both eddy transport (Thomas et al., 2008; Spall and Thomas, 2016) and vertical mixing (Carmack and Chapman, 2003; Watanabe and Ogi, 2013). These facets link all three studies and are similarly critical to ice retreat. Ice edge displacements are found to migrate to corresponding wind directions due to the drag forces directly from wind (Steele and Ermold, 2015; Serreze et al., 2016). The third study (Lu et al., in review) aims to understand possible variations in the hydrography, ice edge location and frontal exchanges as altered by strong wind events on Chukchi Shelf.

Reference

Brugler, E. T., Pickart, R. S., Moore, G. W. K., Roberts, S., Weingartner, T. J., & Statscewich, H. (2014). Seasonal to interannual variability of the Pacific water boundary current in the Beaufort Sea. *Progress in Oceanography*, 127, 1-20.

Carmack, E., & Chapman, D. C. (2003). Wind-driven shelf/basin exchange on an Arctic shelf: The joint roles of ice cover extent and shelf-break bathymetry. *Geophysical Research Letters*, 30(14).

Danielson, S. L., Weingartner, T. J., Hedstrom, K. S., Aagaard, K., Woodgate, R., Curchitser, E., & Stabeno, P. J. (2014). Coupled wind-forced controls of the Bering–Chukchi shelf circulation and the Bering Strait throughflow: Ekman transport, continental shelf waves, and variations of the Pacific–Arctic sea surface height gradient. *Progress in Oceanography*, 125, 40-61.

Haine, T. W., & Marshall, J. (1998). Gravitational, symmetric, and baroclinic instability of the ocean mixed layer. *Journal of Physical Oceanography*, *28*(4), 634-658.

Lu, K., Weingartner, T., Danielson, S., Winsor, P., Dobbins, E., Martini, K., & Statscewich, H. (2015). Lateral mixing across ice meltwater fronts of the Chukchi Sea shelf. *Geophysical Research Letters*, *42*(16), 6754-6761.

Lu, K., Danielson, S., Hedstrom, K., & Weingartner, T. (in review). Assessing the role of oceanic heat fluxes on ice ablation on the Chukchi Sea Shelf. *Progress in Oceanography*.

Lu, K., Danielson, S., & Weingartner, T. (in review). Impacts of short-term wind events on Chukchi hydrography and sea ice retreat. *Deep Sea Research Part II: Topical Studies in Oceanography*.

Pickart, R. S., Weingartner, T. J., Pratt, L. J., Zimmermann, S., & Torres, D. J. (2005). Flow of winter-transformed Pacific water into the Western Arctic. *Deep Sea Research Part II: Topical Studies in Oceanography*, *52*(24-26), 3175-3198.

Serreze, M. C., Crawford, A. D., Stroeve, J. C., Barrett, A. P., & Woodgate, R. A. (2016). Variability, trends, and predictability of seasonal sea ice retreat and advance in the Chukchi Sea. *Journal of Geophysical Research: Oceans*, 121(10), 7308-7325.

Shchepetkin, A. F., & McWilliams, J. C. (2005). The regional oceanic modeling system (ROMS): a split-explicit, free-surface, topography-following-coordinate oceanic model. *Ocean Modelling*, 9(4), 347-404.

Shroyer, E. L., & Plueddemann, A. J. (2012). Wind-driven modification of the Alaskan coastal current. *Journal of Geophysical Research: Oceans*, 117(C3).

Sigler, M. F., Kuletz, K. J., Ressler, P. H., Friday, N. A., Wilson, C. D., & Zerbini, A. N. (2012). Marine predators and persistent prey in the southeast Bering Sea. *Deep Sea Research Part II: Topical Studies in Oceanography*, 65, 292-303.

Spall, M. A. (2007). Circulation and water mass transformation in a model of the Chukchi Sea. *Journal of Geophysical Research: Oceans*, *112*(C5).

Spall, M. A., & Chapman, D. C. (1998). On the efficiency of baroclinic eddy heat transport across narrow fronts. *Journal of Physical Oceanography*, *28*(11), 2275-2287.

Spall, M. A., & Thomas, L. N. (2016). Downfront winds over buoyant coastal plumes. *Journal of Physical Oceanography*, 46(10), 3139-3154.

Steele, M., & Ermold, W. (2015). Loitering of the retreating sea ice edge in the Arctic Seas. *Journal of Geophysical Research: Oceans*, *120*(12), 7699-7721.

Timmermans, M. L., Toole, J., Krishfield, R., & Winsor, P. (2008). Ice-Tethered Profiler observations of the double-diffusive staircase in the Canada Basin thermocline. *Journal of Geophysical Research: Oceans*, 113(C1).

Thomas, L. N., Tandon, A., & Mahadevan, A. (2008). Submesoscale processes and dynamics. *Ocean Modeling in an Eddying Regime*, 17-38.

von Appen, W. J., & Pickart, R. S. (2012). Two configurations of the western Arctic shelfbreak current in summer. *Journal of Physical Oceanography*, *42*(3), 329-351.

Watanabe, E., & Ogi, M. (2013). How does Arctic summer wind modulate sea ice-ocean heat balance in the Canada Basin?. *Geophysical Research Letters*, 40(8), 1569-1574.

Weingartner, T. J., Cavalieri, D. J., Aagaard, K., & Sasaki, Y. (1998). Circulation, dense water formation, and outflow on the northeast Chukchi shelf. *Journal of Geophysical Research: Oceans*, 103(C4), 7647-7661.

Weingartner, T., Aagaard, K., Woodgate, R., Danielson, S., Sasaki, Y., & Cavalieri, D. (2005). Circulation on the north central Chukchi Sea shelf. *Deep Sea Research Part II: Topical Studies in Oceanography*, *52*(24-26), 3150-3174.

Weingartner, T., Dobbins, E., Danielson, S., Winsor, P., Potter, R., & Statscewich, H. (2013). Hydrographic variability over the northeastern Chukchi Sea shelf in summer-fall 2008–2010. *Continental Shelf Research*, *67*, 5-22.

Winsor, P., & Chapman, D. C. (2004). Pathways of Pacific water across the Chukchi Sea: A numerical model study. *Journal of Geophysical Research: Oceans*, *109*(C3).

Woodgate, R. A. (2018). Increases in the Pacific inflow to the Arctic from 1990 to 2015, and insights into seasonal trends and driving mechanisms from year-round Bering Strait mooring data. *Progress in Oceanography*, 160, 124-154.

Chapter 1

Lateral mixing across ice meltwater fronts of the Chukchi Sea shelf

K. Lu[1], T. Weingartner[1*], S. Danielson[1], P. Winsor[1], E. Dobbins[1], K. Martini[2,3], and H. Statscewich[1]

[1]School of Fisheries and Ocean Sciences, University of Alaska, Fairbanks, Alaska, USA.

[2]Joint Institute for the Study of the Atmosphere and Oceans, University of Washington, Seattle, Washington, USA.

[3]Pacific Marine Environmental Laboratory, NOAA, Seattle, Washington, USA.

*Corresponding author's e-mail: tjweingartner@alaska.edu

Manuscript #: 2015GL063500

Revised for submission to *Geophysical Research Letters*

May, 2015

Abstract

Summer and fall hydrographic sections in the northeastern Chukchi Sea frequently capture 5 – 20 m thick intrapycnocline lenses or horizontal plumes of warm, moderately salty summer Bering Sea Water flowing northward from Bering Strait. These features occur within the shallow (~20 m depth) pycnocline separating cold, dilute, surface meltwater from near-freezing, salty, winter-formed waters beneath the pycnocline. An idealized numerical model suggests that the features arise from eddies and meanders generated by instability of the surface front separating meltwater from Bering Sea Water. Warm Bering Sea Water is transported across the front and into the pycnocline by the cross-frontal velocities associated with the instabilities. The accompanying lateral eddy heat fluxes may be important both in summer for promoting ice melt and in fall by delaying the onset of ice formation over portions of this shelf. Lateral heat flux magnitudes depend upon the stratification of the Bering Sea Water.

1. Introduction

Summer and fall water masses on the Chukchi Sea shelf include cool, dilute waters derived from ice melt (MW); near-freezing, saline winter waters (WW) formed during the previous winter on the Chukchi/Bering shelves; and warmer, Pacific-derived water masses having salinities between those of the MW and the WW. These include fresh, warm Alaskan Coastal Water (ACW), derived from riverine sources south of Bering Strait [Aagaard et al., 2006], and cooler, saltier Bering Sea Water (BSW). Both ACW and BSW contain substantial heat [Woodgate et al., 2012] and flow northward from Bering Strait across the Chukchi shelf along bathymetrically controlled routes [Winsor and Chapman, 2004; Weingartner et al., 2005; Woodgate et al., 2005; Spall, 2007]: Herald Valley in the western Chukchi, the Central Channel aligned meridionally west of Hanna Shoal (Figure 1a), and Barrow Canyon, which parallels the northwestern Alaskan coast and terminates on the continental slope (Figure 1a). The pathways are evident in the shelf-wide distribution of summer sea ice concentrations (Figure 1b) and lead to prominent embayments separated by broad tongues of ice [Martin and Drucker, 1997]. This pattern suggests that the Pacific waters exert a thermodynamic and/or dynamic influence on ice retreat, although a mechanistic description of these processes has not been offered. Through summer and fall, the Pacific waters are found adjacent to MW and WW [Weingartner et al., 2005, Weingartner et al., 2013] and often form surface and subsurface fronts. Each of these water masses interacts with one another and the ice to produce the horizontally- and vertically-structured complex of water masses that exit the northeast Chukchi Sea through Barrow Canyon [Pickart et al., 2005; Shroyer and Plueddemann, 2012]. This outflow and its potential vorticity (PV) structure affect eddy formation [Spall et al., 2008; von Appen and Pickart, 2012] and upwelling [Brugler et al., 2014] along the shelfbreak. Herein, observations and an idealized

numerical model suggest that lateral mixing and stirring of heat and salt on the Chukchi shelf is a consequence of baroclinic instability of the MW/BSW fronts. The instabilities promote lateral fluxes of BSW into the pycnocline separating MW and WW.

2. Observations

Figure 1a is a satellite-derived composite of the sea surface temperature (SST; 21 August 2012) and the bathymetry of the northeast Chukchi Sea. The SST distribution shows cold water (and ice) extending northward from about 71.5 °N, over and to the north and east of Hanna Shoal. Warmer water prevails on the shelf south of 71.5 °N and in two tongues protruding northward in the Central Channel and northeastward in Barrow Canyon. Figure 1b is a Moderate Resolution Imaging Spectroradiometer (MODIS) satellite image of the ice distribution on 23 July 2012 on the northeastern shelf. A large amount of ice is centered over, and to the northwest of, Hanna Shoal. Ice concentrations diminish to the east and northeast of the Shoal and open water is present ~100 km to the south. Lower ice concentrations are evident west of the Shoal in the Central Channel. The southern boundary of the ice edge contains meanders with wavelengths of ~20 km. The ice distribution on the Shoal is common in summer and is ascribed to trapping by a Taylor column [Martin and Drucker, 1997] or grounded aggregations of ice. Even when ice is absent, MW is often associated with the Shoal region and may remain there through early fall [Weingartner et al., 2013]. By mid-September 2012 and 2013, the ice had disappeared completely from the Shoal.

Intrapycnocline signatures of BSW were opportunistically observed on three CTD transects completed between August and September in 2012 and 2013 (T1, T2, and T3 in Figure 1a). Although these sections did not extend into the ice, the sampling captured the surface MW

(that either was advected from the Shoal region or was a remnant of previous melting) and the MW/BSW front. Transects T1 (August 2012) and T2 (August 2013) were constructed from 1 dbar-averaged CTD data obtained during the Chukchi Sea Ecosystem Studies Program interdisciplinary cruises and are derived from stations at a nominal spacing of 15 km. Transect T3 (September 2013) was obtained by a towed CTD-vehicle (Acrobat) that yo-yoed between the surface and bottom. Acrobat data was averaged into 1-dbar bins to produce water column profiles with a nominal 250 m horizontal spacing. In 2012, the winds were from the south at ~5 m s^{-1}. In 2013, the winds at the time of the transect occupations were northeasterly between 5 – 10 m s^{-1}, which is typical for the region. Current data are not available from the shipboard sampling, but previous measurements [Weingartner et al., 2005; Weingartner et al., 2013] indicate that the mean August - September flow in the southern portion of the Central Channel is northward at ~0.05 m s^{-1}, while along the southern half of T1 and T2, Central Channel derived-waters flow eastward at ~0.05m s^{-1}. This eastward flow reverses when westward winds exceed ~6 m s^{-1}. Figure 2 shows vertical sections of potential temperature (θ) and salinity (S) overlain with σ_θ contours for each transect.

Transect T1 (2012) contained cold (θ~0 – 1°C), fresh (S<30) MW in the upper 15 m north of km 75. A strong, thin halocline at ~15 m depth separates the surface MW from colder (θ <0.5°C) and saltier (S≥32.5) WW in the lower half of the water column. Along the southernmost 50 km of T1, BSW occupied most of the water column with θ ranging from 1 to 5°C and S between 30.5 and 32.5. At about km 75, the BSW and MW are separated by a surface front, whose structure is likely not well-resolved by the 15-km station spacing. Of interest is the 125-km long tongue of 1 - 2°C water extending northward from the front between 10 and 15 m depth. Note that the 30 and 32 isohalines are vertically distended, which suggests an anticyclonic eddy

near the tongue's origin at ~km 75.

Transects T2 (2013) and T1 both have a strong MW/BSW front in the upper 15 m, a pycnocline centered at ~20 m depth, and stratification that increases from south to north. T2 differs from in T1 in that the bottommost 20 m over the entire transect mainly consists of WW. Two intrapycnocline features are evident. One is a lens or filament of 2 – 4°C water located at the base of the front and coincident with vertical spreading of the 30 and 32 isohalines. The other is indicated by the 4°C water at the northern end of T2, which may have derived from the Central Channel [Weingartner et al., 2005]. Between these features, and within the pycnocline, the water is warmer than either MW or WW and occupies the same θ-S space as BSW so this is a consequence of lateral influxes and not vertical mixing between MW and WW.

Transect T3 (2013), obtained from the Acrobat along the northwest side of Hanna Shoal, suggests four lenses within the pycnocline and between the 30 – 32 isohalines, with temperatures of 2 – 4°C. Note that T3 most likely parallels the front delimiting BSW as it flows northward in the Central Channel (cf. Figure 1a, although this SST image is from 2012 because heavy cloud cover precluded obtaining imagery in 2013). As suggested by the model results presented later, the spacing and number of lenses in T3 may be a signature of intrapycnocline eddies generated by instabilities along the length of this front. Each intrusion is 10 – 15 m thick with a horizontal length-scale (L_I) of 10 – 20 km.

These sections suggest that north of the MW/BSW front, the pycnocline separating MW and WW hosts thin (~10 m) layers of BSW. The high-resolution Acrobat data (T3) indicates that these are discrete lenses and the vertical stretching of the isopycnals about the lenses implies that the features are anticyclonic. The more widely-spaced CTD stations (T1 and T2) suggest lenses

and/or subducted plumes although here the inferred structure might be biased by contouring given the station spacing. Along all sections the internal deformation radius (R_{bc}) is ~5 – 7 km based on the thickness of the upper layer of MW and the Coriolis parameter, $f = 1.38 \times 10^{-4}$ s^{-1} evaluated at 71.5 °N. For the T3 features, the Burger Number ($= R_{bc}^2 / L_I^{\,2}$) is O(10^{-1}).

3. Model Results

Meltwater and ice edge fronts are often baroclinically unstable [Muench, 1990], which is consistent with the 20-km wavelength along the ice edge (Figure 1b) for an R_{bc} of ~6 km. We hypothesize that the subducting tongues and lenses arise due to baroclinic instability of the MW-WW-BSW front. We test this hypothesis using the Regional Ocean Modeling System (ROMS) configured on an *f*-plane for a 150 km x 150 km channel, with a constant depth of 50 m. The meridional (y) walls are impermeable, the zonal (x) boundaries are periodic, the horizontal and vertical resolutions are 500 m and 1 m, respectively, and the integration time step is 1 min. Bottom friction is quadratic with a drag coefficient of $C_D = 5 \times 10^{-4}$ m s^{-1}. The vertical diffusivity is 5×10^{-6} m^2 s^{-1} and the horizontal diffusivity was set to minimal values sufficient to suppress numerical noise. We conducted two experiments that differed only with respect to their initial density (ρ) distribution (Figure 3f). Model 1 (M1) mimics the hydrography of transect T1 by initially having a strongly stratified 2-layer structure confined to the northern half ($y > 75$ km) of the domain. This includes a front separating MW in the upper 20 m and WW in the lower 30 m from a 50-m deep layer of unstratified BSW in the southern half of the channel (km 0 – 75). The MW properties are $\theta = 0$ °C, S = 28, and $\rho = 1022.5$ kg m^{-3}. BSW properties are $\theta = 5$°C and S = 30 and, $\rho = 1024$ kg m^{-3}, and the WW properties are $\theta = 0$ °C, S = 33 and $\rho = 1026.5$ kg m^{-3}. The water properties in Model 2 (M2) are identical to those in M1, but the spatial structure

differs and mimics section T2 (Figure 2). In M2, the 2-layer structure consists of WW extending across the entire width of the channel. MW occupies the upper 20 m over the northern half of the channel and BSW occupies the upper 20 m over the southern half. In each model the initial R_{bc} ~6 km given the distribution of MW and WW.

To initiate the instabilities, we displaced the front with perturbation amplitudes of 0.5 km for random forcing and 1 and 2 km for sinusoidal forcing. The sinusoids had wavelengths of 20, 40 and 80 km and were applied individually or by superposition. The results were similar to one another and we show those using a single sinusoid (1-km amplitude and a 20-km wavelength) as these conditions case yielded intermediate values for the lateral heat fluxes and bolus velocities discussed later. Both models were run for 30 days. We evaluated time series of PV = $(\zeta + f)/h$ where h is the layer thickness between $23 \leq \sigma_\theta \geq 25$ kg m^{-3} and ζ is the relative vorticity based on the layer-averaged velocities. The evolution of the PV fields, normalized by the initial PV = $f/50m$, is shown at 4-day intervals between Day 8 and 24 for M1 and M2 (Figures S1 and S2, respectively). In both models meanders develop after a few days, evolving into cyclonic and anticyclonic eddies and filaments as the collapse of the frontal region progresses in a manner similar to that described by Manucharyan and Timmermans [2013]. Mesoscale motions approach the meridional boundaries in M1 by Day 25, but for M2, they remain within 25 km of the original frontal position at this time. Figures 3a – c show the temperature and velocity fields on Day 25 at 0, 20, and 38 m for M1. Figures 3d and e show the same fields at 0 and 20 m only for M2 because temperature remains constant and motions are feeble in the WW layer. Both the temperature and PV maps show eddy-like features with diameters of ~20 km and filaments that can be long (~100km) but narrow (~5 – 10 km). Mesoscale velocities range from 0.05 – 0.25 m s^{-1} and are generally higher for M1 than for M2 presumably because of the greater available

potential energy of M1 compared to M2 [Gill, 1982]. In both models, cyclonic eddies carry MW southward into the region initially occupied by BSW, while cyclonic and anticyclonic eddies transport BSW northward beneath the front and into the pycnocline. In M1, the eddies transport WW southward across the front into the region initially occupied by BSW.

Vertical cross-channel sections of temperature and salinity for M1 (Figures 4a, b) and M2 (Figures 4d, e) were constructed on Day 25 along km 84 (indicated in Figure 3f). The sections show a series of warm lenses (associated with the eddies and filaments of Figure 3) penetrating laterally along the pycnocline between MW and WW. In general agreement with the observations, the features vary in thickness from 5 - 25 m and in width from ~5 - 20 km yielding Burger numbers of $O(10^{-1})$.

The instantaneous lateral heat fluxes accompanying the BSW features were evaluated by Reynolds' decomposition of the time-varying cross-channel heat flux. For a given along-channel position, x_p, this flux varies with time (t) and cross-channel location (y) as:

$$\rho C_p[v(y,t)\theta(y,t)h(y,t)]_{x_p} = \rho C_p\left[\bar{v}\left(\bar{\theta}\,\bar{h} + \bar{\theta}h' + \theta' h' + \theta'\bar{h}\right) + v'\left(\underbrace{\overline{\theta h}}_{\text{I}} + \underbrace{\bar{\theta}h'}_{\text{II}} + \underbrace{\theta'\bar{h}}_{\text{III}} + \underbrace{\theta' h'}_{\text{IV}}\right)\right]_{x_p}$$

where C_p is the specific heat at constant pressure, v the cross-channel velocity, and h the intrusion thickness. Variables with an overbar denote the along-channel mean (computed at each time step along y = 90 km; 15 km northward of the initial frontal position) and primes denote deviations from the means. The fluxes are computed between the $23 \leq \sigma_\theta \leq 25$ kg m^{-3} isopycnal layer because these isopycnals encompass the bulk of the BSW (Figure 4) contained within the features. The first four terms describe fluxes due to the mean cross-channel flow $\left(\bar{v}\right)$ and vanish

while terms *I* – *IV* are the heat fluxes associated with the eddy velocities (v'). These fluxes arise from features having the mean heat content ($\overline{h}\overline{\theta}$, *I*), anomalous heat contents due to thickness (h', *II*) and temperature (θ', *III*) anomalies, and the product of these two anomalies ($h'\theta'$, *IV*). For both models, terms *I* – *IV* have comparable magnitude so no single term dominates. A maximum eddy heat flux of ~2 x 10^7 W m^{-1} occurs in the unstratified model (M1) whereas for the stratified model (M2) the maximum is ~4 x 10^6 W m^{-1}.

We computed the mean daily heat content (Q) within the box encompassing the entire length and depth of the channel between the northern wall and y = 90 km, (cf. Figure 3f). Centered-time differences of Q yield the mean daily heating rate, dQ/dt (Figure 4c and f). For M1, dQ/dt increases monotonically from 0 to ~320 W m^{-2} between Days 5 and 16 before decreasing to ~30 W m^{-2} by Day 20 and then increasing again until Day 25. For M2, dQ/dt is smaller; it attains a maximum of ~75 W m^{-2} on Day 8, collapses to ~0 W m^{-2} between Days 11 and 15, and then increases to ~40 W m^{-2} thereafter. The mean northward heat fluxes between Days 5 and 25 are ~110 W m^{-2} for M1 and ~20 W m^{-2} for M2. Figures 4c and f also include time series of the eddy-induced or "bolus velocity", $v^* = \overline{h'v'}/\overline{h}$; the isopycnal component of the secondary circulation due to flattening of the isopycnals engendered by instabilities [Lee et al., 1997]. The dQ/dt and v^* time series coincide with one another as expected if the instabilities are the source for the lateral heat flux. Here the overbar signifies the zonal average at each time step along y = 90 km and h is the varying thickness of the $23 \leq \sigma_\theta \leq 25$ kg m^{-3} isopycnal layer.

For the more energetic M1, v^* varies from ~0 to 0.04 m s^{-1} between Days 5 and 25 for an average value of ~0.02 m s^{-1}, whereas in M2 v^* is ~0.01 m s^{-1} and its average is 0.003 m s^{-1}. In both models the ratio of the average dQ/dt to the average v^* is similar.

4. Discussion

Observations indicate that a common hydrographic feature of the Chukchi Sea shelf in summer and fall are lenses or tongues of warm, moderately salty Bering Sea Water (BSW) penetrating the pycnocline separating cold, dilute surface meltwaters (MW) from cold, salty winter waters (WW) in the lower half of the water column. Idealized model results suggest that these features originate from baroclinic instabilities of the MW/BSW fronts. Such fronts are ubiquitous aspects of the ice edge of the Chukchi shelf in summer [Paquette and Bourke, 1981] and can be present through fall [Weingartner et al., 2013]. Consequently, the intrapycnocline features might be an important mechanism on the Chukchi shelf for lateral transport and stirring that lead to the spectrum of shelf water types that eventually feed the Arctic Ocean. Moreover, intrapycnocline fluxes of BSW represent a potential heat and salt source to the surface mixed layer if turbulent mixing is sufficiently strong.

Kawaguchi et al. [2015] estimated vertical eddy diffusivities, K_T, on the Chukchi shelf in September and found that K_T varied with wind speed from $10^{-4} - 10^{-5}$ m^2 s^{-1} in the strongly stratified subsurface waters between 20 – 30 m depth. For $K_T = 10^{-5}$ m^2 s^{-1} (twice the background vertical eddy diffusivity used in our model runs) and $\partial\theta/\partial z = 0.3$°C m^{-1} the vertical eddy heat flux is 12 W m^{-2}. These vertical heat fluxes will cause lenses with temperatures of 2°C and thicknesses of 5 – 10 m to decay in 1 – 3 months. For $K_T = 10^{-4}$ m^2 s^{-1} the vertical eddy heat flux is ~120 W m^{-2}, implying that such features would erode in a few days.

Our results have implications on summer ice retreat and fall ice formation on the Chukchi shelf. Retreat commences in May with the annual increase in heat transport through Bering Strait [Woodgate et al., 2012] and progresses northward across the shelf in the form of ice-edge

embayments along the bathymetrically-defined flow pathways [Paquette and Bourke, 1981; Martin and Drucker, 1997]. The embayments presumably form as a consequence of both advection of ice by the currents and through subsurface melting as the warmer, but denser, Bering waters flow beneath the ice and surface meltwater. The oceanic heat flux convergence may be large so that heat fluxes associated with the mean flow (e.g., the first four terms in Eq. 1) are likely important in forming the embayments. Weingartner et al. [2005] estimated heat flux convergences of ~150 W m^{-2} in the Central Channel where the flow is steadily northward at ~0.10 m s^{-1} from May - July. The embayments effectively increase the length of the marginal ice zone and associated fronts, so that the mid-summer ice edge extends for more than 1000 km across the Chukchi shelf. Presumably these fronts are subject to instabilities akin to those modeled here.

For the stratified and unstratified models, the lateral eddy heat fluxes averaged ~20 – 110 W m^{-2}, respectively. If the latter flux is made available to the underside of the ice, it would result in an ablation rate of ~0.03 m day^{-1}. These fluxes depend upon the temperature of the BSW adjacent to the ice edge front, which can vary from 2 – 9°C within a few kilometers of the ice edge [Paquette and Bourke, 1981]. Measurements by the Department of Energy's Atmospheric Radiation Measurement site in Barrow Alaska indicate a June-July mean net daily shortwave radiation rate of ~200 W m^{-2}. For albedo values of ~0.6 within the marginal ice zone [Lindsay and Rothrock, 1994; Fetterer and Untersteiner, 1998], the net solar heat flux to the ice is ~120 W m^{-2}. Thus the lateral heat fluxes represent a potentially important heat source for the ice within several tens of kilometers of the ice edge. In ice-free regions from August through early October, the lateral heat flux magnitudes are comparable to or greater than the atmospheric heat fluxes [Weingartner et al., 2013]. In August the modeled lateral heat fluxes are comparable to the net

atmospheric heating rate of ~80 W m^{-2} while from September through early October the lateral heat fluxes would buffer the 50 – 120 W m^{-2} heat lost to the atmosphere and therefore delay the onset of ice formation.

Our results suggest that frontal instabilities may play an important role in summer ice melt on the Chukchi shelf. We have, however, considered only two simple characterizations of the stratification and frontal structure and ignored the influence of bottom topography, mean flows, and winds. Over the northeastern Chukchi shelf, winds generally have a westward component and thus blow in the same direction as baroclinic jets in thermal wind balance along zonally-oriented ice edges (cf. Figure 1b). Such winds should enhance intrapycnocline eddy formation [Thomas, 2008]. Also ignored are the stratifying effects of a surface buoyancy flux from melting ice, which will suppress turbulent mixing. Hence the connection between the subsurface lateral eddy heat fluxes and vertical mixing of this heat into the surface layer remains unclear and deserves further investigation. Importantly, the model results indicate that the vigor of the frontal instabilities and lateral heat fluxes depend upon the stratification properties of the BSW. This stratification is contingent upon the rate of the northward retreat of WW and the properties of the BSW. The latter are a function of processes occurring far south of the ice edge and depend upon the integrated effects of air-sea heat exchange and the mixing history of the BSW as it flows northward across the Bering and Chukchi shelves.

Acknowledgements

The CTD data sets used in this paper are archived with the authors and with NODC, the Alaska Ocean Observing System (AOOS), and the BOEM. This research was funded by the BOEM, US Dept. of Interior, and ConocoPhillips Alaska Company, Shell Exploration and Production Company, and Statoil USA E+P, Inc. We thank the many people who assisted in various phases of the project, especially A. Macrander, C. Rea, S. Eldøy, R. Day, J. Burns, S. Wisdom, and the officers and crews of the R/V *Westward Wind* and the R/V *Norseman II*. Computing time was provided by the Arctic Supercomputer Center at the University of Alaska. Atmospheric solar radiation measurements were provided by the DOE-ARM facility in Barrow. Figure 1 is from the Rapid Response imagery from the Land Atmosphere Near-real time Capability for EOS (LANCE) system operated by the NASA/GSFC/Earth Science Data and Information System (ESDIS) with funding provided by NASA/HQ. The MODIS Aqua Level 3 Thermal IR Daily 4km data were obtained through the online PO.DAAC Live Access Server (LAS) at the Physical Oceanography Distributed Active Archive Center (PO.DAAC), NASA Jet Propulsion Laboratory, Pasadena, CA. http://thredds.jpl.nasa.gov/las/getUI.do. Comments by Knut Aagaard, Harper Simmons, Mark Johnson, and the reviewers improved the substance and clarity of the paper.

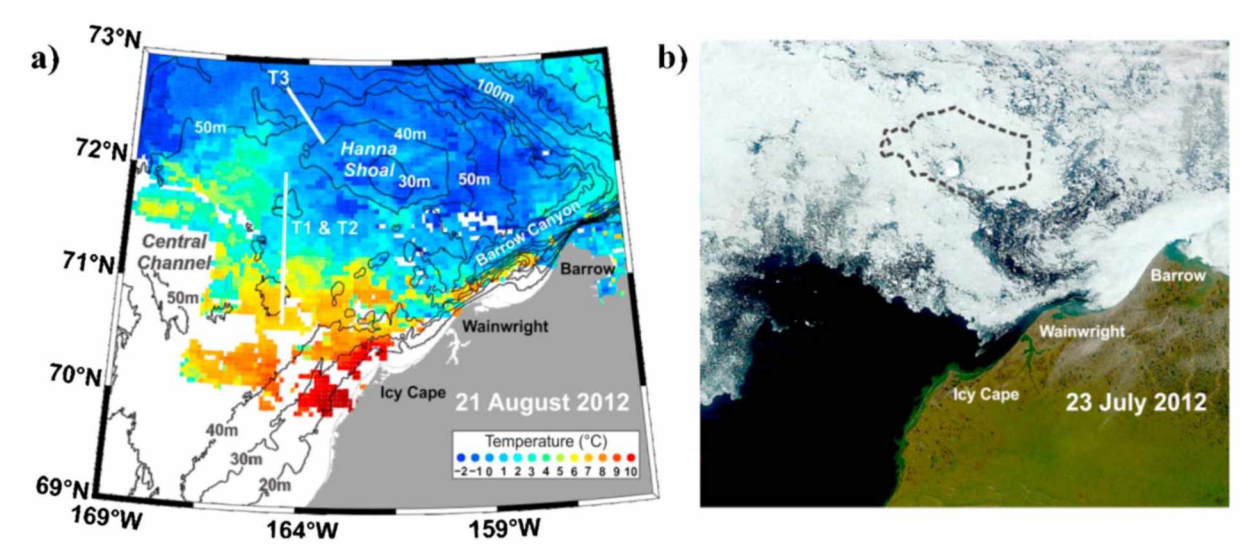

Figure 1. a) A MODIS thermal image of sea surface temperature from 21 August 2012 overlain with isobaths and locations in the northeastern Chukchi Sea. Transects T1 (2012), T2 (2013), and T3 (2013) are indicated by white solid lines. b) Sea ice distribution on 23 July 2013 showing the heavy ice concentrations over Hanna Shoal (where the black, dashed curve denotes the 40 m isobath).

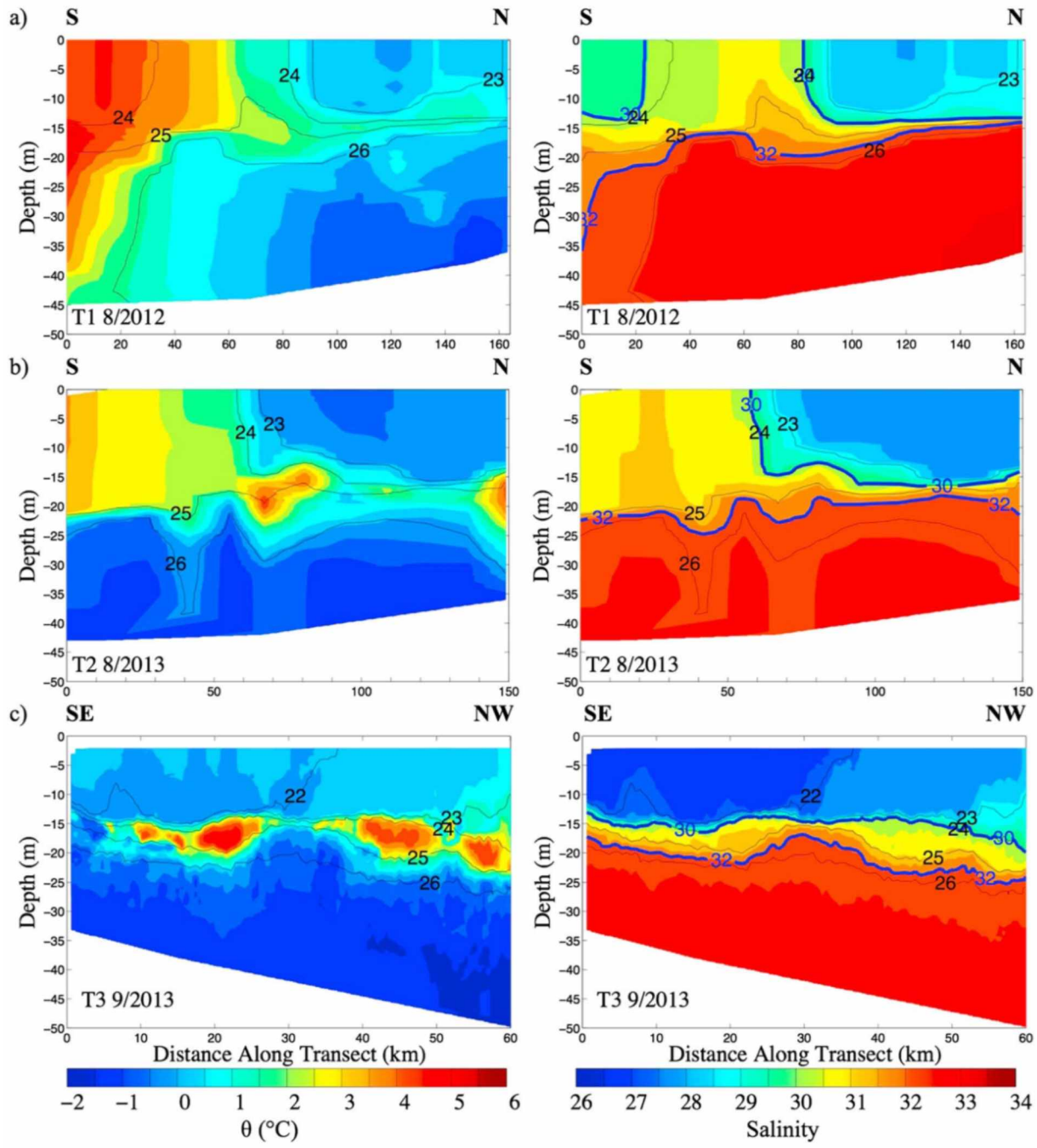

Figure 2. Vertical sections of temperature and salinity for a) T1, b) T2, and, c) T3 overlain with σ_θ contours. The 30 and 32 isohaline contours on the salinity sections are highlighted and labeled.

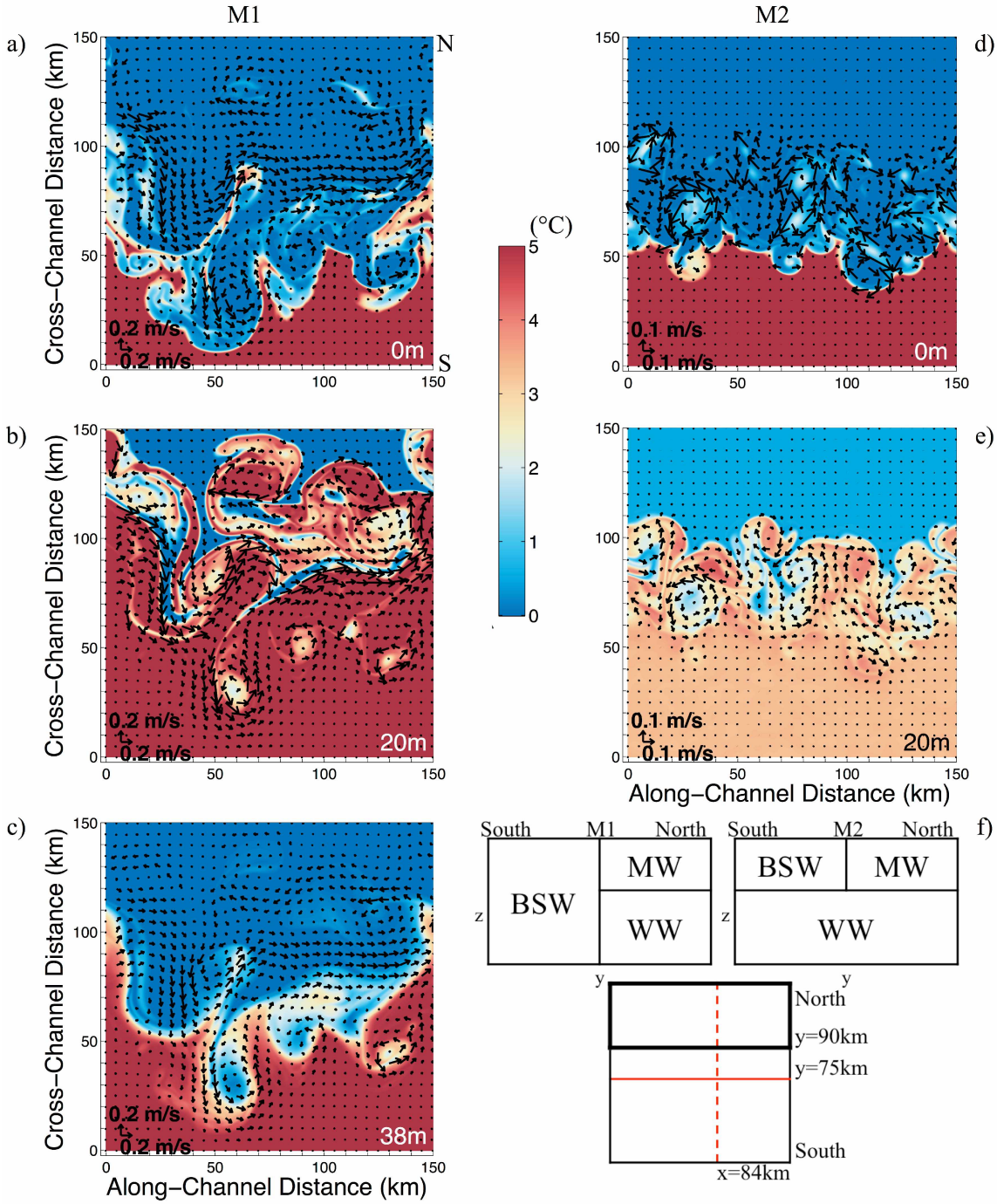

Figure 3. Plan views of temperature and velocity vectors from models M1 (left) and M2 (right) on Day 25 at the depths indicated. Figure 3f shows the initial stratification conditions for M1 and

M2. Note that the velocity scales differ between M1 and M2. The initial location of the front (red line) is at y = 75 km and the dashed red line at x = 84 km is the location of the model cross-sections in Figures 4a-d. The black rectangle outlines the model domain over which the heat fluxes (Figure 4c and f) were computed.

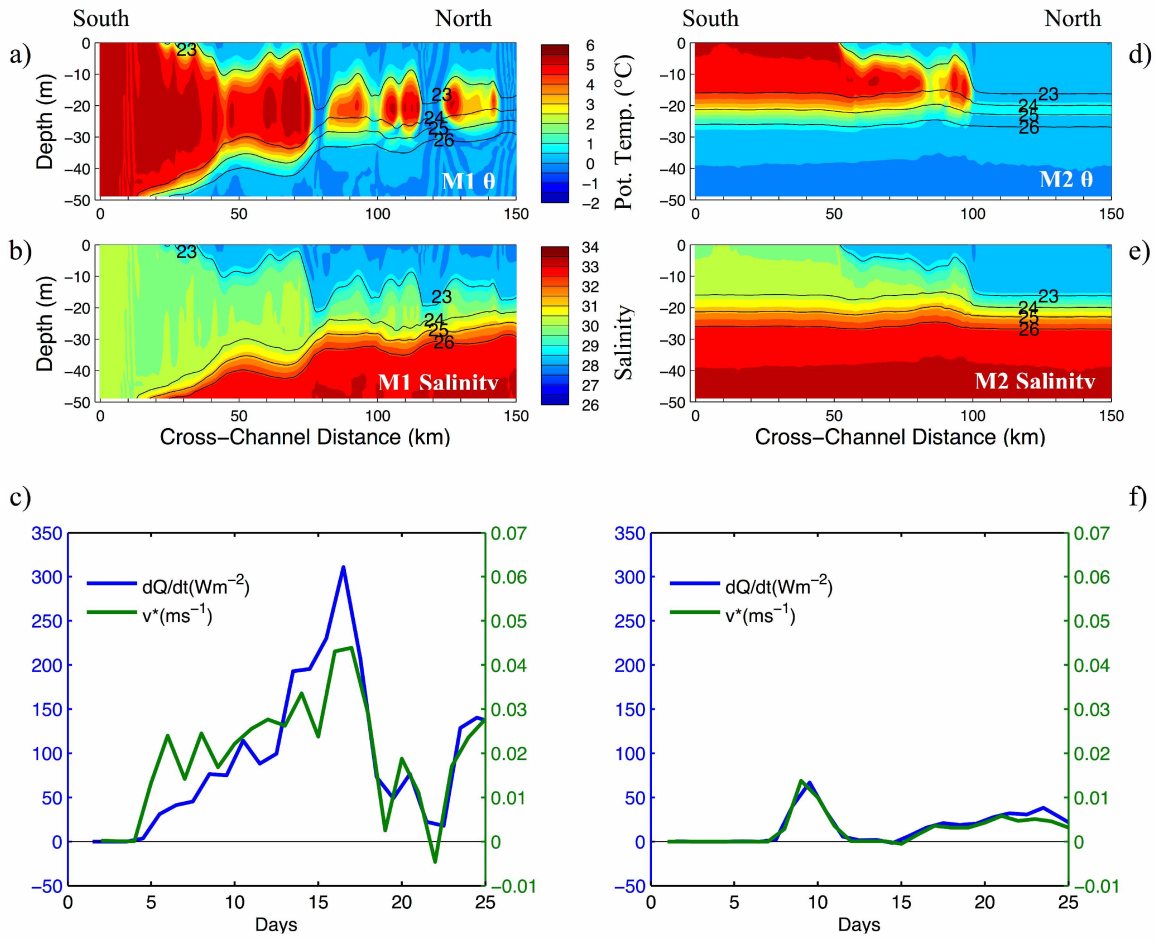

Figure 4. Cross-channel sections of temperature and salinity, overlain with σ_θ contours, at along-channel distance km 84 from M1 (a and b) and M2 (c and d) on Day 25. Panels c and f show the mean daily heating rate (dQ/dt) and the bolus velocity (v^*) as a function of time for M1 and M2, respectively.

Reference

Aagaard, K., Weingartner, T. J., Danielson, S. L., Woodgate, R. A., Johnson, G. C., & Whitledge, T. E. (2006). Some controls on flow and salinity in Bering Strait. *Geophysical Research Letters*, 33(19).

Brugler, E. T., Pickart, R. S., Moore, G. W. K., Roberts, S., Weingartner, T. J., & Statscewich, H. (2014). Seasonal to interannual variability of the Pacific water boundary current in the Beaufort Sea. *Progress in Oceanography*, 127, 1-20.

Fetterer, F., & Untersteiner, N. (1998). Observations of melt ponds on Arctic sea ice. *Journal of Geophysical Research: Oceans*, 103(C11), 24821-24835.

Gill, A. E. (1982). Atmosphere-Ocean dynamics (International Geophysics Series). *Academic Press*, 662 pp.

Kawaguchi, Y., Nishino, S., & Inoue, J. (2015). Fixed-point observation of mixed layer evolution in the seasonally ice-free Chukchi Sea: Turbulent mixing due to gale winds and internal gravity waves. *Journal of Physical Oceanography*, 45(3), 836-853.

Lindsay, R. W., & Rothrock, D. A. (1994). Arctic sea ice albedo from AVHRR. *Journal of Climate*, 7(11), 1737-1749.

Manucharyan, G. E., & Timmermans, M. L. (2013). Generation and separation of mesoscale eddies from surface ocean fronts. *Journal of Physical Oceanography*, 43(12), 2545-2562.

Martin, S., & Drucker, R. (1997). The effect of possible Taylor columns on the summer ice retreat in the Chukchi Sea. *Journal of Geophysical Research: Oceans*, 102(C5), 10473-10482.

Muench, R. D. (1990). A review of mesoscale processes in the polar oceans. *Polar Oceanography*, 223-285.

Paquette, R. G., & Bourke, R. H. (1981). Ocean circulation and fronts as related to ice melt-back in the Chukchi Sea. *Journal of Geophysical Research: Oceans*, 86(C5), 4215-4230.

Pickart, R. S., Weingartner, T. J., Pratt, L. J., Zimmermann, S., & Torres, D. J. (2005). Flow of winter-transformed Pacific water into the Western Arctic. *Deep Sea Research Part II: Topical Studies in Oceanography*, 52(24-26), 3175-3198.

Shroyer, E. L., & Plueddemann, A. J. (2012). Wind-driven modification of the Alaskan coastal current. *Journal of Geophysical Research: Oceans*, 117(C3).

Spall, M. A. (2007). Circulation and water mass transformation in a model of the Chukchi Sea. *Journal of Geophysical Research: Oceans*, 112(C5).

Spall, M. A., Pickart, R. S., Fratantoni, P. S., & Plueddemann, A. J. (2008). Western Arctic shelfbreak eddies: Formation and transport. *Journal of Physical Oceanography*, 38(8), 1644-1668.

Thomas, L. N. (2008). Formation of intrathermocline eddies at ocean fronts by wind-driven destruction of potential vorticity. *Dynamics of Atmospheres and Oceans*, 45(3-4), 252-273.

von Appen, W. J., & Pickart, R. S. (2012). Two configurations of the western Arctic shelfbreak current in summer. *Journal of Physical Oceanography*, 42(3), 329-351.

Weingartner, T., Aagaard, K., Woodgate, R., Danielson, S., Sasaki, Y., & Cavalieri, D. (2005). Circulation on the north central Chukchi Sea shelf. *Deep Sea Research Part II: Topical Studies in Oceanography*, 52(24-26), 3150-3174.

Weingartner, T., Dobbins, E., Danielson, S., Winsor, P., Potter, R., & Statscewich, H. (2013). Hydrographic variability over the northeastern Chukchi Sea shelf in summer-fall 2008–2010. *Continental Shelf Research*, 67, 5-22.

Winsor, P., & Chapman, D. C. (2004). Pathways of Pacific water across the Chukchi Sea: A numerical model study. *Journal of Geophysical Research: Oceans*, 109(C3).

Woodgate, R. A., Weingartner, T. J., & Lindsay, R. (2012). Observed increases in Bering Strait oceanic fluxes from the Pacific to the Arctic from 2001 to 2011 and their impacts on the Arctic Ocean water column. *Geophysical Research Letters*, 39(24).

Woodgate, R. A., Aagaard, K., & Weingartner, T. J. (2005). A year in the physical oceanography of the Chukchi Sea: Moored measurements from autumn 1990–1991. *Deep Sea Research Part II: Topical Studies in Oceanography*, 52(24-26), 3116-3149.

Chapter 2

Assessing the role of oceanic heat fluxes on ice ablation of the central Chukchi Sea Shelf

Submitted to *Progress in Oceanography*, May 2019

Kofan Lu[1], corresponding author, klu3@alaska.edu

Seth Danielson[1] (sldanielson@alaska.edu), University of Alaska Fairbanks

Kate Hedstrom[1] (kshedstrom@alaska.edu), University of Alaska Fairbanks

Thomas Weingartner[1] (tjweingartner@alaska.edu), University of Alaska Fairbanks

[1]College of Fisheries and Ocean Science, University of Alaska Fairbanks, Fairbanks, AK, USA, 99775-7220

Keywords: Chukchi Sea, Bering Strait, baroclinic instability, ice model, mesoscale eddy

Abstract

This study investigates the role of oceanic heat flux convergence in the summertime retreat of sea ice in the presence of a mean background flow. Prior observations and preliminary numerical model results indicate that eddies generated along the marginal ice zone front carry substantial quantities of heat laterally beneath the ice, but the importance of these fluxes to the summertime retreat of sea ice directly is not well established. We use the Regional Ocean Model System (ROMS) with an idealized configuration of the Chukchi Sea shelf and without wind forcing, to: 1) determine the contributions to ice melt from the oceanic heat flux compared to that from the net atmospheric heat flux through the ice surface; 2) evaluate the role of mesoscale fluctuations versus the mean background flow in providing this sub-surface heat flux, and 3) evaluate the role of the underlying bathymetry in modifying the subsurface heat flux to the ice. Analyses show that the three main water masses (Melt Water, Bering Sea Water and Winter Water) establish frontal systems (the Shelf Water Front and the Ice Edge Melt Water Front) that control baroclinic processes, which in turn regulate the quantity of heat fluxed laterally and vertically to the ablating ice edge. We identify and characterize distinct oceanic zones associated with these fronts (the Shelf Water Transition Zone and the Melt Water Transition Zone) that are delineated by flow dynamics and hydrographic structure. We provide a parameterization for the vertical heat transport to the ice through the near-surface meltwater lens that is a function of the along-front current velocity and the cross-front temperature gradient. Such parameterizations could improve coarse-scale ocean and climate models that lack the vertical or horizontal resolution necessary for reproducing such small-scale processes. The results of this study may be informative to further investigations of the associated ice edge communities, and in helping to predict future ice-edge ecosystem conditions.

1. Introduction

Summer ice retreat over the Chukchi Sea responds thermodynamically to oceanic and atmospheric heat fluxes, and dynamically to advection by currents and winds. However, the relative contributions of these factors and how they interact with one another to affect ice retreat has not been explored systematically. One of the goals of this paper is to compare the roles of the oceanic and atmospheric heat fluxes in the Chukchi Sea ice melt.

The principal oceanic heat source to the Chukchi shelf is the northward transport of Pacific waters through Bering Strait. Woodgate et al. (2005; 2012) estimate that, on annual average, the northward mass and heat transports through the Strait are ~0.8 Sv and ~3 to 5×10^{20} J (~9-15 TW), respectively, and that the volume and heat transport have both increased by about 25% in recent years (Woodgate et al., 2012; Woodgate, 2018). The flow is bathymetrically steered across the shelf, creating distinct spatial patterns (Figure 1a) in the ice cover that consist of ice-edge embayments (Paquette and Bourke, 1981; Bourke, 1983) and which were well-known to 19th century whalers (Bockstoce, 1986). Ice preferentially retreats in Herald Valley, the Central Channel, and Barrow Canyon, (the main transport pathways across the shelf Woodgate et al., 2005; Winsor and Chapman, 2004; Weingartner et al., 2005; Spall, 2007) but lingers much longer over Herald and Hanna shoals, where the flow dynamics favor the likely development of Taylor columns (Martin and Drucker, 1997).

Chukchi shelf summer temperature and salinity properties vary widely but include three primary water masses evident in the meridional sections of temperature and salinity. These water masses were observed on the shelf east of the Central Channel in the sections redrawn from Paquette and Bourke (1981) on the shelf west of the Central Channel in August 1977 (Figure 1b,

c, respectively). They consist of cool (0 - 2 °C), low-salinity (26 - 30) melt water (MW), warm (2 - 6 °C), moderately salty (~30 - 32) Bering Sea Water (BSW) and near-freezing (-1.8 - 0°C), saline (>32.5) winter water (WW) formed the previous winter. Note that over the northern half of the sections the water column structure consists of a shallow (5 – 10 m) MW layer overlying a thick (25 – 30m) bottom layer of WW, with the two water masses separated by a strong but thin (~5 m) pycnocline. Less-stratified BSW lies over the southern portion of the sections. BSW is separated from MW by a surface front and from WW by a bottom front; these fronts are not necessarily laterally co-located.

The massive heat supply of the Bering inflow is, in principle, sufficient to melt the ~2 m thick ice cover over nearly the entire Chukchi shelf (Woodgate et al., 2010; Woodgate et al., 2012). However, the MW/BSW surface fronts (evident at ~ km 70 in Figures 1b and c and shown in other sections by Paquette and Bourke, 1981 and Weingartner et al., 2017), prevent direct interaction between the BSW and the ice. Lu et al. (2015) showed that BSW can penetrate the pycnocline between the MW and WW in the form of intra-pycnocline intrusions (eddies and/or filaments) that are 10 – 20 m thick and arise from MW/BSW frontal instabilities. Marginal ice zone (MIZ) instabilities have been well-documented (Johannessen et al., 1994; Fukamachi et al., 1998; Shuchman et al., 2004; Manucharyan and Thompson, 2017) along with the intrusions that evolve from such fronts (Lee et al., 1981; May and Kelly, 2001; Badin et al., 2009; Kuzmina, 2016). In the Chukchi Sea, these intrusions are found just below the shallow surface layer. Consequently, they may be an important source of heat to the surface layer and to the ice.

Our paper addresses two main issues. First, we determine the magnitude of the oceanic heat flux to the ice and compare this flux with the contribution of atmospheric heating at the

surface of the ice. Second, we evaluate the relative roles of intra-pycnocline eddies and the mean flow in feeding the oceanic heat flux to the ice. This portion of the paper includes an analysis of the spatial variations in the ice-ocean fluxes, frontal structures, and frontal processes. The analyses are based on a suite of numerical model runs using the Regional Ocean Modeling System (ROMS) that includes sea ice.

Our paper is organized as follows. Section 2 discusses the model formulation and experiments and Section 3 describes the analytical methods. Section 4.1 compares the roles of the oceanic and atmospheric heat fluxes on ice melt. We examine the influence of intra-pycnocline eddies, induced by various stratifications and frontal instabilities associated with the water masses in Section 4.2. In Section 4.3, we show that the eddies also enhance vertical mixing amongst the water masses. In Sections 5.1 and 5.2, we examine the sensitivity of ice retreat to variations in Bering Strait inflow properties (temperature, salinity, and transport). In Section 5.3 we find that intra-pycnocline eddies play an important role in ice melt by driving a cross-isobath heat flux that transports heat from the mean, along-isobath Bering Strait inflow over portions of the shelf east of the Central Channel.

2. Model

2.1 Model Setting

The study uses an ice-ocean-coupled model based on the Regional Ocean Modeling System (ROMS; Shchepetkin and McWilliams, 2005). Figure 2 shows the numerical model configuration, which is a box extending 700 km in the meridional (y) and 800 km in the zonal (x) directions. The bathymetry consists of a 45 m deep shelf and a 50 m deep meridionally-oriented channel centered along x = 350 km. This configuration, which mimics the southern half of the Chukchi's Central Channel, narrows hyperbolically from 500 km width at 150 km north of the inflow (y = 0) source on the southern boundary to 100 km width at the northern end of the domain. To avoid lateral boundary effects, we analyzed only model results within the Figure 2 box indicated by the black square ($100 \leq x \leq 700$ km and $150 \leq y \leq 650$ km). Geostrophic adjustment to the inflow occurs over the first 150 km between the inflow source (y = 0 and depth = 45 m) and the southern edge of the channel (y = 150 km and depth = 50 m). The model resolution is 1 km in the horizontal and ~1 m in the vertical, which contains 40 levels. The vertical turbulent viscosity and mixing coefficients use the Mellor-Yamada level 2.5 turbulence closure scheme with background coefficients 10^{-6} (Mellor and Yamada,1982; Galperin et al., 1988; Kantha and Clayson, 1994; Durski et al., 2004). The sea ice module is based on the elastic-viscous-plastic (EVP) rheology (Hunke and Dukowicz, 1997; Hunke, 2001), and one-layer ice thermodynamics with a molecular sublayer under the ice (Mellor and Kantha, 1989). The ice thermodynamics variables used for the initializations are described in Hedstrom (2018).

At the start of all model runs the sea ice has a concentration of 100% and a thickness of 2 m and salinity of 3.2, consistent with the Chukchi Sea late-winter ice cover (Frey et al., 2014). The initial seawater conditions consist of unstratified WW with $\theta = -1.8°C$, S = 33 and ρ =

1026.5 kg m^{-3}. A 100 km-wide inflow (300 km $\leq x \leq$ 400 km; y = 0 km) represents the Bering Strait inflow with θ = 6°C, S = 30 and ρ = 1023.6 kg m^{-3}. The inflow increases from zero to ~0.8 Sv in 1 day and then remains constant over the remainder of the 120-day model integration time. The Coriolis parameter ($f = 1.4\times10^{-4}$ s^{-1}) is constant everywhere. Model analyses assess the 90-day period of June 1 to late August.

Atmospheric forcing ramps up from zero to the values of June 1 during a 30-day adjustment spin-up time interval. These include downwelling shortwave and longwave radiation imposed as spatially homogeneous monthly averages as the summer progresses and are based on the 2012 National Center for Atmospheric Prediction (NCEP) North American Regional Reanalysis (NARR) data (Mesinger et al., 2006). Sensible, latent, upwelling longwave and reflected shortwave are computed using bulk formulae to complete the surface heat budget at the surface, also using the NCEP air temperature and air humidity as needed.

We integrated the model with 12 combinations of three different inflow temperatures (θ = 4, 6, 8 °C) and four volume transports (0.6, 0.8, 1.0, 1.2 Sv) to investigate the contributions of oceanic heat fluxes to the ice retreat. In each experiment the inflow properties remain constant with time.

2.2 Model Validations

2.2.1 Heat Budget Balance

The heat budget is evaluated via Eq. 2.1 and is based on the balance between the changing rate of oceanic heat content and the sum of heat fluxes across the four lateral boundaries and the surface of the integration box.

$$\frac{\partial(\rho_{WW} C_P V_{oc}(\theta-\theta_{WW}))}{\partial t} = \quad \text{(Eq.2.1)}$$

$$(\rho_{BSW} C_P \vec{v} \theta A_{south} - \rho_0 C_P \vec{v} \theta A_{north}) + (\rho_0 C_P \vec{u} \theta A_{west} - \rho_0 C_P \vec{u} \theta A_{east}) + (F_{surface} \Downarrow - \rho_0 C_P \vec{w} \theta A_{surface})$$

where ρ_{WW} is the WW density ~1026.5 kgm^{-3}, ρ_{BSW} is BSW density ~1023.7 kgm^{-3} and ρ_0 is the reference seawater density ~1025 kgm^{-3}. C_P is the specific heat 3990 J-kg^{-1}K^{-1}, V_{oc} is the ocean volume within the box, $A_n$is the area of each side of the box, $\theta_{WW}$is the initial WW potential temperature -1.8 °C, $F_{surface} \Downarrow$ is the surface heat flux through the ice and into the ocean. θ, $\vec{u}$, v and $\vec{w}$ are seawater potential temperature and velocities in x, y and depth (z), respectively.

Figure 3 is based on model results using Bering Strait inflow properties of 6 °C and 0.8 Sv. In Figure 3a, the left-hand side of Eq.2.1 is indicated by the red dashed line and the black line indicates the right-hand side; the two lines are identical as expected after geostrophic adjustment. Figure 3b presents the six terms from the right-hand side: heat fluxes along the northward (outflow > 0 and yellow), western (green) and surface (outward > 0 and magenta) boundaries are negligible and overlap each other near the zero line. The red line in Figure 3c is the sum of the first four terms on the RHS of Eq. 2.1, representing the net horizontal oceanic heat transport and the blue line is the atmospheric heat flux through the sea surface (the fifth term in Eq. 2.1). The last term is the heat loss through the sea surface, and is ignored because it is an order of magnitude smaller than the other terms. Figure 3c shows that the oceanic heat is larger than the atmospheric heat over the entire integration period. We examined this balance for all 12 integrations and detail the results in Section 4.1.

2.2.2 Fresh Water Budget Balance

The fresh water budget is evaluated as the balance between the changing rate of fresh water volume and the sum of the fresh water fluxes across the five sides (including the ice meltwater at the surface) of the model domain as follows.

$$\frac{\partial\left(\rho_{WW}V_{oc}\frac{(S_{WW}-S)}{S_{WW}}\right)}{\partial t} = \qquad \text{(Eq. 2.2)}$$

$$\left(\rho_{BSW}\vec{v}\frac{(S_{WW}-S)}{S_{WW}}A_{south} - \rho_0\vec{v}\frac{(S_{WW}-S)}{S_{WW}}A_{north}\right) + \left(\rho_0\vec{u}\frac{(S_{WW}-S)}{S_{WW}}A_{west} - \rho_0\vec{u}\frac{(S_{WW}-S)}{S_{WW}}A_{east}\right) + (Ice\ Melt \Downarrow)$$

Notations are the same as in Section 2.2.1 with S_{WW} being the initial WW salinity (= 33) and S the model-determined salinity. Ice melt⇓ is surface melt water flux into the ocean from the ice.

As with the heat balance, the two sides of Eq. 2.2 (left: red dashed line, right: black line in Figure 4a) are consistent with each other. Figure 4b shows plots of the five terms on right-hand side of Eq. 2.2. The meltwater flux from ice (black) and the fresh water transported by the Bering Strait inflow (red) are the two largest sources and of comparable magnitude. An appreciable fraction of the Bering freshwater flux is lost to the east (blue). Freshwater outflow to the north (yellow) and exchanges with the west (green) are substantially smaller. The net freshwater transport across the lateral sides of the integration box (the sum of first four terms of Eq. 2.2) is, shown by the red line in Figure 4c and the fresh water from ice melt is indicated by the blue line. With our forcing and model configuration, we find that the ice melt contribution to the fresh water on the Chukchi shelf is more than the Bering Strait inflow; it comprises ~55% of the total in mid- June and increases to ~80% at the end of August.

3. Methods

3.1 Water mass classification

The three major water masses (MW, BSW, and WW) and their mixtures are classified in the model runs based on their properties and the ratio (m) of the potential temperature anomaly ($\Delta\theta$) to the salinity anomaly (ΔS), where the anomalies are referenced to the initial WW properties (θ=-1.8°C; S=33). Figures 5a and b are T-S diagrams derived from the model having an inflow temperature of θ = 6°C. Figure 5a shows the T-S diagram at model day 70, where the colors indicate the meridional position (y) of the water type relative to the southern boundary. From Figure 5a, the BSW/WW and BSW/MW mixtures lie between ~50-120 km, with the BSW/WW mixture being most prevalent. The MW/WW mixtures extend from about y~100 km to the northern boundary. Water masses with temperatures > 0°C and salinities mostly <28 occur between ~100-200 km.

Figure 5b uses color to show the evolution of T-S properties through time based on a census every 10 days. The potential temperature of the BSW/WW mixtures increases with time via the warming of BSW by solar radiation. Similar results hold for the initial BSW inflow potential temperature of 6°C as the BSW/WW mixture potential temperatures increase to ~8°C by the end of August (model day 90). Our criteria based on the T-S anomaly slope (m) as evaluated from equations Eq.3.1-3.3 works well for classifying BSW for all model experiment inflow temperatures. In contrast to the BSW/WW mixtures, the potential temperatures of MW/WW mixtures decrease with time especially for water masses with salinity >28, for which the MW lies under the pack ice and is formed due to surface melt by solar radiation. The sub-ice pool of MW pool cools through time due to mixing with WW and from above is insulated from direct atmospheric heat fluxes by the pack ice. The BSW/MW mixtures occur continually but

there is no temporal trend in the salinity of this mixture. Although the quantity of the BSW/MW mixture increases with time, there remains a substantial separation in T/S space between the MW and BSW source waters.

We define a boundary that best represents this separation amongst mixtures derived primarily from BSW or MW by the following equations. The various water types formed in the model are based on the initial WW properties and determined by the ratio:

$$m = \frac{\Delta\theta}{\Delta S} = \frac{(\theta - \theta_{WW})}{(S - S_{WW})} \quad \text{(Eq.3.1)}$$

The water types having properties similar to WW (blue half circle in Figure 5) are classified as WW from Eq. 3.2,

$$\sqrt{\Delta\theta^2 + \Delta S^2} \leq 1: WW \quad \text{(Eq. 3.2)}$$

The remaining water types are separated into BSW and MW according to the value of *m*

$$\begin{cases} m_{mid} \leq |m| < 0: BSW \\ |m| < m_{mid}: MW \end{cases} \quad \text{(Eq. 3.3)}$$

Where m_{mid} (blue line in Figure 5a and 5b) is the slope threshold determined by the following equations to distinguish the BSW/WW mixtures from the MW/WW mixtures:

$$m_{mid} = \frac{|\theta_{mid} - \theta_{WW}|}{(S_{BSW} - S_{WW})} \quad \text{(Eq. 3.4)}$$

$$\theta_{mid} = \frac{|\theta_{BSW} + \theta_{WW}|}{2} \quad \text{(Eq. 3.5)}$$

The classification results are shown in Figure 5c and 5d by way of instantaneous vertical sections of potential temperature and salinity, respectively (on model day 70 along x = 450 km, which is located along the gray dashed line in Figure 6b). In Figures 5c and d, the blue contour delineates the classified MW, the red contour delineates the classified BSW, and the remaining waters are considered WW. The positions of each water mass shown in these transects are

consistent with the description in Figure 5a. This classification method helps us understand the dynamics and the water mass interactions, which in turn affect the heat fluxes to the ice.

3.2 Front detection

There are two frontal systems that we recognize based on the water mass distributions discussed above (Figures 6a and 6c). Proceeding from north to south, the Ice Edge Melt Water (IEMW) front separates low-salinity (S<28) MW found along the ablating ice edge from the thin layer of MW (28<S<30) under the pack ice, which forms by melting from solar radiation. The Shelf Water (SW) front is associated with the Bering Strait inflow and occurs where the BSW occupies the bulk of the water column. Both fronts occur where water mass properties change most rapidly in the meridional direction.

The IEMW front is detected when the near-surface (upper 15 m) vertically averaged meridional density gradient $\partial\rho_h/\partial y$ is larger than 0.12×10^{-3} kgm^{-4}. Low-salinity melt water replaces the winter water in the upper 15 m as evaluated by Eq. 3.6, where ρ_h is density averaged vertically over water depth h, ρ_{WW} is the winter water density 1026.5 kgm^{-3}, $\rho_{MW}$is the melt water density (~1022.5 kgm^{-3}), H is the 50 m maximal water depth in Central Channel. The along-channel length scale, ∂y ~10 km is approximately twice the baroclinic radius of deformation (R_d~ 5 km).

$$\frac{\partial\rho_h}{\partial y} = \partial\frac{\left(\rho_{WW} - \frac{\rho_{MW}\times15+\rho_{WW}\times(H-15)}{H}\right)}{\partial y} = \frac{1026.5 - \frac{1022.5\times15+1026.5\times35)}{50}}{10^4} = 0.12\times10^{-3} \qquad \text{(Eq. 3.6)}$$

The SW front separates WW, MW, and BSW intrusions from unstratified BSW. To identify the location of this front, the water mass identified as BSW with methods in section 3.1 are marked as 1 and the rest of water masses are marked as 0. The vertically averaged water mass tracer thus considers only $\phi=\frac{1}{h}\int(m)dz$, where h is water depth, ρ is density and $m(y,z)$

equals 1 for BSW and 0 for other water masses. Then the SW front is identified where the vertically averaged meridional gradient ($\partial\phi/\partial y$) exceeds 8×10^{-5}. This criterion eliminates small-scale (<10 km) BSW intrusions and weak fronts associated with mixing of BSW with MW or WW.

The IEMW and SW fronts delineate striking meridional structures of the water column; their positions correspond to the heterogeneous MIZ conditions shown in Figure 6a and 6c. The IEMW front, which marks the boundary between the solar-melted MW (28<S<30) and the very fresh MW (S<28) plume near the ice edge, lies beneath nearly 100% ice cover of ~2m thickness. South of the IEMW front, both the ice concentration and thickness decrease rapidly. The SW front, which separates unstratified BSW from WW and/or the MW plume, typically occurs under much sparser (<15%) ice concentrations and thinner (<1 m) ice. Although there exist few Chukchi shelf hydrographic cross-sections that extend from open water to 100% ice cover, the observations of Paquette and Bourke (1981) shown in Figures 1b and c are very consistent with the model-derived front locations and structure with respect to the ice cover. Our IEMW-defined front occurs around their station 11, where the MW plumes occur beneath ~100% ice cover. The SW front is centered around their stations 5 and 6, where the warmer BSW is separated from WW and MW and ice concentrations are <15%. Due to the appreciably different hydrographic and ice conditions separated by these two fronts, we analyze and discuss our model results in accordance with their locations.

3.3 Reynolds decomposition based on structure functions

Instantaneous lateral heat fluxes accompanying the front were evaluated by Reynolds decomposition of the along-front heat flux. Since the front position and frontal propagation direction varies with time, both time- and space-averaging over the dominant time and length

scales are needed to evaluate the heat transported by the mean flow and the eddies. The Reynolds decomposition calculations are referenced to the coordinates based on the local orientation of the front at every instant of time.

The basic Reynolds decomposition of the heat flux is given by:

$$\rho C_p[V(x,y,t)\theta(x,y,t)h(x,y,t)]_{x_p,y_p} \quad \text{(Eq. 3.7)}$$

$$= \rho C_p\left[(\overline{V\theta} + \bar{V}\theta' + V'\bar{\theta} + V'\theta')\bar{\mathrm{h}} + (\overline{V\theta} + \bar{V}\theta' + V'\bar{\theta} + V'\theta')h'\right]_{x_p,y_p}$$

All quantities are integrated over the water column with fixed layer thickness so the fluctuation of layer thickness h' will be zero (i.e. the terms multiplied by h' on the right-hand side). For the remaining terms on the right hand side, we focus on the heat transported by the mean flow (i.e. $\rho C_p \overline{V\theta h}$) and by the fluctuations (i.e. $\rho C_p V'\theta'\bar{h}$), where the components of mean flow term ($\bar{V}, \bar{\theta}, \bar{\mathrm{h}}$) are time-averaged over 5 days and space-averaged over 30 km to filter out small-scale features but still preserve the major front characteristics. The 5 day and 30 km integration scales are determined by the autocorrelations of the structure function per Zhang and Gawarkiewicz (2015), which provide upper bounds for the time and length scales that contain homogeneous and steady hydrographic features. Eddy heat transport evaluated with a range of averaging scales are found to be quite similar to each other: differences resulting from reasonable parameter choices (1 to 10 days and 20 to 30 km) are less than 10%.

The autocorrelations of the structure function per Zhang and Gawarkiewicz (2015) are calculated using Eq.3.8 and Eq.3.9. The along-channel structure function ($Q(y,t)$)is the mean square salinity difference (a proxy for density in high latitudes) separated by an along-channel distance Δy at depth d = 5 m below the surface e.g.:

$$Q(y,t) = \{[S_d(x,y+\Delta y,t) - S_d(x,y,t)]^2\}_y \quad \text{(Eq. 3.8)}$$

Where $\{\cdot\}$ denotes averaging over 0 to $L_y - \Delta y$ in the along-channel direction.

The space-lagged autocorrelation ($r(y,t)$) is then:

$$r(y,t) = 1 - \frac{1}{2}\frac{Q(y,t)}{var(S_d)} \quad \text{(Eq. 3.9)}$$

Where the $var(S_d)$ is the variance of S_d from 0 to $L_y - \Delta y$ and is the normalization factor (Davis et al., 2008). Hence r approaches 0 when the structure function Q is larger than twice the variance of S_d (i.e. the variations of along-channel salinity from 0 to $L_y - \Delta y$ are so large that Δy cannot possibly be the frontal length scale). The last step in determining the dominant length scale is to identify the first trough in the structure function, which corresponds to the secondary maximum of the autocorrelation function (Zhang and Gawarkiewicz, 2015). The dominant time scales can be determined by the same procedure, except the structure function $Q(y,t)$ is based on the mean square difference in salinity separated by time intervals, Δt = 1, 2, ... to 30 days, and averaging over the total model time per Eq. 3.10:

$$Q(y,t) = \{[S_d(x,y,t+\Delta t) - S_d(x,y,t)]^2\}_t \quad \text{(Eq. 3.10)}$$

We applied the same analyses to the along-channel velocity (v) to find the dominant length and time scales associated with frontal processes. From these analyses, the maximal frontal length scale is ~30 km (~6 R_D) for both salinity and along-channel velocity, the maximal time scales are ~20 days for salinity and ~7 days ($\sim\frac{R_D}{V_{front}}$) for the along-channel velocity structure. We choose 30 km as a spatial averaging scale and 5 days as temporal averaging scale for the Reynolds decomposition to make sure the characteristics of the mean flow are reasonably stable across the averaging intervals.

4. Results

In this section, model results are integrated over four zones defined by the length scales and position of the fronts as determined by the methods of Section 3 for the 12 different experiments within the integration box (per Figure 2 and as described in Section 3.1). From the transects in Figure 6 and the fronts described in Section 3.2, four zones shown in Figure 6 and Table 1 are identified that correspond to differing ice and oceanographic conditions. From north to south these include the pack ice zone (PIZ), the melt water transition zone (MWTZ), the shelf water transition zone (SWTZ) and the ice free zone (IFZ). The SWTZ extends from open water to partial ice cover and the MWTZ extends from partial ice cover to the pack ice. We note that the MWTZ and the SWTZ together encompass much more than the MIZ. The MIZ is classically defined using a range of partial ice cover, such as 15-80% concentration, although other definitions exist as well (Strong et al., 2017). Our analyses are designed to reveal some previously undescribed oceanographic structures in the vicinity of the MIZ, and to assess their dynamics.

4.1 Oceanographic characteristics of the ice edge

Figure 6c shows a thin layer of fresh water with salinity ~28 to 30 in the uppermost 5 meters of the PIZ. This MW layer comes solely from ice melt resulting from atmospheric heating: warm BSW is not present and WW is not a heat source.

The MW layer in the MWTZ is fresher than in the PIZ, with salinities diminishing southward across this zone to < 28 and occupying a layer ~10 - 15 meters thick. This MW layer forms because the ice is melted rapidly by oceanic heat delivered laterally and vertically to the ice edge (discussed in Sections 4.1-4.3 below), including from oceanic heat that has been warmed by the atmosphere en route across the Chukchi Sea from Bering Strait. The ice thickness

declines within the MWTZ from ~2 meters within the PIZ to zero. Due to the lateral pressure gradient across the front separating MW from BSW, eddies are induced by baroclinic instabilities resulting in modeled eddy kinetic energy (EKE) values as large as ~11.5 cm^2s^{-2} in the MWTZ. The ice edge MW plume ($S < 26$ in Figure 6c) extends across both the MWTZ and the SWTZ, but is primarily centered in the region found between low ice concentrations (< 15%) and thin ice (< 0.5 m). The ice edge MW plume may be the oceanographic feature that most closely aligns with typical definitions of the MIZ.

The SWTZ is the most energetic zone (EKE ranges from 18.5 to 50.0 cm^2s^{-2}) as it is disturbed by frontal meanders and instabilities that actively interact with the surface MW and the subsurface WW. This zone consists of BSW modified by mixing with MW and WW. Within 10 m of the seafloor, winter water (WW) intrudes below the BSW. The along-channel (y) scale of the SWTZ is approximately 60 km, or about 2-3 times the dominant frontal length scale determined by the structure function in Section 3.3. The maximum SWTZ ice concentration decreases from ~50% in early summer to ~30% in late summer, placing it within the MIZ.

The IFZ contains weakly-stratified BSW over the entire water column and has hydrographic properties similar to those of the Bering Strait inflow, modestly modified by insolation and any mixing with waters from north of the SW front. Eddies in this zone originate in the SWTZ and although somewhat energetic, do not directly interact with the ice edge. We therefore focus attention on the SWTZ and MWTZ instabilities and mean flows.

4.2 Lateral oceanic heat transport

The total heat flux derives from the lateral oceanic heat transport and surface atmospheric heating, and is evaluated separately from the heat balance (Eq. 3.1). We assess the importance of lateral oceanic heat transport (Figure 7) by computing the ratio of the oceanic heat transport to

the sum of the oceanic and atmospheric heat transports (i.e. right-hand side of Eq.3.1; Figure 7b) and examining the corresponding ice melt rate overlain on the area-averaged ice thickness (Figure 7a).

Within the PIZ, sea ice melts primarily by local atmospheric heating because the Bering Strait inflow does not influence this zone. In contrast, the oceanic heat transport contributes more than 70% of the heat to ice ablation in the MWTZ and the SWTZ. In both zones, the melting rates by oceanic heating are more than 2.5 cm of ice per day, or triple the ice melt rate caused by atmospheric heating alone. The stronger (1-1.2 Sv) and warmer (6-8 °C) Bering Strait inflows tend to supply more oceanic heat (~80% of the total) and accelerate the ice ablation compared to the weaker and cooler inflows (~70%). The importance of oceanic heat to the heat budget decreases within the IFZ because solar heating of the ocean increases due to the lower average albedo (e.g., <0.1). In the MWTZ and SWTZ oceanic heat fluxes dominate. We next show the inflow discharge rate is more important than inflow temperature in controlling the lateral heat transport by both the mean flow and the eddies.

4.3. Lateral eddy heat transport

Lateral eddy heat transport is evaluated as the fluctuating term $\rho C_p h V' \theta'$ from Eq. 3.7 via Reynolds decomposition. The importance of the eddy heat transport is assessed as the proportion of the lateral eddy heat transport to the total oceanic heat flux calculated as described in Section 3.1 from Eq. 3.1.

Eddies transport 10 – 30% of the total oceanic heat in the MWTZ and 30 – 50% in the SWTZ (Figure 8a). As shown in Figure 8b and 8c, both the mean and eddy heat transports increase as the Bering Strait inflow discharge increases. The eddy heat fluxes decrease as the Bering Strait inflow temperature increases, which we hypothesize is due to the decreased density

difference between the warmer Bering Strait inflows and the MW. This hypothesis is tested in Section 5.2.1 using models whose density is based only on salinity and thus excludes the effect of inflow temperature on heat transport.

4.4. Vertical Oceanic Heat Transport

Vertical heat transport is calculated as Eq. 4.1 integrated over the MW layer and BSW layer defined by the water mass classification scheme of Section 3.1.

$$Vertical\ Heat\ Transport\ = \frac{1}{h_{(BSW,MW)}} \int \rho_0 C_p \vec{w}(\theta - \theta_{WW}) A dz \qquad \text{(Eq. 4.1)}$$

Where $h_{(BSW,MW)}$ is the layer thickness of BSW or MW, ρ_0 is the referenced seawater density as 1025 kgm^{-3}, C_p is the specific heat capacity of seawater, $\vec{w}$ is vertical velocity, θ is the potential temperature, θ_{WW} is referenced to the WW temperature (-1.8 °C), A is the surface area of each zone and the vertical extent (dz) of the integral is evaluated over the MW layer and BSW layer separately. Since the potential temperature for calculating the vertical heat transport is referenced to WW temperature, the transport direction is determined by the vertical velocity $\vec{w}$, which is upward toward the surface when positive and downward when negative. We found that the vertical heat transports integrated over each control volume are upward on average. We next assess the importance of the vertical heat in proportion to the total lateral oceanic heat transport. Both the vertical and lateral heat transports are integrated and presented for the MW and BSW layers (Figure 9a, b, respectively) separately for the MWTZ and SWTZ areas.

Within the SWTZ, the vertical heat transport from the BSW layer (Figure 9b) can be substantial (>30%) at the beginning of model integration, but it generally decreases to <20% by day 30, after MW has formed and accumulated. This result arises because the increase in MW strengthens the stratification and suppresses the vertical heat flux from the BSW layer, similar to the findings of Manucharyan and Thompson (2017) for the Arctic basin. However, the newly

formed MW begins interact with BSW intrusions under the ice edge of the MWTZ and induce eddies via baroclinic instabilities. As the instabilities grow, the vertical heat transport across the MW layer (Figure 9a) often increases to >30% after day 30. This vertical heat flux into the MW layer is important in melting ice along the ice edge within the MWTZ.

Figure 9c and 9d show the monthly averaged vertical heat transport versus the monthly averaged eddy heat transport for the MWTZ and the SWTZ, respectively. The vertical heat transports are well-correlated to lateral eddy heat transports in both zones. In the MWTZ, both the vertical heat transport and lateral eddy heat transport increase with time. Consequently the vertical heat transport into the MWTZ is important melting ice throughout the summer.

5. Discussion

5.1. Role of Inflow from Bering Strait

As the inflow initiates ice melt and breakup, the surface albedo decreases due to formation of melt ponds, open water, and leads. The positive feedbacks of the ocean ice albedo system lead to increasing atmospheric heat fluxes through the ice and into the ocean. We find that warm BSW can provide more than 70% of the total heat flux for melting ice within the MWTZ and the SWTZ (Figure 7b). This oceanic heat supports melt rates of up to ~2.5 cm per day near the ice edge (Figure 7a), resulting in the formation of a ~10-15 m thick, fresh and somewhat insulating MW layer on top of cold WW (Figure 5).

Atmospheric heating also ablates ice into a cool, thin layer of MW just below the ice pack. BSW plumes subduct warmer waters into the pycnocline between MW and WW and as a result of baroclinic instabilities generated in the fronts between BSW and MW at depth ~10-15 m and BSW and WW at depth ~10-30 m (Lu et al., 2015). These eddies enhance lateral and vertical

oceanic heat fluxes as shown in Section 4.4 and as discussed further in Section 5.2. Nevertheless, more than 50% of the oceanic heat flux that melts ice is due to the mean flow (Figures 8b, c). Variations in the Bering Strait inflow transport exert a greater influence on ice retreat rates than do variations in the temperature of the inflow (at least over the parameter range examined here).

The inflow from Bering Strait not only supplies oceanic heat to melt ice thermodynamically; it also advects the ice pack. Figure 10 shows the open water area caused by advection only in comparison to the ice retreat associated with warm BSW and then the fully coupled system including atmospheric-ocean heat fluxes. The ocean heat-driven component dominates the ice retreat early in the season but this component is less than half of the total after only 40 days of integration. Thereafter the advective component dominates the oceanic influence on the open water area. In contrast, the open water area driven only by advection of the inflow (blue line of Figure 10) is ~35% of the open water area due to the combined effects of a warm BSW inflow and atmospheric forces (black line in Figure 10).

5.2. Frontal instabilities induced eddies

Our model results suggest that 30% to 50% of the oceanic heat that results in ice melt is transported laterally by eddies into the ice edge. Moreover, the eddies provide 10% to 30% of the BSW vertical heat fluxes through the MW layer into the ice (Figure 8a). Although the eddy energy is primarily determined by cross-frontal density differences, we show here that the Bering Strait volume and heat transport also play a role in setting the eddy heat transport ($\rho C_p V'\theta'\overline{h}$). This term is directly proportional to the Bering Strait inflow and is related to the mean flow heat transport derived from the Reynolds decomposition ($\rho C_p \overline{V\theta h}$).

5.2.1 Influence of Bering Strait inflow density to eddy transport efficiency

From Figure 8, we observe that eddy heat transports slightly decrease even if the temperature of the Bering Strait inflow increases from 4 °C to 8 °C. This is particularly true in the MWTZ, where the dependence is presumably related to the cross-frontal density difference. We excluded the effect of inflow temperature on heat transport and focus on the inflow density by means of a set of four model runs in which the BSW temperature and transport was fixed at 6°C and 0.8 Sv, respectively. Inflow salinities were 28 (ρ = 1022.03), 29 (ρ = 1022.82), 30 (ρ = 1023.60), and 31 (ρ = 1024.40).

The inflow density differently affects eddy transports across the BSW/MW front and the BSW/WW fronts because less dense BSW establishes a larger density gradient with the MW but a weaker gradient with the WW (Figure 11a). These density gradients shift in the opposite direction for the case of denser BSW (Figure 11b). As a consequence, the vertical heat flux changes for different inflow salinities, as shown by the August averages of the vertical heat transport components (Figure 11c and 11d). (In these figures $\overrightarrow{w}\Delta\theta$ was computed along x = 400 km and spatially referenced to the SW front.) Recall that all three water masses can occupy portions of the MWTZ and the SWTZ so that the strongest eddies (which dominate the eddy heat transport) are generated from different water mass pairs and their corresponding layer thicknesses. In the SWTZ, the maximal vertical heat transport occurs at ~20 – 30 m depths (Figure 11c and 11d), which is much deeper than the ~10 m MW layer thickness. This finding implies that eddies in the SWTZ are induced primarily by interactions between BSW and WW. By contrast, in the MWTZ, the vertical heat transport is maximal immediately below the MW layer at ~10 to 15 m depth. Vertical heat transports between BSW/WW and MW/WW in the MWTZ are very weak, again showing that eddies in the MWTZ are induced primarily by interactions between MW and intruded BSW. In fact, motions and vertical heat fluxes appear

negligible in the deeper WW.

For the SWTZ (Figure 11c), a less dense BSW inflow (salinity = 28) results in a stronger vertical heat transport compared to a denser BSW (salinity = 31, Figure 11d). On the other hand, the vertical heat transport in the MWTZ increases as the salinity of the BSW inflow increases. These relationships correspond to the relative density differences between the BSW, MW and WW water masses on fronts as discussed by Haine and Marshall (1998) and given by Eq. 5.1

$$u_{eddy} = \frac{g}{\rho_0 f} \Delta h \Delta \rho \qquad \text{(Eq. 5.1)}$$

Eq. 5.1 shows that the eddy velocity scale can be expressed with the cross-front density difference $\Delta\rho$ and that eddy transport should be directly proportional to the density difference between water masses, which induce strong eddies (i.e. $|\rho_{WW} - \rho_{BSW}|$ in the SWTZ and $|\rho_{BSW} - \rho_{MW}|$ in the MWTZ). Integrating our model with four different inflow salinities (S = 28, 29, 30 and 31) verifies the density gradient component of Eq.5.1 (Figure 12a and 12b). Moreover, Eq. 5.1 shows that the eddy transport is also affected by layer thickness difference Δh (Figure 12c and 12d). We notice that the eddy transport is dominated by Δh in the SWTZ and by $\Delta\rho$ in the MWTZ by comparing the shapes of Figure 12e to Figure 12a and c; and Figure 12f to Figure 12b and d. These comparisons show that vorticity in the SWTZ is strong enough to change the layer thickness; thus eddy transport in SWTZ is driven by layer thickness difference. In contrast, the MWTZ eddy transport is primarily driven by the density difference because density difference is larger between MW/BSW than BSW/WW. The layer thickness difference of water masses (i.e. thickness of evolved eddies) increases when the eddy relative vorticity increases with stronger eddy transport to maintain potential vorticity conservation in SWTZ (Figure 12g and 12h). Based on these results, the freshening and warming of the Bering Strait inflow as reported by Woodgate et al. (2012) may actually reduce the relative importance of eddy

heat fluxes on the Chukchi ice melt.

In conclusion, denser Bering Strait inflows induce larger eddy heat transports for melting ice in the MWTZ but smaller eddy heat transports in the SWTZ. Our findings suggest that in addition to the transport and temperature of the Bering Strait inflow, the rate of summer ice retreat over the Chukchi shelf depends upon the inflow salinity and stratification.

5.2.2 Eddy transport efficiency

Spall and Chapman (1998) relate the eddy transport, $\overline{u'\rho'}$, (where u' and ρ' are deviations from the temporal or spatial mean cross-front velocity and density, respectively) to the cross-front density difference, $\Delta\rho$, and the along-front velocity scale, V_m, i.e., $\overline{u'\rho'} = C_e V_m \Delta\rho$, where C_e is the efficiency constant. In a multi-layered system, V_m and C_e can be estimated from Eqs. 5.2 and 5.3, respectively:

$$V_m = \sqrt{g'h}\sqrt{\frac{\Delta h}{H}} = \sqrt{\frac{\Delta\rho}{\rho_0} g \Delta h}\sqrt{\frac{\Delta h}{H}} \qquad \text{(Eq. 5.2)}$$

$$C_e = \frac{\sum u'_N h'_N}{V_m h}, N = (MW, BSW, WW) \qquad \text{(Eq. 5.3)}$$

In Eq. 5.3 $\sum u'_N h'_N$ is the sum of the along front-averaged eddy thickness flux, where the flux is perpendicular to either the SW or IEMW front. The subscript N on the eddy thickness flux indicates integrations across BSW, MW and WW water mass layers. H is a scale height for the mean stratification and Δh is the vertical displacement of the interface across the front.

The efficiency coefficient in the SWTZ zone is ~0.04 to 0.06 (Figure 13a) and is ~0.02 in the MWTZ (Figure 13b). These values fall within the range of ~0.02 to 0.064 reported by Spall and Chapman (1998), where the efficiency coefficient is parameterized with the relative offset of

the upper- and lower-layer eddies (Fig. 2 of Spall and Chapman, 1998). The tight relation in the MWTZ indicates that this region is completely dominated by the baroclinic instability induced eddies, driven by the cross-frontal density difference. By contrast, the SWTZ strongly feels the influence of the inflow. The high efficiency constants found in the SWTZ shows that the eddies here are not only induced by the baroclinic instabilities, but also influenced by the Bering Strait inflow, which enlarges the relative lateral offset of the upper- and lower-layer eddies. Even though the Bering Strait inflow influences eddy transport in the SWTZ, the positive correlations between the scale of the along-front thickness flux $V_m h$ and the total eddy thickness fluxes $\sum u'_N h'_N$ occurs in both zones, supporting the conclusion in Section 5.2.1, that the cross-frontal density difference between fronts governs the eddy transport.

Due to the relatively tight correlations (R ~0.86 in MWTZ and ~0.92 in SWTZ) between eddy heat transport and vertical heat transport (Figures 9b and 9d), we may parameterize the Chukchi Sea vertical heat transport (VHF) to the ice using the eddy transport efficiency coefficient C_e as:

$$VHF = \frac{1}{D}\int \rho_0 C_p \vec{w}(\theta - \theta_{WW}) A dz = C_e \rho_0 C_p V_m \left(\theta_{inflow} - \theta_{WW}\right) dA \qquad \text{(Eq. 5.4)}$$

Where D is the ocean depth, θ_{inflow} is the initialized potential temperature of the Bering Strait inflow as 4°C, 6°C and 8°C, A is the total area of the transition zones and dA is grid area, 1 km^2.

The results are consistent with the parameterizations of eddy thickness fluxes. The vertical heat transport in the MWTZ is well-characterized by the parameterization in Eq. 5.4 using an efficiency constant (C_e) of ~0.02 (Figure 13d); and for the SWTZ, C_e ~0.04 to ~0.06 (Figure 13c). Vertical heat transport supplied by stronger Strait inflows (darker symbols in Figures 13c and 13d) are associated with a higher efficiency constant, showing that higher eddy transport efficiencies are related to the transport of the Bering Strait inflow.

5.3 Bathymetric steering of oceanic heat transport

Observations and circulation models show that Pacific waters are bathymetrically steered northward through the Central Channel and spread eastward along its length (Weingartnaer et al., 2013; Winsor and Chapman, 2004; Spall, 2007; Pickart et al., 2016). Figure 14a tracks and plots the eddy relative vorticity field overlain by the mean flow velocity at the SW front every 10 days over August (day 70, 80 and 90 of the model integration based on a 0.8 Sv inflow and 6°C inflow temperature). Within the Central Channel the velocities along the front are directed slightly northeastward. Primarily anticyclonic eddies form along the MW and SW fronts, which then propagate southeastward across the isobaths and away from the Channel. Consequently, the relative vorticity in the frontal zones is stronger to the east of the Channel than within it. The southeastward propagating eddies carry heat onto the shelf east side of the Channel. The anticyclones get stronger, presumably inducing southeastward meanders as they are squeezed across the shoaling bathymetry and adjust to conserve potential vorticity (Waseda and Mitsudera, 2002; Waseda et al., 2002; Gawarkiewicz et al., 2004). Figure 14b shows the monthly averaged relative vorticity field overlain by monthly averaging thermal wind velocity calculated on SW front as Eq. 5.5

$$\begin{cases} u_g = \frac{1}{h}\frac{g}{\rho_0 f}\int \frac{\partial \rho}{\partial y} dz \\ v_g = \frac{-1}{h}\frac{g}{\rho_0 f}\int \frac{\partial \rho}{\partial x} dz \end{cases} \quad \text{(Eq. 5.5)}$$

where f is Coriolis parameter as 1.4×10^{-4}, $\frac{\partial \rho}{\partial x}$ and $\frac{\partial \rho}{\partial y}$ are density gradients. Flows associated with the front on the east side of Central Channel derive primarily from the meanders induced by anticyclonic eddies because of thermal wind balance (Figure 14a and 14b).

We compare the eddy thickness fluxes $\sum u'_N h'_N$ (Spall and Chapman, 1998) and mean flow thickness flux $\bar{v}h_{BSW}$ within the Channel (depth ≥ 50 m, Figure 14c) and to the east of it

(depth < 50 m, Figure 14d). The latter is the product of the meridional mean flow velocity $\bar{v}$ evaluated from the Reynolds Decomposition (Eq. 3.7), using the BSW layer thickness h_{BSW} at the SW front. Both the eddy and mean flow thickness fluxes are area-averaged over the combined area of the MWTZ and the SWTZ but separately within the Central Channel (Figure 14c) and to the east of the Channel (Figure 14d). Figure 14c shows that the mean flow is persistently northward within Central Channel throughout summer. By contrast, the mean flow thickness flux east of the Channel turned southward in late summer (July ▽ and August △, Figure 14d) when inflow discharge is strong enough (>0.8 Sv) regardless of inflow temperature indicated by marker size in Figure 14d. The eddy fluxes east of the Channel are stronger than the eddy fluxes within the Channel in average. Moreover, mean flows east of Central Channel tend to turn more southeastward with stronger eddy fluxes, indicating that the eddies both expand the ice melt area and affect the route of the Bering Strait transport across the shelf.

6. Conclusions

This study provides a new look at the summer evolution of sea ice melt in the presence of a mean background flow and proposes a hydrographic classification system that encompasses our understanding of the fronts, stratification, energetics and heat fluxes. We describe the oceanographic structure with respect to the ice edge region as represented by an idealized model of a portion of the Chukchi Sea continental shelf (the Central Channel). The frontal systems established across the three main water masses (melt water, Bering Sea water and winter water) control baroclinic processes that in turn regulate the quantity of heat fluxed laterally and vertically to the ablating ice edge.

Our work provides a set of systematic analyses that assess the importance of the Bering

Strait inflow on ice ablation over the Chukchi Shelf using a simple model that mimics the Central Channel. Although the model ignores the complexity of bathymetric and coastline variations, the effects of wind, and shorter-term variations in atmospheric fluxes and Bering Strait influxes of heat and mass, this simplicity nevertheless identifies key factors that influence ice melt and the associated hydrographic structure (Figure 15). The Bering Strait inflow is critical in initiating ice retreat by melting the ice edge directly and by advecting ice northward. Both processes contribute positively to ocean and ice albedo feedbacks associated with the absorption of incoming solar radiation. Although these processes enhance the solar radiative influx to the ocean, the Strait inflow is responsible for the bulk of the ~10 TW (Table 2) of heat in summer in our model, in agreement with the observations of Woodgate et al. (2010).

The oceanic heat flux contributes more than 70% of the heat budget associated with melting ice along the ice edge and the marginal ice zone, which extends ~120 km southward from the main pack ice. The model indicates that eddies carrying heat from the Bering Strait inflow (and heat gained from the atmosphere en route) provide ~30% of the total oceanic heat transported laterally to the ice. Both the mean flow and eddy heat transports are positively correlated to the Bering Strait inflow discharge and the eddy transport is strongly affected by the Bering Strait inflow density. A cooler and saltier inflow leads to a higher under ice eddy heat flux in the transition zone between partial and full ice cover but a reduced eddy heat flux in the transition zone between open water and partial ice. The integrated heat fluxes along the modeled ice edge are significant: lateral eddy transport of heat is as large as 2 TW, of which 50% is fluxed upwards into the near-surface MW.

The MWTZ is an eddy-dominated zone where instabilities are induced primarily by the cross-front density difference, and the inflow density can be used to estimate the under-ice eddy

transport. In contrast, the SWTZ eddy transport efficiency is enhanced by the Bering Strait inflow and the background flow discharge is more important than the inflow density in the melt-back. The eddies provide a vertical heat flux from the BSW layer to the MW layer and from the MW layer to the ice. However, the vertical heat flux from the MW layer to the ice is less than $1/10^{th}$ of the vertical heat transported from the BSW below. The vertical eddy heat transport that melts ice in the MWTZ supplies at least 30% of the total heat content variation of the MW layer, whose heat content is continually re-supplied from the BSW layer by either diffusion or the upward vertical eddy heat flux. Although the mean heat transport is northward and steered bathymetrically within the Central Channel, eddies provide a substantial proportion of the oceanic heat transport to the shelf east of the Central Channel. This mechanism is consistent with recent hydrographic and ice observations from the Chukchi shelf (Lu et al., 2015) and from the Arctic basin (Manucharyan and Thompson, 2017).

Our systematic analyses organize relationships among various factors that affect ice retreat. The results help us understand the evolution and physical and biological consequences of Chukchi ice melt. The onset of ice retreat is correlated with the summer Bering Strait heat inflow and oceanic heat uptake via ice-albedo feedbacks (Serreze et al., 2016) and the timing of a particular year's ice retreat carries ecological consequences. Nutrients do not limit Chukchi shelf primary productivity early in the spring, although leads, light, and water column stability do (Arrigo et al., 2012; Leu et al., 2015; Assmy et al., 2017; Lowry et al., 2018). An earlier ice retreat fosters an earlier, more strongly illuminated ocean realm, and ice melt increases the near-surface stratification but decreases the inorganic nutrient concentrations. In aggregate these mechanisms may help control the onset, evolution and even composition of early season pelagic phytoplankton and zooplankton blooms (Hunt et al, 2002; Matrai and Apollonio, 2013) within

the SWTZ and MWTZ. Frontal systems associated with the ice melt can aggregate passively drifting plankton, eggs, and larvae. Upper trophic level animals also are impacted by ice meltback timing and location, including walrus, seals and whales (e.g., Jay et al., 2017).

The insights gained from this study and our approach to diagnosing the sea ice melt can be applied to other polar shelf regions, including the western branch of the Bering Strait inflow that is directed toward Herald Canyon. On the other side of the Arctic, the Atlantic inflow though Hopen Deep on the Barents Shelf leads to similar upper-layer hydrography and ice features (Ivanov et al., 2016; Koenig et al., 2017) that could be described by the mechanisms and classifications proposed in this study. Elsewhere, such as the northeastern Chukchi and Beaufort shelves (Okkonen et al., 2018) and the Barents shelf (Koenig et al., 2017), winds are believed to be the primary control on ice edge displacements. A subsequent study will focus on the linkages among winds, ice retreat, and ocean stratification.

Table 1. Definitions and characteristics of the four integrated zones. Ice concentration, ice thickness and eddy kinetic energy (EKE) are averaged over the area of each zone and also monthly averaged with (Jn) for June (model day 1 to 30), (Jl) for July (model day 31 to 60) and (A) for August (model day 61 to 90).

Characteristic		Pack Ice Zone (PIZ)	Melt Water Transition Zone (MWTZ)	Shelf Water Transition Zone (SWTZ)	Ice Free Zone (IFZ)
Position		From the northern boundary of the integration box to north of the IEMW front	Between the IEMW front and the SW front	From the SW front southward two structure function length scales (60 km)	From the southern boundary of the integration box northward to the SWTZ
Ice Concentration (%)		97(Jn), 97(Jl), 99(A)	94(Jn), 92(Jl), 94(A)	52(Jn), 38(Jl), 31(A)	22(Jn), 5(Jl), 0(A)
Ice Thickness (m)		1.93(Jn), 1.69(Jl), 1.39(A)	1.70(Jn), 1.33(Jl), 0.88(A)	0.38(Jn), 0.25(Jl), 0.12(A)	0.15(Jn), 0.01(Jl), 0.00(A)
EKE (cm^2s^{-2})		1.0±0.17 ~ 6.8±0.57 (Jn), 0.5±0.02 ~ 7.4±0.11 (Jl), 0.5±0.02 ~ 8.3±0.52 (A)	2.3±0.48 ~ 9.1±0.41 (Jn), 2.1±0.28 ~ 11.9±0.67 (Jl), 2.0±0.26 ~ 11.5±0.27 (A)	26.5±5.45 ~ 50.0±5.20 (Jn), 22.7±3.02 ~ 42.2±3.15 (Jl), 18.5±1.74 ~ 33.2±1.54 (A)	33.5±11.02 ~ 67.7±6.54 (Jn), 26.6±13.48 ~ 39.3±4.80 (Jl), 26.0±4.00 ~ 36.8±1.54 (A)
Stratification	MW	Salinity ~28 to 30 Thickness <5 m	Salinity <28 Thickness ~10-15 m	Salinity <28 Rare, only under ice floes	Absent
	BSW	Absent	Temperature ~3°C Thickness ~5-10 m blobs	Temperature >4°C Thickness ~35-45 m	Temperature = T_{inflow}: ~4, 6, 8°C Over entire depth
	WW	Thickness >45 m	Thickness ~25-40 m	Thickness <10 m blobs	Absent

Table 2. Summary of heat transport magnitudes along the modeled ice edge. The lateral flux is computed through the SW front (~600 km long and ~45 m deep) and the vertical flux is computed in the MWTZ (~600 km long and 60 km wide).

Atmospheric Heat	Ice Free Ocean	6 – 8 TW			
	Ice Covered Ocean	3 – 5 TW			
Oceanic Heat		5 – 10 TW	Lateral	Mean Flow	3 – 9.5 TW
				Eddy Lateral	0.5 – 2 TW
			Vertical	BSW to MW	~1 TW
				MW to Ice	~0.3 TW

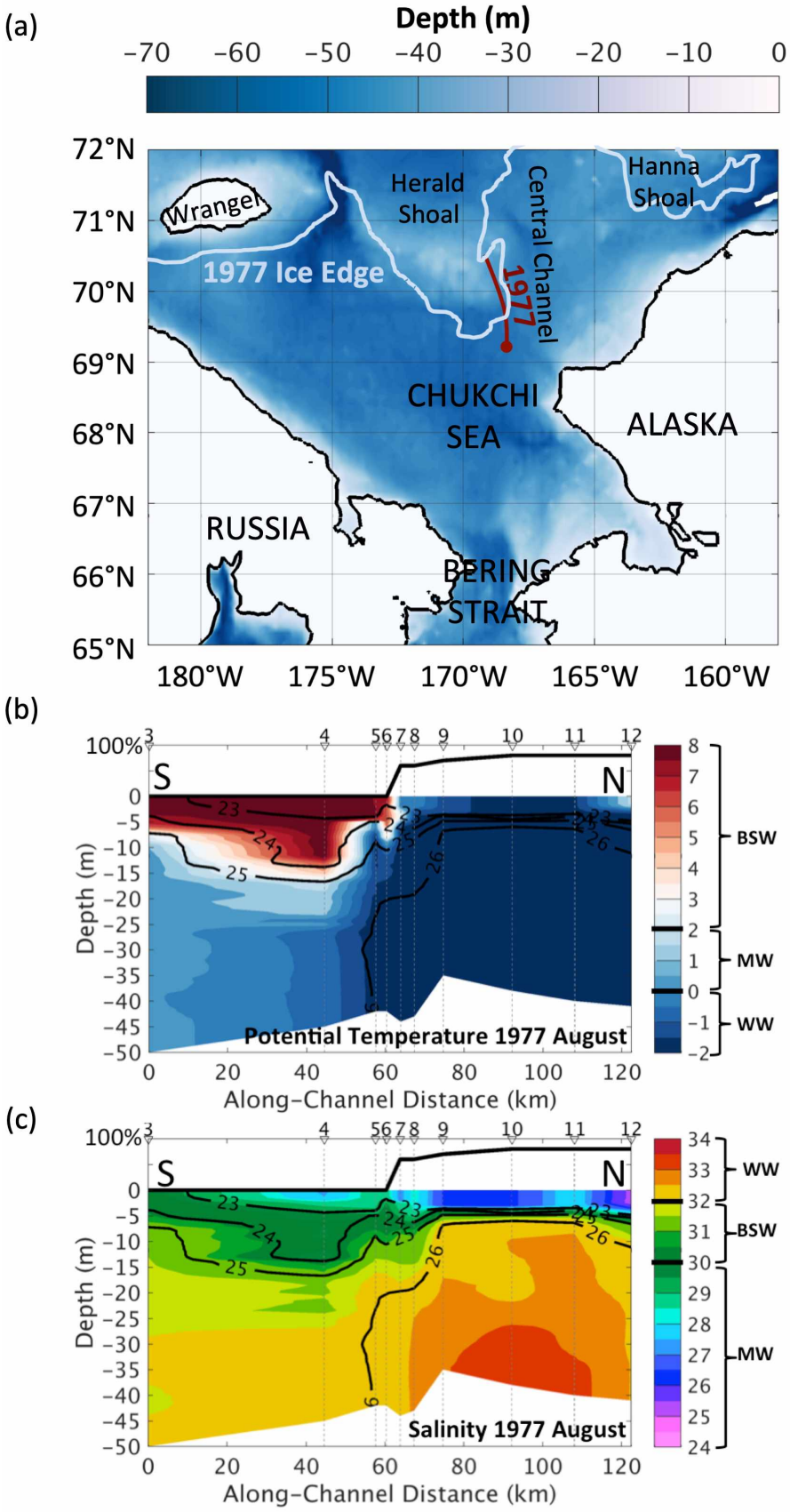
(a)
Depth (m)
−70 −60 −50 −40 −30 −20 −10 0
72°N
71°N
70°N
69°N
68°N
67°N
66°N
65°N
180°W 175°W 170°W 165°W 160°W
Wrangel
Herald Shoal
Central Channel
Hanna Shoal
1977 Ice Edge
1977
CHUKCHI SEA
ALASKA
RUSSIA
BERING STRAIT
(b)
100%
S
N
Depth (m)
Potential Temperature 1977 August
Along−Channel Distance (km)
BSW
MW
WW
(c)
Salinity 1977 August
Along−Channel Distance (km)
WW
BSW
MW

Figure 1. (a) A modification of Figure 2 in Paquette and Bourke (1981) showing the ice edge in August 1977, and depths color-coded. The red line on the map shows the location of their August 1977 meridional CTD section. The vertical sections of potential temperature and salinity (both overlain with potential density anomaly contours) from the 1977 section are shown as (b) and (c).

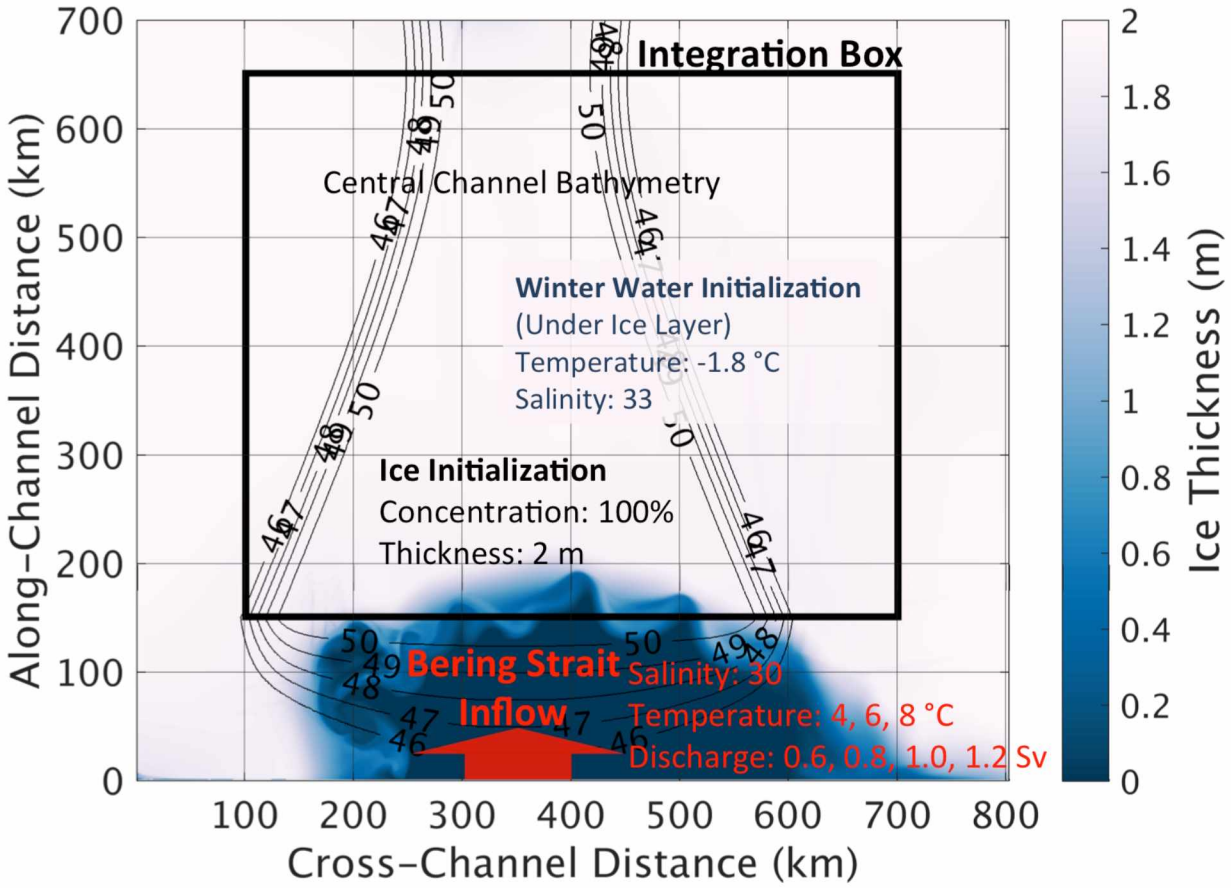

Figure 2. Model configuration, and a planview of the ice thickness at the beginning of the integration time 30 days after numerical adjustment.

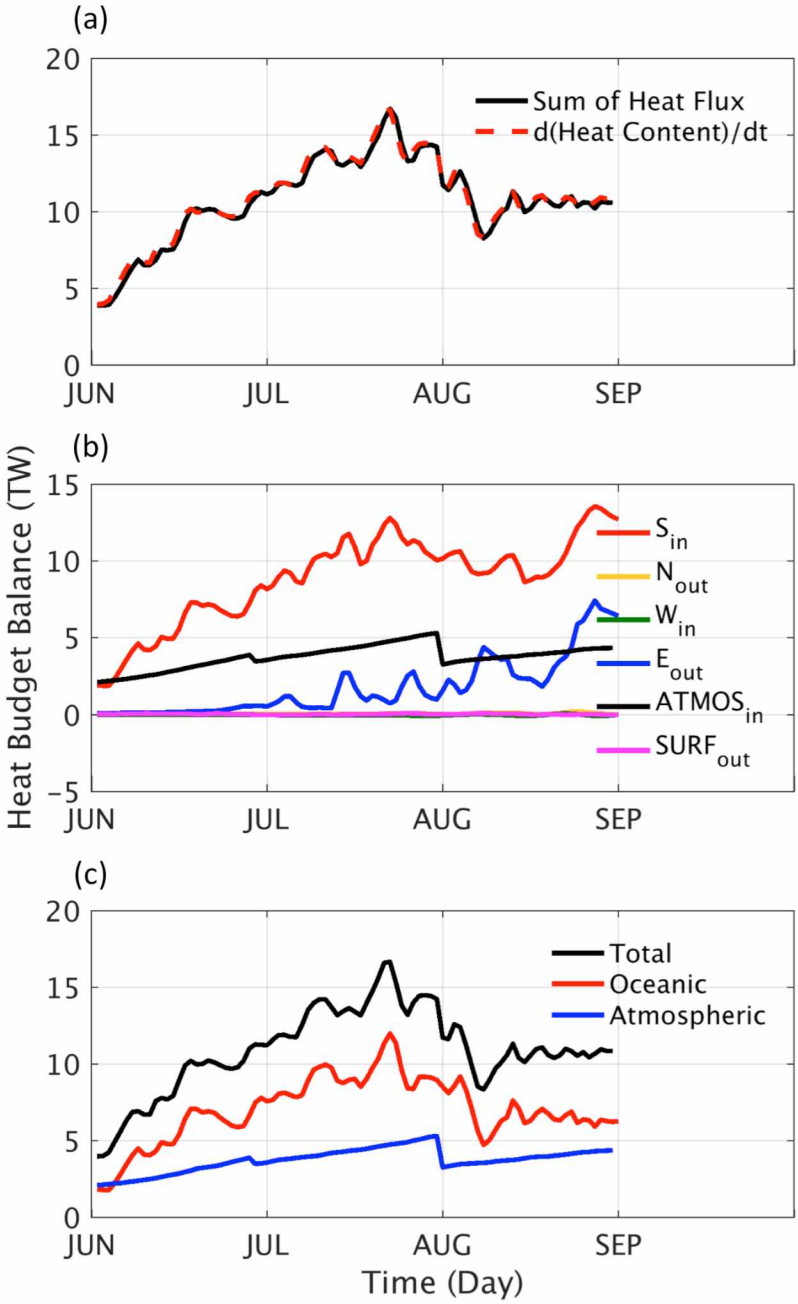

Figure 3. (a) The heat budget balance between the daily heat content and the sum of the heat fluxes across the five sides of the integration box. (b) The six terms on the right-hand side of the heat budget (Eq.3.1). (c) The total heat budget along with the oceanic and atmospheric heating contributions.

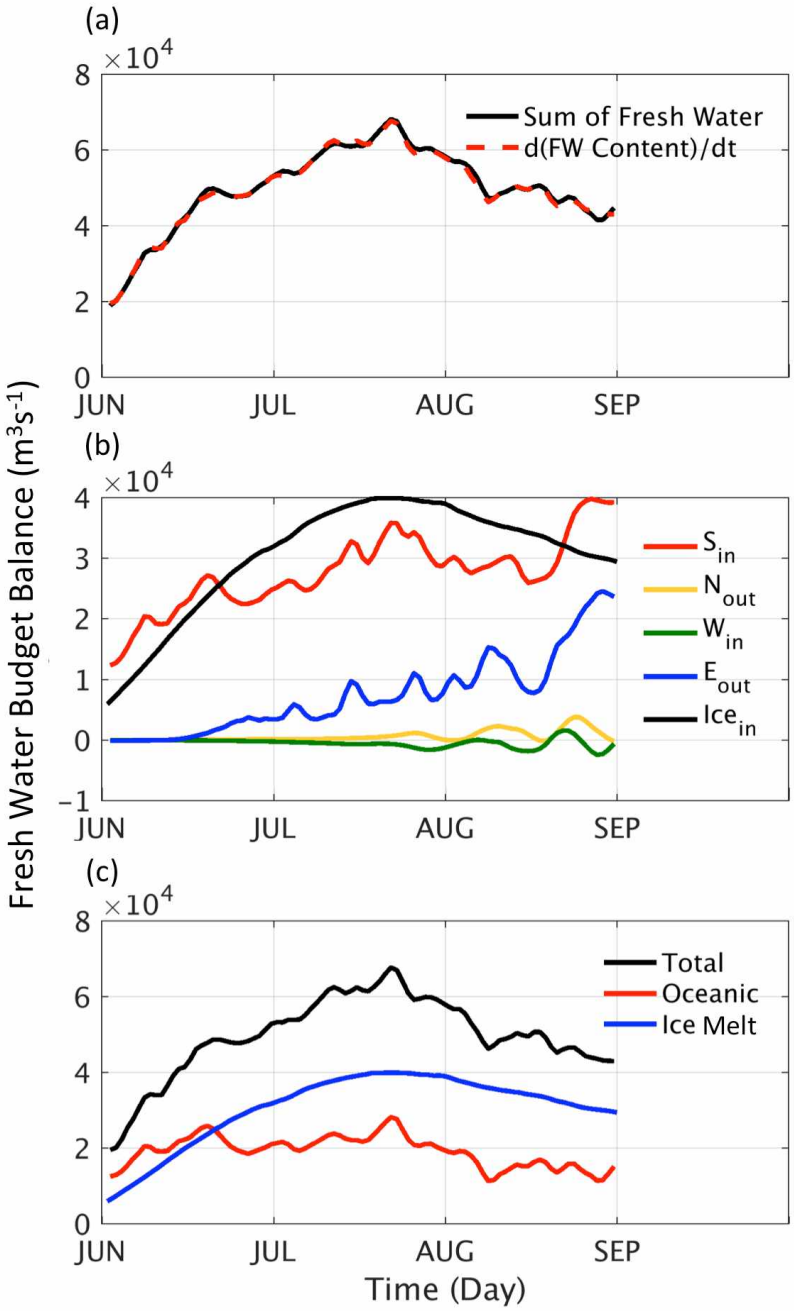

Figure 4. (a) The fresh water budget balance between the daily fresh water content and the sum of the fresh water fluxes cross the five sides of integration box. (b) The five terms on the right-hand side of Eq.3.2. (c) The total fresh water budget including contributions from ice melt and the fresh water transported by the Bering Strait inflow.

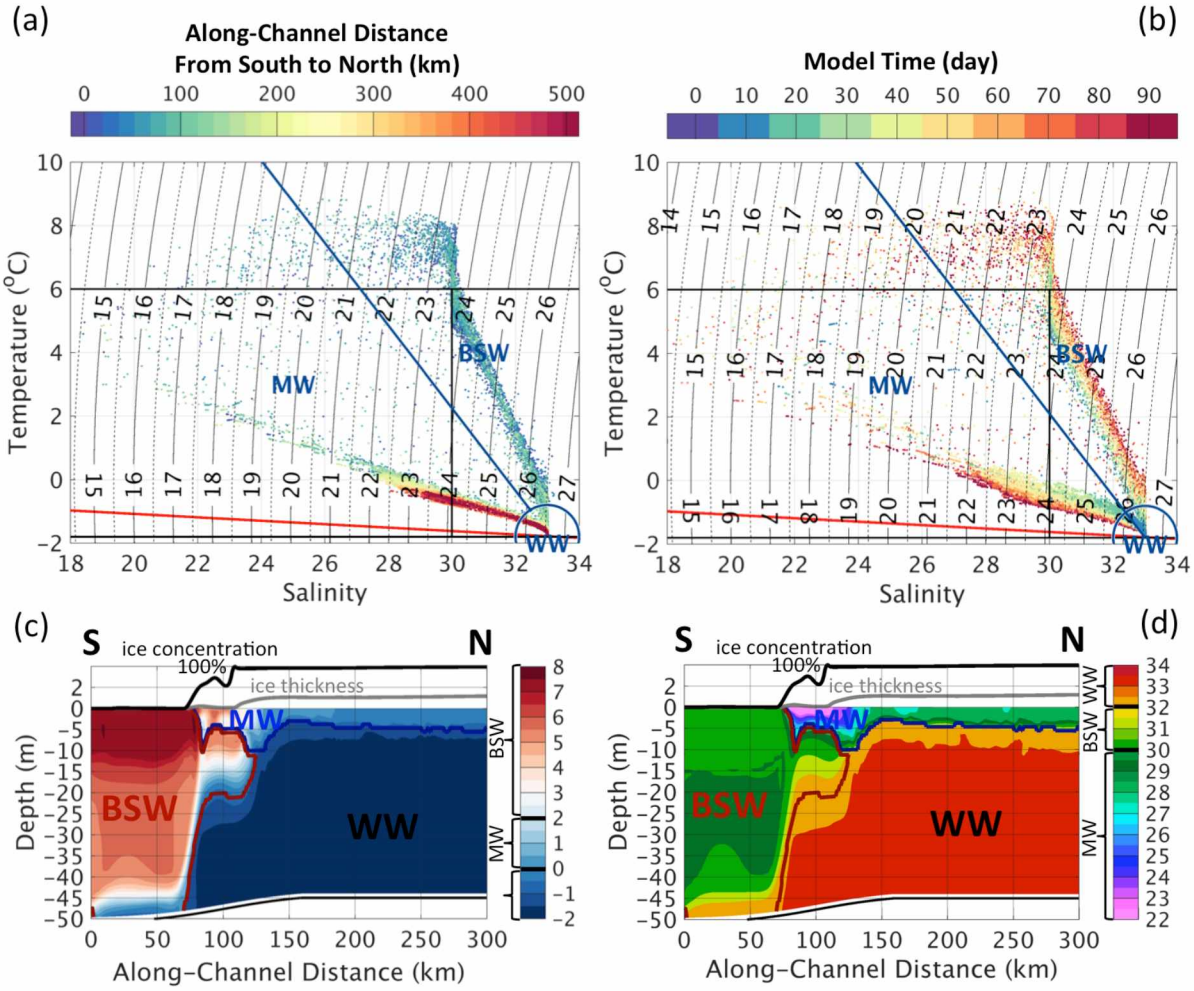

Figure 5. T-S diagram of model results with a Bering Strait inflow temperature of 6°C and the threshold (blue lines and half circle) to classify the three major water masses on Chukchi Shelf (MW, BSW and WW). The T-S diagram in (a) is plotted after 70 model days with colors indicating positions of the water types according to along-channel distance (y-, km). The T-S diagram in (b) is plotted every 10 days through the entire model integration (90 days) with colors indicating the integration time (day). Figures (c) and (d) are vertical sections of temperature and salinity, respectively, and the water mass classification results on day 70 of the model run for a Bering Strait inflow temperature of 6°C. The locations of the sections are shown in Figure 6(b) by the gray dashed line at x= 450 km. The red contours delineate BSW and the blue contours

delineate MW. The thick gray lines in sections (b) and (c) above depth 0 m denote the ice thickness, which ranges from 0 to ~2 m. The thick black lines denote ice concentration, which ranges from 0 to 100%. Ice thickness decreases coincident with the presence of very fresh (S<28) MW.

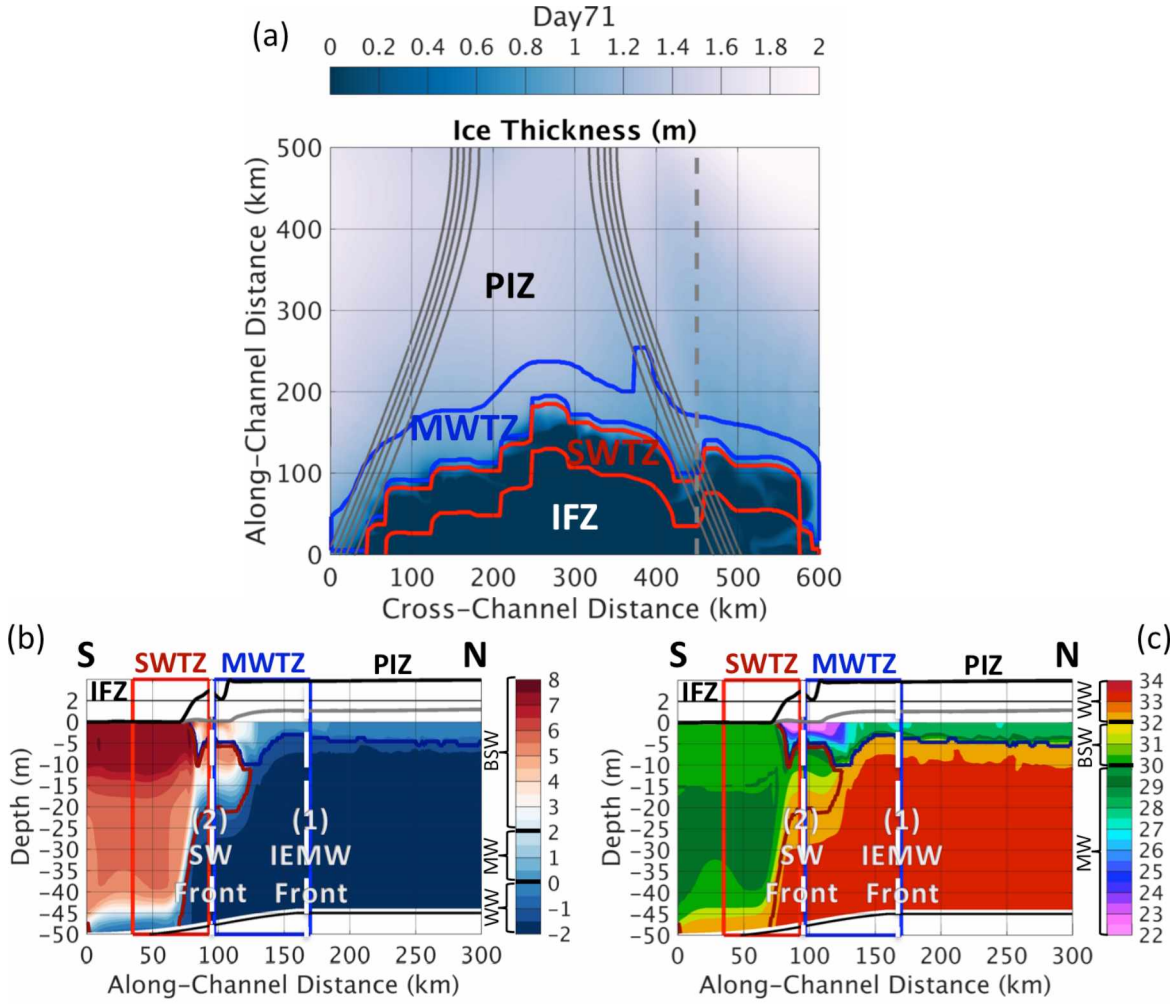

Figure 6. (a) Planview snapshot of ice thickness on day 70, with the location of the transition zones defined by the IEMW and SW fronts, which are denoted by the white dashed lines in (b) and (c). Panels (b) and (c) are temperature and salinity transects, respectively at x = 450 km as indicated by the gray dashed line in (a). The blue line delineates the MWTZ, the red line delineates the SWTZ.

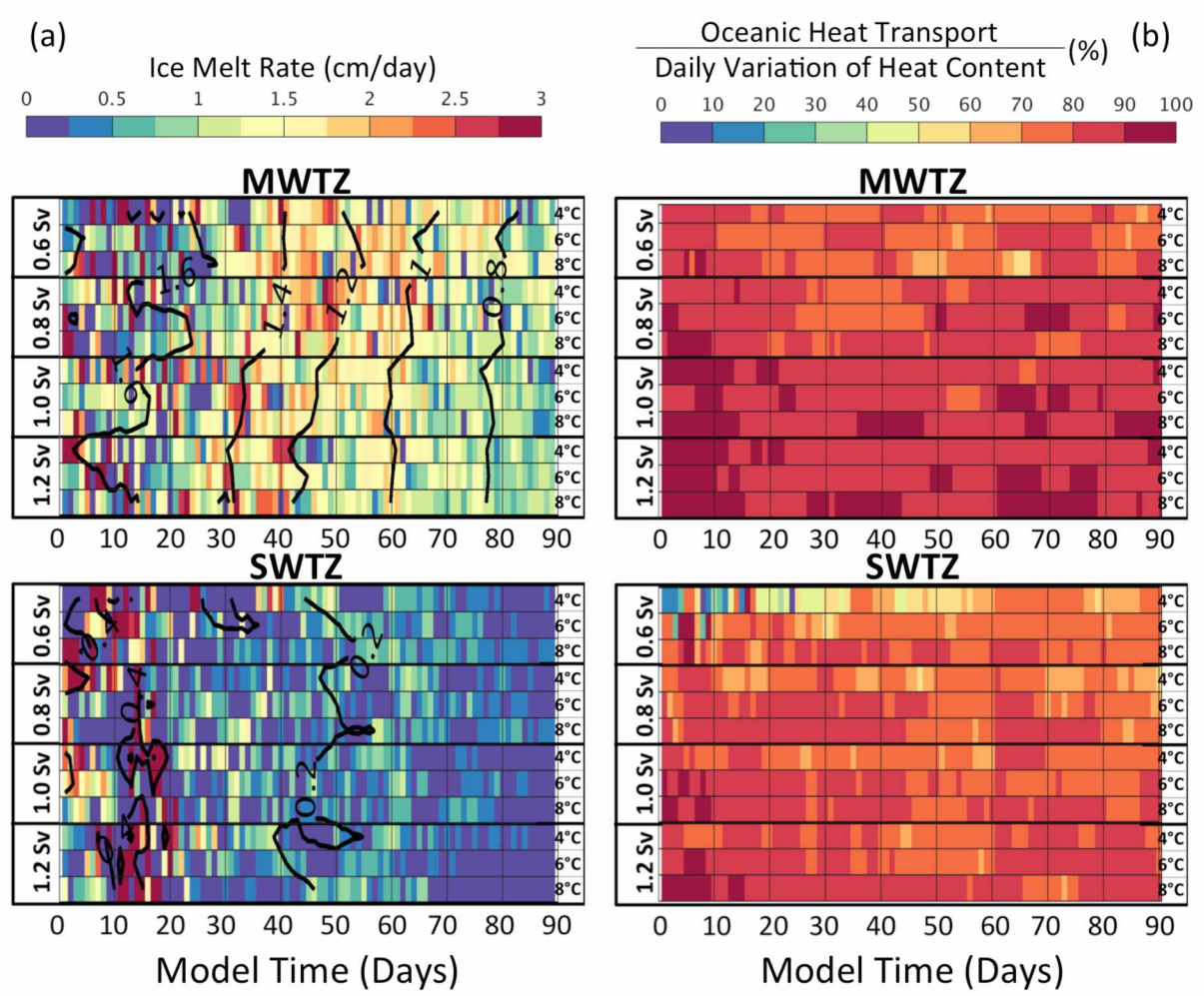

Figure 7. (a) The ice melt rate (color-coded) overlain on the area-averaged ice thickness (black contours) and (b) the contribution of oceanic heat transport to the daily variation of heat content for 12 combinations of inflow discharge of 0.6, 0.8, 1.0, 1.2 Sv (top to bottom in each zone by thick black horizontal lines) and BSW temperatures of 4, 6, 8 °C (top to bottom in each discharge segment and separated by thin black thin lines) integrated over the MWTZ and SWTZ.

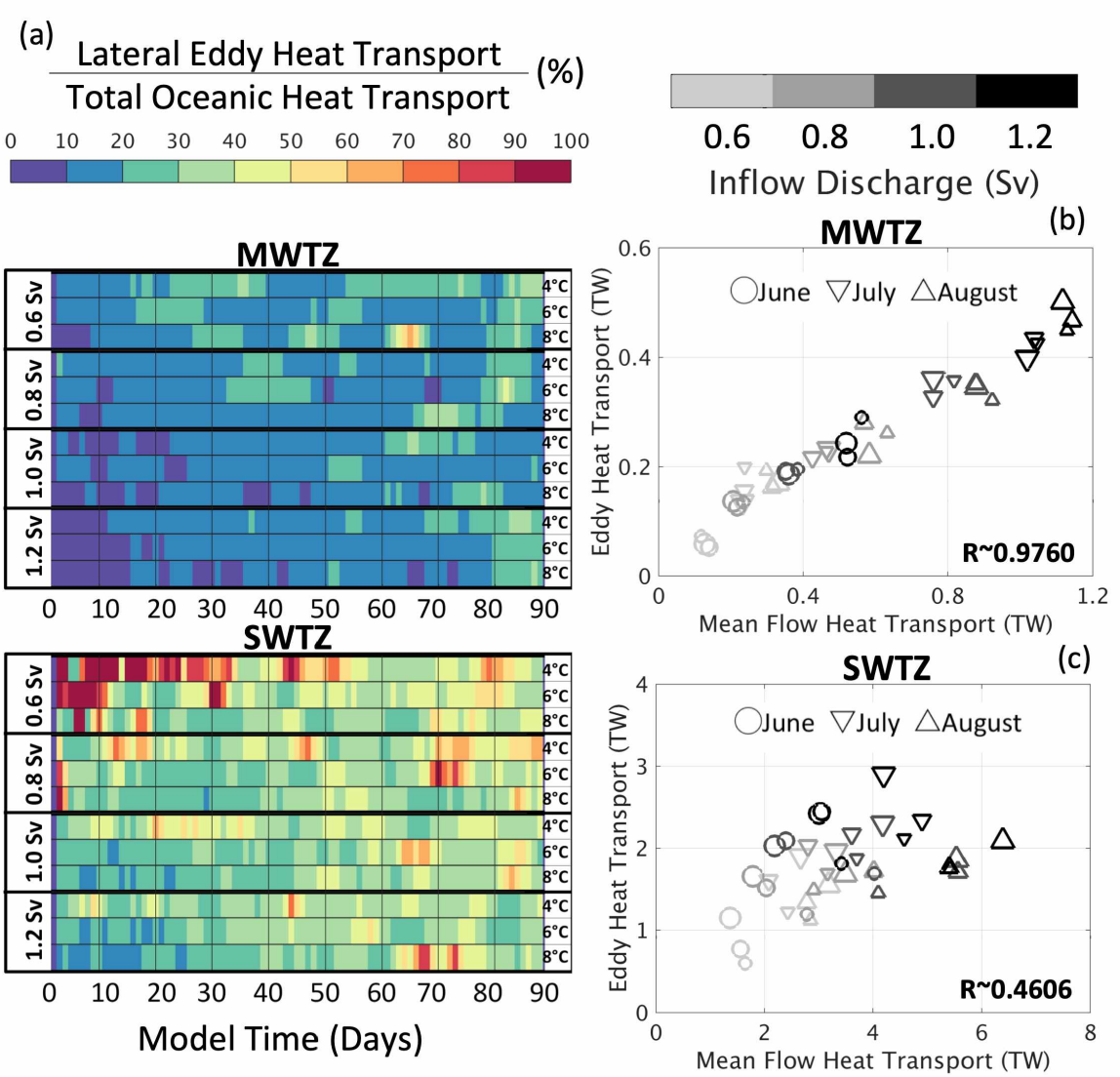

Figure 8. (a) The contribution of the eddy heat transport to the total oceanic heat transport for 12 combinations of inflow discharge of 0.6, 0.8, 1.0, 1.2 Sv (top to bottom in each zone separated by thick black lines) and BSW temperatures of 4, 6, 8 °C (top to bottom in each discharge set separated by thin black lines) integrated over the MWTZ and SWTZ. Panels (b) and (c) show the monthly-averaged mean flow heat transport and eddy heat transport in the MWTZ and the SWTZ, respectively. The small to large size of the markers indicates inflow temperatures of 4, 6 and 8°C, respectively. The grayscale corresponds to the inflow discharge magnitudes and the symbol shapes indicate different monthly averages.

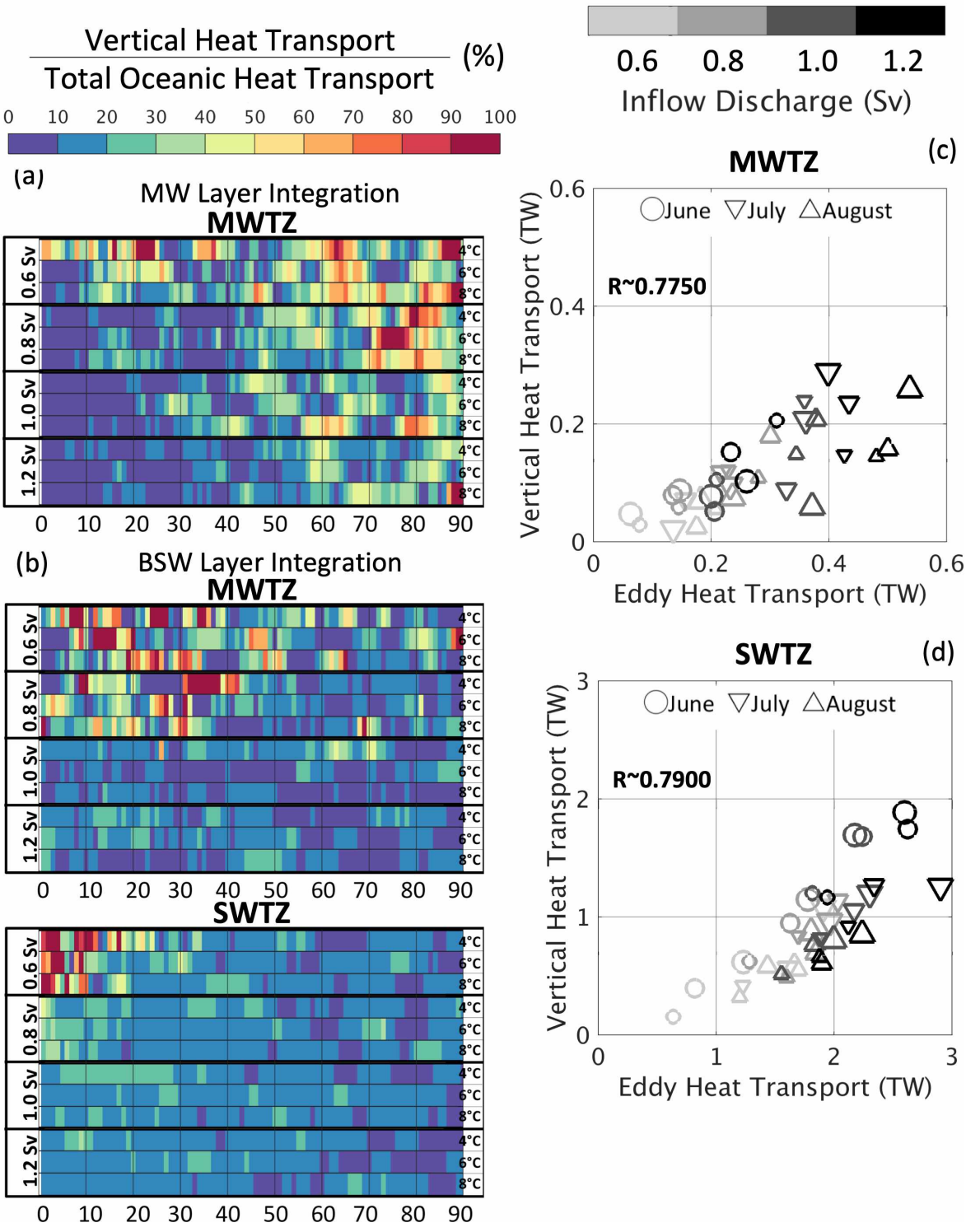

Figure 9. Panels (a) and (b) show the vertical heat transport as a proportion of the total lateral oceanic heat transport for 12 combinations of inflow discharges of 0.6, 0.8, 1.0, 1.2 Sv (top to bottom in each zone separated by thick black lines) and BSW temperatures of 4, 6, 8 °C (top to

bottom in each discharge set separated by thin black thin lines) integrated over the surface MW layer in (a) and the subsurface BSW layer in (b) separately for the MWTZ and SWTZ. Panels (c) and (d) show the relationship between the eddy heat transport and the vertical heat transport. The large-to-small size of the symbols markers indicates inflow temperatures of 4, 6 and 8°C, respectively. Inflow discharges are denoted by the grayscale colorbar and the shapes indicate different monthly averages.

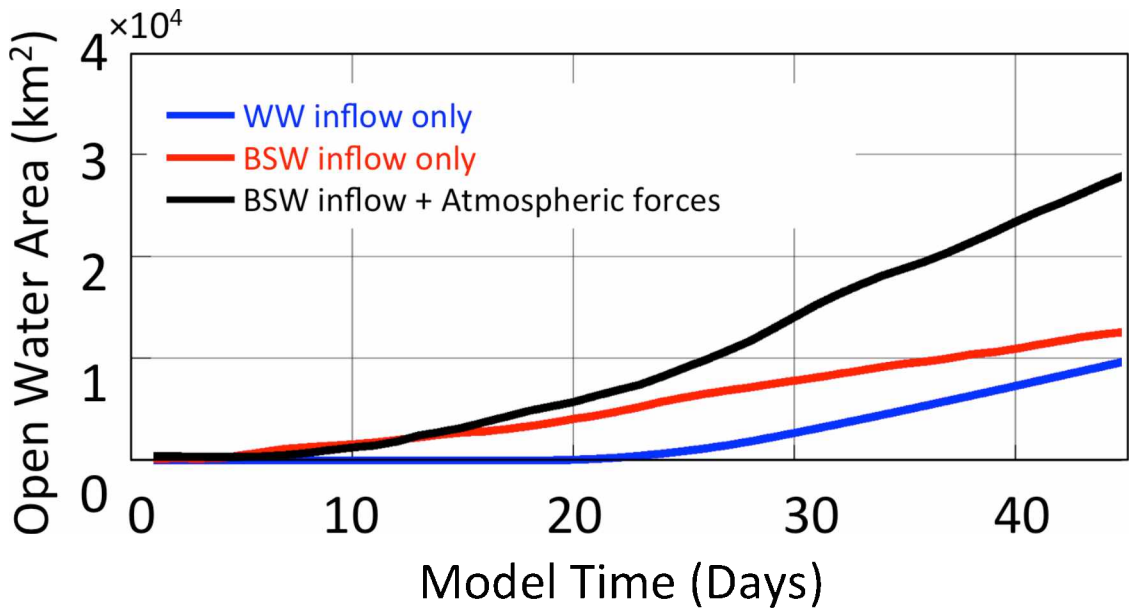

Figure 10. Time series of total open water area for various combinations of inflows with and without atmospheric heating. The blue line is the open water evolution due only to ice advection for an inflow having Winter Water (WW, T = -1.8°C, S = 33) properties and no atmospheric heating. The red line is the open water area due to an inflow of Bering Sea Water (BSW) with T = 6°C and S = 30 and no atmospheric heating. The black line is the standard run with BSW inflow and atmospheric forces. All inflow rates are 0.8 Sv.

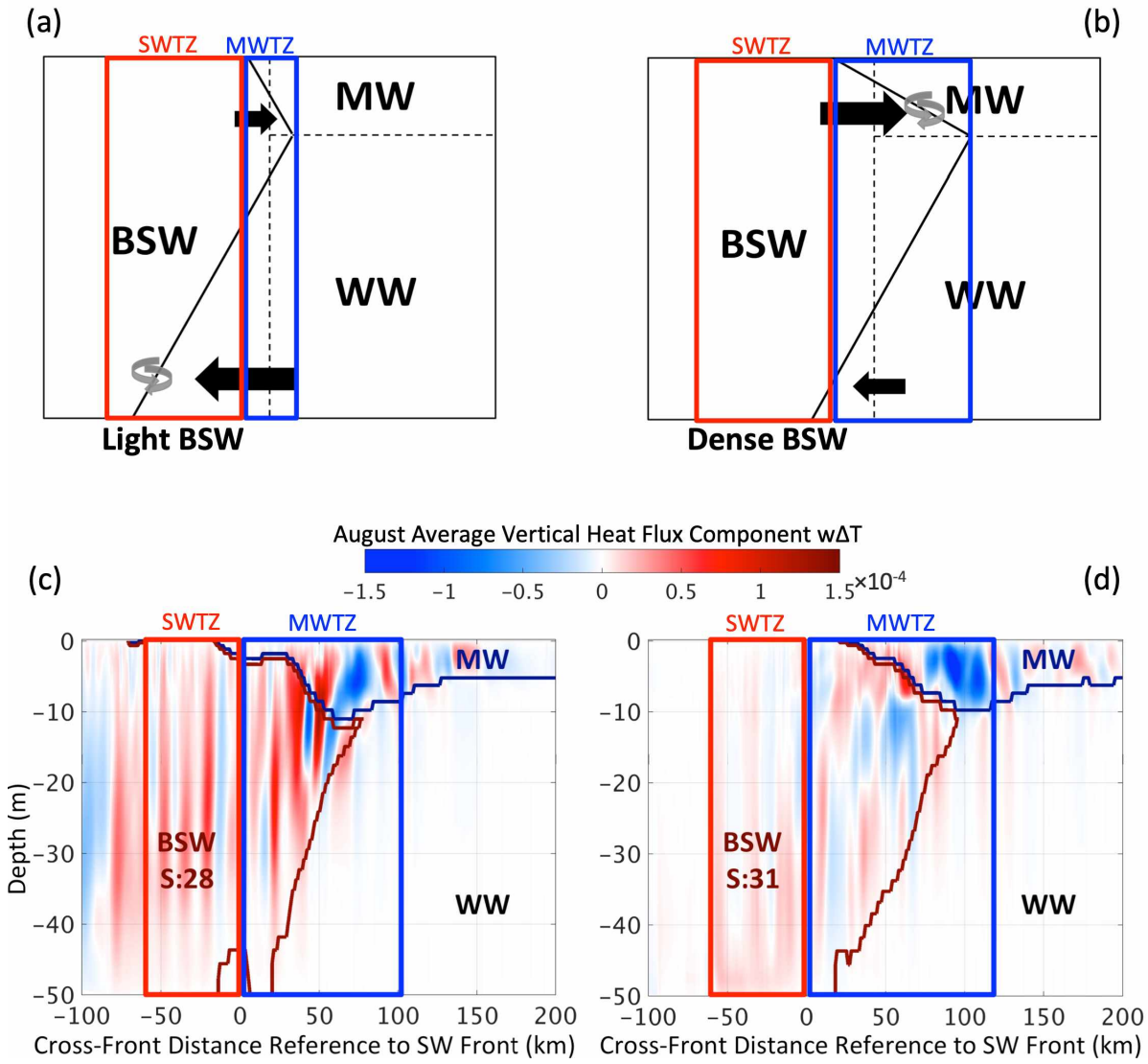

Figure 11. Panels (a) and (b) are schematics showing how water mass interactions differ in the SWTZ and the MWTZ. Changes in BSW density lead to different eddy energy intensities in each region. Panels (c) and (d) are monthly-averaged vertical heat transport components, $w\Delta T$, on the transect across x=450 km within the Central Channel. The inflow salinity is 28 and 31 in (a, c) and (b, d), respectively.

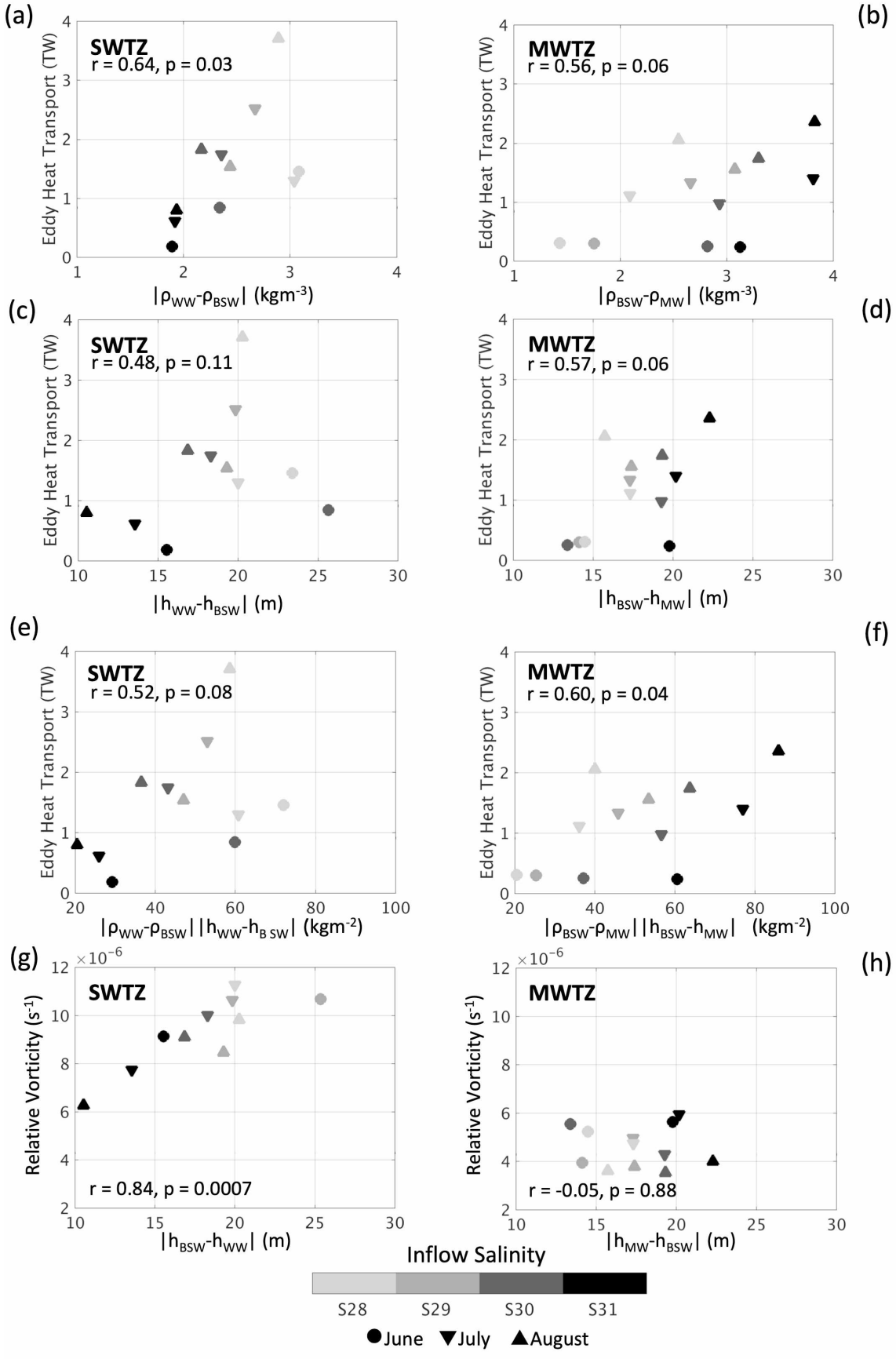
(a)
SWTZ
r = 0.64, p = 0.03
Eddy Heat Transport (TW)
|ρWW-ρBSW| (kgm-3)
(b)
MWTZ
r = 0.56, p = 0.06
|ρBSW-ρMW| (kgm-3)
(c)
SWTZ
r = 0.48, p = 0.11
|hWW-hBSW| (m)
(d)
MWTZ
r = 0.57, p = 0.06
|hBSW-hMW| (m)
(e)
SWTZ
r = 0.52, p = 0.08
|ρWW-ρBSW||hWW-hB SW| (kgm-2)
(f)
MWTZ
r = 0.60, p = 0.04
|ρBSW-ρMW||hBSW-hMW| (kgm-2)
(g)
SWTZ
Relative Vorticity (s-1)
×10-6
r = 0.84, p = 0.0007
|hBSW-hWW| (m)
(h)
MWTZ
r = -0.05, p = 0.88
|hMW-hBSW| (m)
Inflow Salinity
S28
S29
S30
S31
June
July
August

Figure 12. Panels (a) and (b) show the relationship between cross-frontal density differences and eddy heat transport, where the density difference is calculated by BSW and MW for MWTZ in (a) and by BSW and WW for SWTZ in (b). Panels (c) and (d) show the relationship between eddy heat transport and layer thickness difference of the fronts (BSW and MW for MWTZ, BSW and WW for SWTZ), which mainly interacts with the BSW front. Panels (e) and (f) show the relationship between the eddy heat transport and the product of the density difference and layer thickness difference, i.e. the two sides of Eq. 5.1. Panels (g) and (h) show the relationship between relative vorticity and layer thickness difference. Symbol colors correspond to the Bering Strait inflow salinity shown by the colorbar and symbol type corresponds to different monthly averages.

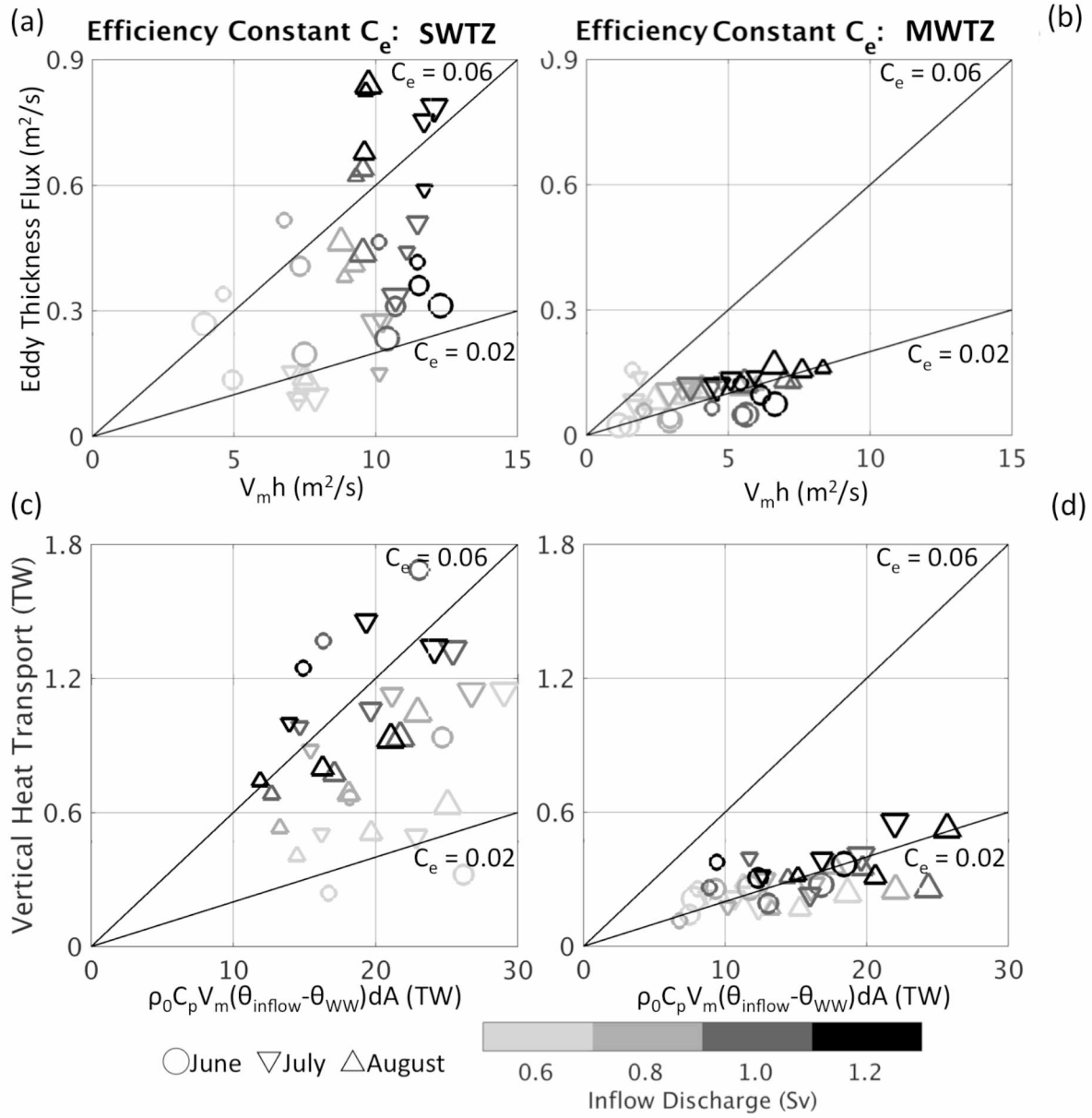

Figure 13. Panels (a) and (b) show the relationship between the scale of the along-front thickness flux and the eddy thickness flux for the calculation of the efficiency constant. Panels (c) and (d) show the relationship between the scale of the along-front heat transport and the vertical heat transport supported by eddies for the calculation of the efficiency constant.

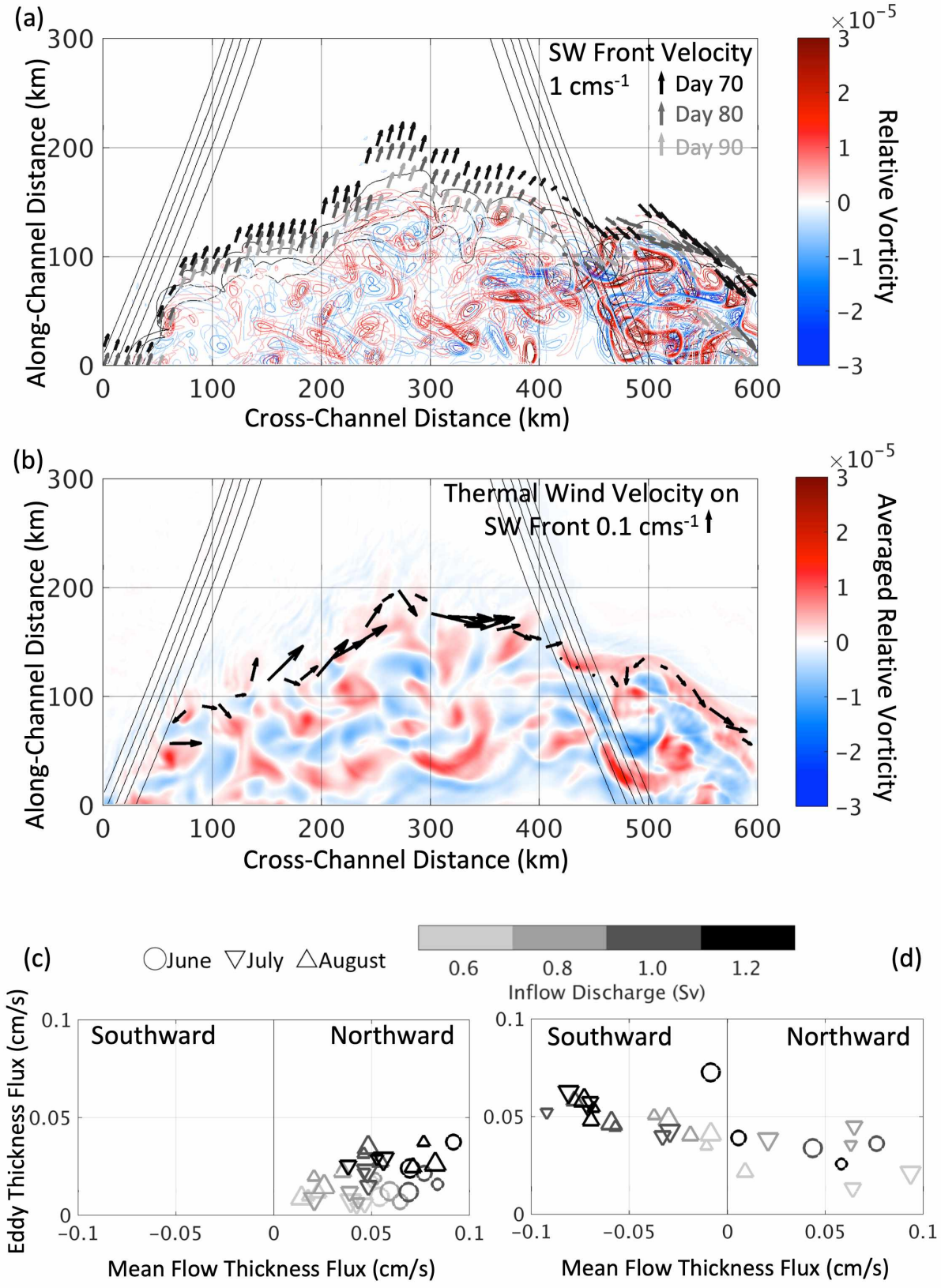
(a)
SW Front Velocity
1 cms-1
Day 70
Day 80
Day 90
Along-Channel Distance (km)
Cross-Channel Distance (km)
Relative Vorticity
×10−5
(b)
Thermal Wind Velocity on
SW Front 0.1 cms-1
Along-Channel Distance (km)
Cross-Channel Distance (km)
Averaged Relative Vorticity
×10−5
(c)
June
July
August
Inflow Discharge (Sv)
Southward
Northward
Eddy Thickness Flux (cm/s)
Mean Flow Thickness Flux (cm/s)
(d)
Southward
Northward
Mean Flow Thickness Flux (cm/s)

Figure 14. Panel (a) is a planview of relative vorticity at day 70, overlapped by model runs at days 80 and 90 using progressively lighter colors. Arrows show the SW front velocity on the SW front position at model day 70, 80 and 90 as indicated by the legend color shading. Panel (b) is a planview of the monthly-averaged relative vorticity overlain with the monthly-averaged thermal wind velocity on the SW front for August. The gray thin contours show the Central Channel bathymetry in (a) and (b). Panels (c; depth>45 m within the Central Channel) and (d; depth<45 m east of the Channel), show the relationship between eddy thickness fluxes and mean flow thickness flux, which are averaged across the combined area of the MWTZ and the SWTZ.

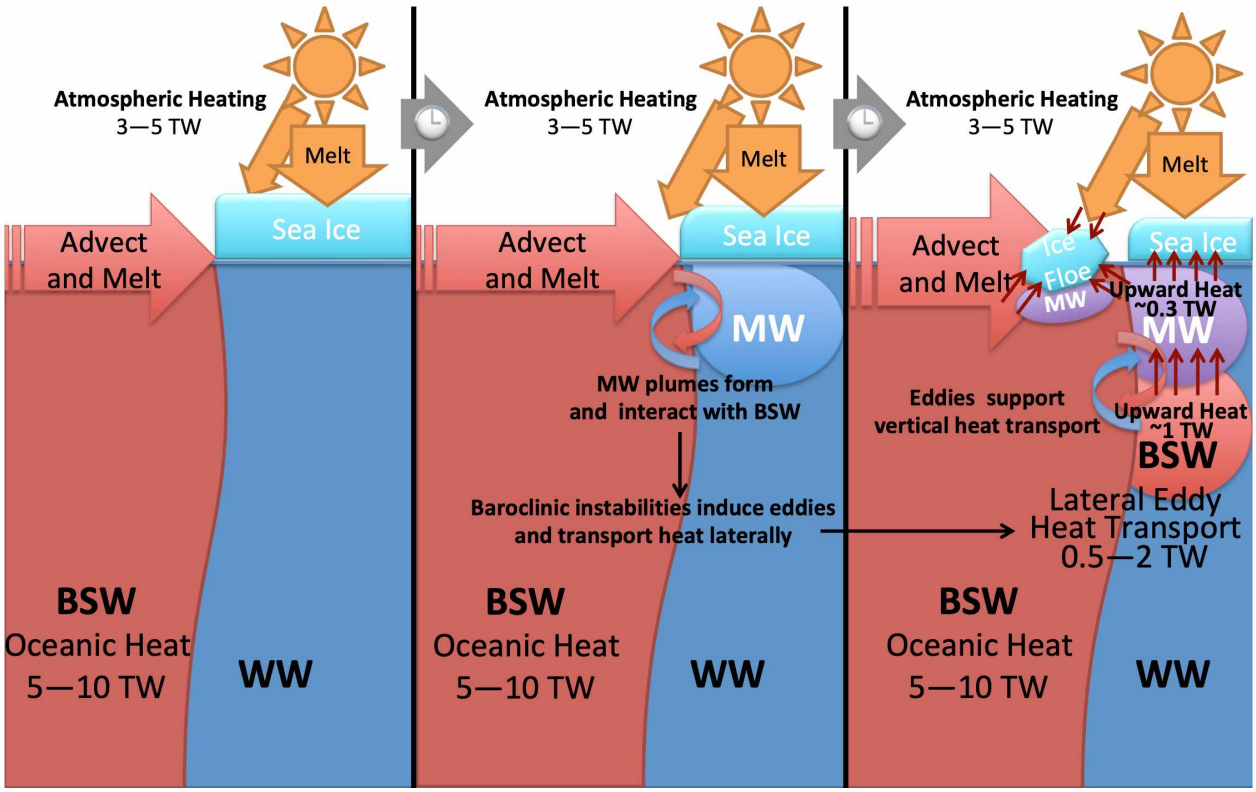

Figure 15. Schematic cartoon showing the role of oceanic heat fluxes on ice ablation.

References

Arrigo, K. R., Perovich, D. K., Pickart, R. S., Brown, Z. W., Van Dijken, G. L., Lowry, K. E., ... & Bates, N. R. (2012). Massive phytoplankton blooms under Arctic sea ice. *Science*, 336(6087), 1408-1408.

Assmy, P., Fernández-Méndez, M., Duarte, P., Meyer, A., Randelhoff, A., Mundy, C. J., ... & Cohen, L. (2017). Leads in Arctic pack ice enable early phytoplankton blooms below snow-covered sea ice. *Scientific Reports*, 7, 40850.

Badin, G., Williams, R. G., Holt, J. T., & Fernand, L. J. (2009). Are mesoscale eddies in shelf seas formed by baroclinic instability of tidal fronts? *Journal of Geophysical Research: Oceans, 114*(C10).

Bockstoce, J. R. (1986). Whales, ice, and men: the history of whaling in the western Arctic. *Seattle: University of Washington Press*, p.62

Bourke, R. H. (1983). Currents, fronts and fine structure in the marginal ice zone of the Chukchi Sea. *Polar Record*, 21(135), 569-575.

Durski, S. M., Glenn, S. M., & Haidvogel, D. B. (2004). Vertical mixing schemes in the coastal ocean: Comparison of the level 2.5 Mellor-Yamada scheme with an enhanced version of the K profile parameterization. *Journal of Geophysical Research: Oceans*, 109(C1).

Frey, K. E., Maslanik, J. A., Kinney, J. C., & Maslowski, W. (2014). Recent variability in sea ice cover, age, and thickness in the Pacific Arctic region. *In The Pacific Arctic Region* (pp. 31-63). Springer, Dordrecht.

Fukamachi, Y., Ohshima, K. I., & Ishikawa, T. I. (1998). Mesoscale ice features in the summer marginal ice zone off East Queen Maud Land observed in NOAA AVHRR imagery. *American Geophysical Union (AGU)*, pp. 317-323.

Galperin, B., Kantha, L. H., Hassid, S., & Rosati, A. (1988). A quasi-equilibrium turbulent energy model for geophysical flows. *Journal of the Atmospheric Sciences*, 45(1), 55-62.

Gawarkiewicz, G., Brink, K. H., Bahr, F., Beardsley, R. C., Caruso, M., Lynch, J. F., & Chiu, C. S. (2004). A large amplitude meander of the shelfbreak front during summer south of New England: Observations from the Shelfbreak PRIMER experiment. *Journal of Geophysical Research: Oceans, 109*(C3).

Haine, T. W., & Marshall, J. (1998). Gravitational, symmetric, and baroclinic instability of the ocean mixed layer. *Journal of Physical Oceanography*, *28*(4), 634-658.

Hedstrom, K. (2018). Technical Manual for a Coupled Sea-Ice/Ocean Circulation Model (Version 5). U.S. Dept. of the Interior, Bureau of Ocean Energy Management, Alaska OCS Region. *OCS Study BOEM 2018-007*. 182 pp.

Hunke, E. C., & Dukowicz, J. K. (1997). An elastic–viscous–plastic model for sea ice dynamics. *Journal of Physical Oceanography*, 27(9), 1849-1867.

Hunke, E. C. (2001). Viscous–plastic sea ice dynamics with the EVP model: Linearization issues. *Journal of Computational Physics*, 170(1), 18-38.

Hunt Jr, G. L., Stabeno, P., Walters, G., Sinclair, E., Brodeur, R. D., Napp, J. M., & Bond, N. A. (2002). Climate change and control of the southeastern Bering Sea pelagic ecosystem. *Deep Sea Research Part II: Topical Studies in Oceanography*, 49(26), 5821-5853.

Ivanov, V., Alexeev, V., Koldunov, N. V., Repina, I., Sandø, A. B., Smedsrud, L. H., & Smirnov, A. (2016). Arctic Ocean heat impact on regional ice decay: A suggested positive feedback. *Journal of Physical Oceanography*, 46(5), 1437-1456.

Jay, C. V., Taylor, R. L., Fischbach, A. S., Udevitz, M. S., & Beatty, W. S. (2017). Walrus haul-out and in water activity levels relative to sea ice availability in the Chukchi Sea. *Journal of Mammalogy*, 98(2), 386-396.

Johannessen, O. M., Sandven, S., Budgell, W. P., Johannessen, J. A., & Shuchman, R. A. (1994). Observation and simulation of ice tongues and vortex pairs in the marginal ice zone. *American Geophysical Union (AGU)*.

Kantha, L. H., & Clayson, C. A. (1994). An improved mixed layer model for geophysical applications. *Journal of Geophysical Research: Oceans*, 99(C12), 25235-25266.

Koenig, Z., Provost, C., Villacieros Robineau, N., Sennéchael, N., Meyer, A., Lellouche, J. M., & Garric, G. (2017). Atlantic waters inflow north of Svalbard: Insights from IAOOS observations and Mercator Ocean global operational system during N-ICE2015. *Journal of Geophysical Research: Oceans*, 122(2), 1254-1273.

Kuzmina, N. (2016). Generation of large-scale intrusions at baroclinic fronts: an analytical consideration with a reference to the Arctic Ocean. *Ocean Science, 12*(6), 1269-1277.

Lee, T. N., Atkinson, L. P., & Legeckis, R. (1981). Observations of a Gulf Stream frontal eddy on the Georgia continental shelf, April 1977. *Deep Sea Research Part A. Oceanographic Research Papers, 28*(4), 347-378.

Leu, E., Mundy, C. J., Assmy, P., Campbell, K., Gabrielsen, T. M., Gosselin, M., ... & Gradinger, R. (2015). Arctic spring awakening–Steering principles behind the phenology of vernal ice algal blooms. *Progress in Oceanography*, 139, 151-170.

Lowry, K. E., Pickart, R. S., Selz, V., Mills, M. M., Pacini, A., Lewis, K. M., ... & Ferland, J. (2018). Under-ice phytoplankton blooms inhibited by spring convective mixing in refreezing leads. *Journal of Geophysical Research: Oceans*, 123(1), 90-109.

Lu, K., Weingartner, T., Danielson, S., Winsor, P., Dobbins, E., Martini, K., & Statscewich, H. (2015). Lateral mixing across ice meltwater fronts of the Chukchi Sea shelf. *Geophysical Research Letters*, *42*(16), 6754-6761.

Manucharyan, G. E., & Thompson, A. F. (2017). Submesoscale Sea Ice-Ocean Interactions in Marginal Ice Zones. *Journal of Geophysical Research: Oceans, 122*(12), 9455-9475.

Martin, S., & Drucker, R. (1997). The effect of possible Taylor columns on the summer ice retreat in the Chukchi Sea. *Journal of Geophysical Research: Oceans, 102*(C5), 10473-10482.

Matrai, P., & Apollonio, S. (2013). New estimates of microalgae production based upon nitrate reductions under sea ice in Canadian shelf seas and the Canada Basin of the Arctic Ocean. *Marine Biology*, 160(6), 1297-1309.

May, B. D., & Kelley, D. E. (2001). Growth and steady state stages of thermohaline intrusions in the Arctic Ocean. *Journal of Geophysical Research: Oceans, 106*(C8), 16783-16794.

Mellor, G. L., & Kantha, L. (1989). An ice-ocean coupled model. *Journal of Geophysical Research: Oceans*, 94(C8), 10937-10954.

Mellor, G. L., & Yamada, T. (1982). Development of a turbulence closure model for geophysical fluid problems. *Reviews of Geophysics*, 20(4), 851-875.

Mesinger, F., DiMego, G., Kalnay, E., Mitchell, K., Shafran, P. C., Ebisuzaki, W., ... & Ek, M. B. (2006). North American regional reanalysis. *Bulletin of the American Meteorological Society*, 87(3), 343-360.

Okkonen, S., Ashjian, C., Campbell, R. G., & Alatalo, P. (2018). The encoding of wind forcing into the Pacific-Arctic pressure head, Chukchi Sea ice retreat and late-summer Barrow Canyon water masses. *Deep Sea Research Part II: Topical Studies in Oceanography*, 162, 22-31.

Paquette, R. G., & Bourke, R. H. (1981). Ocean circulation and fronts as related to ice melt back in the Chukchi Sea. *Journal of Geophysical Research: Oceans, 86*(C5), 4215-4230.

Pickart, R. S., Moore, G. W. K., Mao, C., Bahr, F., Nobre, C., & Weingartner, T. J. (2016). Circulation of winter water on the Chukchi shelf in early summer. *Deep Sea Research Part II: Topical Studies in Oceanography*, 130, 56-75.

Serreze, M. C., Crawford, A. D., Stroeve, J. C., Barrett, A. P., & Woodgate, R. A. (2016). Variability, trends, and predictability of seasonal sea ice retreat and advance in the Chukchi Sea. *Journal of Geophysical Research: Oceans*, 121(10), 7308-7325.

Shchepetkin, A. F., & McWilliams, J. C. (2005). The regional oceanic modeling system (ROMS): a split-explicit, free-surface, topography-following-coordinate oceanic model. *Ocean Modelling*, 9(4), 347-404.

Shuchman, R. A., Onstott, R. G., Johannessen, O. M., Sandven, S., & Johannessen, J. A. (2004). Processes at the ice edge: The Arctic. *Synthetic Aperture Radar Marine User's Manual*, 373-395.

Spall, M. A. (2007). Circulation and water mass transformation in a model of the Chukchi Sea. *Journal of Geophysical Research: Oceans*, *112*(C5).

Spall, M. A., & Chapman, D. C. (1998). On the efficiency of baroclinic eddy heat transport across narrow fronts. *Journal of Physical Oceanography*, *28*(11), 2275-2287.

Strong, C., Foster, D., Cherkaev, E., Eisenman, I., & Golden, K. M. (2017). On the definition of marginal ice zone width. *Journal of Atmospheric and Oceanic Technology*, 34(7), 1565-1584.

Waseda, T., & Mitsudera, H. (2002). Chaotic advection of the shallow Kuroshio coastal waters. *Journal of Oceanography, 58*(5), 627-638.

Waseda, T., Mitsudera, H., Taguchi, B., & Yoshikawa, Y. (2002). On the eddy Kuroshio interaction: Evolution of the mesoscale eddy. *Journal of Geophysical Research: Oceans, 107*(C8).

Weingartner, T., Aagaard, K., Woodgate, R., Danielson, S., Sasaki, Y., & Cavalieri, D. (2005). Circulation on the north central Chukchi Sea shelf. *Deep Sea Research Part II: Topical Studies in Oceanography*, *52*(24-26), 3150-3174.

Weingartner, T., Dobbins, E., Danielson, S., Winsor, P., Potter, R., & Statscewich, H. (2013). Hydrographic variability over the northeastern Chukchi Sea shelf in summer-fall 2008–2010. *Continental Shelf Research*, *67*, 5-22.

Weingartner, T. J., Potter, R. A., Stoudt, C. A., Dobbins, E. L., Statscewich, H., Winsor, P. R., ... & Borg, K. (2017). Transport and thermohaline variability in Barrow Canyon on the Northeastern Chukchi Sea Shelf. *Journal of Geophysical Research: Oceans*, 122(5), 3565-3585.

Winsor, P., & Chapman, D. C. (2004). Pathways of Pacific water across the Chukchi Sea: A numerical model study. *Journal of Geophysical Research: Oceans*, *109*(C3).

Woodgate, R. A., Aagaard, K., & Weingartner, T. J. (2005). Monthly temperature, salinity, and transport variability of the Bering Strait through flow. *Geophysical Research Letters*, 32(4).

Woodgate, R. A., Weingartner, T., & Lindsay, R. (2010). The 2007 Bering Strait oceanic heat flux and anomalous Arctic sea ice retreat. *Geophysical Research Letters*, *37*(1).

Woodgate, R. A., Weingartner, T. J., & Lindsay, R. (2012). Observed increases in Bering Strait oceanic fluxes from the Pacific to the Arctic from 2001 to 2011 and their impacts on the Arctic Ocean water column. *Geophysical Research Letters*, *39*(24).

Woodgate, R. A. (2018). Increases in the Pacific inflow to the Arctic from 1990 to 2015, and insights into seasonal trends and driving mechanisms from year-round Bering Strait mooring data. *Progress in Oceanography*, 160, 124-154.

Zhang, W. G., & Gawarkiewicz, G. G. (2015). Dynamics of the direct intrusion of Gulf Stream ring water onto the Mid-Atlantic Bight shelf. *Geophysical Research Letters*, *42*(18), 7687-7695.

Chapter 3

Impacts of Short-Term Wind Events on Chukchi Hydrography and Sea Ice Retreat

Submitted to *Deep Sea Research Part II: Topical Studies in Oceanography,* July 2019

Kofan Lu[1], corresponding author, klu3@alaska.edu

Seth Danielson[1] (sldanielson@alaska.edu), University of Alaska Fairbanks

Thomas Weingartner[1] (tjweingartner@alaska.edu), University of Alaska Fairbanks

[1]College of Fisheries and Ocean Science, University of Alaska Fairbanks, Fairbanks, AK, USA, 99775-7220

Abstract

We seek a better understanding of the summer ice retreat over the Chukchi shelf by investigating mechanisms through which wind forcing mediates changes in sea ice cover, water column hydrography, and their inter-related evolution in time, in the presence of a warm background inflow. The problem is addressed with an idealized depiction of the Chukchi Sea's Central Channel within the Regional Ocean Modeling System (ROMS) framework, forced with inflow from the south, surface heat fluxes, and surface wind stresses of varied magnitudes and directions. Due to strong atmosphere-ice coupling, direct wind-forced advection of the ice edge emerges as the over-riding factor that triggers numerous consequences. These include Ekman surface convergences and divergences, which decrease and increase vertical transport, respectively, and corresponding alterations of the sea surface height. Somewhat surprisingly, we find no significant wind control of the cross-frontal eddy transport, due to counter balances between the frontal density gradient and the pycnocline depth. We propose a conceptual model for understanding the net impact of the wind influence on the Chukchi shelf ice retreat and hydrographic structure. Advection of ice away from the inflow reduces the ice melt rate and increases the salinity of the meltwater plume. Advection of ice toward the inflow increases the ice melt rate and decreases the meltwater plume salinity. The identified mechanisms represent steps toward a more complete understanding of the summer conditions in the Chukchi Sea and will help future investigations of seasonally ice-covered shelf ecosystems.

1. Introduction

The seasonal ice distribution in the Chukchi Sea is established by its thermodynamic responses to oceanic and atmospheric heat fluxes (Serreze et al., 2016; Onarheim et al., 2018), advection by ocean currents (Paquette and Bourke, 1981), and direct wind forcing (Stabeno et al., 2018; Okkonen et al., 2018). Observations show an annual mean of about 8 TW (Woodgate, 2018), sufficient heat to melt about 1.4 meters of ice across the entire Chukchi Sea. Model results suggest that in the absence of wind the oceanic heat flux directed by the underlying bathymetry dominates the pack ice retreat, with about one third of the oceanic contribution due to baroclinic instabilities spawned along the ice edge (Lu et al., in review). Our focus in this paper is on regional wind field modifications to the no-wind interactions between the Bering Strait inflow, the eddy field, and the ablating summer Chukchi ice edge.

The marginal ice zone (MIZ) is the ice cover transition between pack ice and open water, often defined as the region covering partial ice concentrations of 15% to 80% (Stroeve et al., 2016). Lu et al. (in review) suggest an oceanic analog to the MIZ, defining the shelf water transition zone (SWTZ) and the melt water transition zone (MWTZ) as dynamically distinct regions whose energetics govern the rate of heat flux to the ice edge. The MWTZ and SWTZ are structural fronts separating water types of three distinct classes found on the Chukchi shelf in summer: buoyant, fresh and cold ice melt water (MW); dense, cold and salty winter water (WW), formed the prior winter through cooling and salinization due to brine rejection from freezing ice; and warm, intermediate density shelf water (SW), comprised of the Bering Strait inflow that is additionally heated by the atmosphere as it transits toward the ice edge. Interestingly, the two oceanic transition zones encompass an area that exceeds the smaller dimensions of the MIZ, hinting that the MIZ is a consequence of the heat balances between the oceanic and atmospheric

fluxes.

The Bering Strait inflow induces intrapycnocline eddies because of baroclinic instabilities that develop at the fronts between the MW and SW (Lu et al., 2015). These eddies promote lateral heat transport of the Bering Strait inflow toward the ice pack, and enhance vertical mixing, thereby helping to break the stratification between the surface melt water layer and the dense winter water. Eddy-induced vertical mixing is thought to be important for delivering stored subsurface heat to the sea ice. Both the lateral and vertical heat transports are believed to be altered by wind forcing and impact sea ice retreat on the Chukchi Shelf (Lu et al., 2015).

There are several pathways for wind to change lateral and vertical heat transport. Winds can enhance intrapycnocline eddy formation by destabilizing the surface buoyancy flux and structure, thereby leading to gravitational instability (Thomas, 2008). In fresh water frontal zones, the wind-driven redistributions of surface melt water are able to change the frontal density gradient and affect eddy energy (Spall and Thomas, 2016). The Ekman transport induced by strong winds will impact the onset of the seasonal ice retreat by advections of inflow (Woodgate et al., 2005; Stabeno et al., 2018; Okkonen et al., 2018) or in opposite by reversing the transport by strong northerly winds for few days to weeks (Coachman and Aagaard, 1981; Woodgate et al., 2005, Danielson et al., 2014). Ekman transport also generates upwellings and downwellings that vary vertical heat transports from warm subsurface layers to the ice (Carmack and Chapman, 2003; Watanabe and Ogi, 2013). In addition, wind forces can act directly on ice (Serreze et al., 2016) and cause "ice edge loitering" (Steele and Ermold, 2015), a behavior of slowed, stalled or even backward ice extent cover. Observations show that correlation between wind and currents in the central Chukchi is 0.5-0.6 (Woodgate et al., 2005; Stabeno et al., 2018) and 50% of the variance of the change in Summer Arctic sea ice extent is counted on wind forcing (Ogi et al., 2010).

This study applies a set of short-term wind forcings to a high-resolution ROMS model (Lu et al., 2015) with an idealized domain that represents the Chukchi Sea's Central Channel region (Lu et al., in review). The model is initialized with late-spring ice, stratification, and density fields. The incorporated wind forcing will vary in both speed and direction for analyzing the role of wind stress on ice retreat and the influences on the importance of instability-induced eddy fluxes.

The paper is organized as follows. Section 2 describes the model configuration, design of wind forcing set and introducing the integration domains. Model results are analyzed with respect to 1) displacements of ice edge and fronts under the effects of winds in Section 3.1; 2) variations of water masses and mixed layer depths in Section 3.2; 3) frontal instabilities and contributions of eddy and vertical fluxes promoted by wind forcing in Section 3.3; and 4) surface height variations under wind impact and the related lateral transport in Section 3.4; to evaluate the role of wind to hydrography and ice retreat as summary in Section 3.5. Section 4 reports observations that support the mechanisms established by model results. Further discussion is provided in Section 5.

2. Background and Methodology

In this section we describe the model setup and integration schemes for systematically testing the impact of winds on the ice meltback. We also introduce ancillary remotely sensed and in situ observational data used to help support the modeling results: satellite-derived ice concentrations and hydrographic survey data.

2.1 The model

We extend the high-resolution model using the Regional Ocean Modeling System (ROMS) from Lu et al. (2015) and Lu et al. (in review), which describe an idealized model with simplified

bathymetry of the Central Channel region of the Chukchi Sea. It is forced with a Bering Strait inflow from the southern boundary and is integrated for analysis over 3 months from June to August following a 1-month spin-up. Atmospheric forcing is imposed using typical values of solar radiation, air temperature and humidity taken from the NCEP-NCAR Reanalysis (Mesinger et al., 2006). The vertical turbulent viscosity and mixing coefficients use the Mellor-Yamada level 2.5 turbulence closure scheme with background coefficients 10^{-6} (Mellor and Yamada,1982; Galperin et al., 1988; Kantha and Clayson, 1994; Durski et al., 2004). Bottom drag is quadratic with coefficient 0.003, interface drag coefficients of air-sea, air-ice, ice-sea are 1.15×10^{-3}, 3×10^{-3} and 7.5×10^{-3}, respectively as described in Hedstrom (2018).

Results from July 1st of the model integrated without wind forcing from Lu et al. (in review) provide initial conditions for the wind experiments described herein, which begin with application of constant winds for 10 days. The initial condition (Figure 1) is associated with Bering Strait inflow discharge of 0.8 Sv, potential temperature is 6°C and salinity is 30. The ice edge is advected northward and melted by the Bering Strait inflow, leaving ~1.5×10^{4} km^2 open water area. The model domain can be separated into four zones of interest from north to south (Figure 1) according to the ice distribution and hydrography: the Pack Ice Zone (PIZ) with near complete ice cover; the MWTZ and the SWTZ (described above), and the open water Ice Free Zone (IFZ). Ice with 100% ice concentration and ~1.2 m thickness in the PIZ is primarily melted by solar heat flux. Very fresh (salinity < 28) MW in the MWTZ surrounds the ice edge due to rapid ablation in this region. This fresh MW has a layer thickness of ~10-15 m, which varies upon interacting with the SW in the SWTZ due to baroclinic instabilities. The SWTZ contains weakly-stratified SW, which contributes ~5-10 TW heat to the ice melt (Lu et al., in review).

For the model integration tests under wind forcing, we start with applying constant surface

stresses over 10 days with 45 increments of degree through 8 compass directions. Each direction is tested with four wind speeds set to 2, 4, 6 and 8 ms^{-1} for a systematic analysis for understanding the role of winds on altering the nature and rate of the ice melt.

Oscillating winds are also tested in our model to understand the hydrographic responses to continuous variations of wind direction. Two oscillating model tests are compared with the model test without wind forces. First, the oscillating wind is given hourly as a sine function between southeasterly and northwesterly directions with a peak magnitude of $8\sqrt{2}$ ms^{-1} for 20 days. Another test has the same wind conditions for the first 10 days and then the wind stress ceases at the 11^{th} day. Results of ice retreat and hydrographic features are discussed in Section 3.5.

2.2 Ice concentration data

In section 4, observations that support the mechanisms linked between ice distribution and wind forces, using the ice concentration dataset from the National Snow and Ice Data Center (NSIDC) employing the NASA team algorithm on a polar stereographic projection at a grid cell size of 25×25 km (Cavalieri et al., 1996). In conjunction with the sea ice data, wind data are from the North American Regional Reanalysis (Mesinger et al., 2006). These are 3 hourly data from 10 m elevation and spatially averaged over the eastern Chukchi shelf region bounded by 66-72°N and 171-160°W.

3. Model Results

3.1 Ice Retreat

We begin with model integrations that with wind magnitudes of 8 ms^{-1} and the eight directions shown in Figure 2 (a-d & f-i).

The integrations reveal impacts of the wind direction on the ice retreat (Figure 2), direction of ice motion, open water area and surface salinity. We find that the ice retreat is most intensified under the effects of southeasterly (Figure 2i) winds due to the strong northward transport that result from the combined effects of the wind and the northward flow from Bering Strait; this leads to largest open water area of ~12×10^4 km^2 when wind velocity is 8 ms^{-1}. The Bering Strait inflow and unstratified SW front are only modestly vulnerable to wind modifications. The drag coefficient that couples the wind and the sea surface is 1.15×10^{-3}, which is less than half of the drag coefficient between wind and ice ($C_D = 3\times10^{-3}$) and much smaller than the drag coefficient between ice and the sea surface ($C_D = 7.5\times10^{-3}$). Hence, the reaction of the SW to short-term winds is not as remarkable as the movements of ice edges. The shifting patterns of the ice edge dragged by winds from different directions are consistent among varied magnitudes of moderate winds (> 4 ms^{-1}) (Figure 2e), whereby the ice edge motion undergoes an Ekman type response that is modified by the background flow field.

3.2 Water Mass Characteristics and Stratification

In this section, we discuss the variations of water mass characteristics and stratification resulting from dynamics of the ice motion and vertical mixing by winds. We focus especially on salinity because it dominates the determination of water mass density and stratification.

Fresh melt water (MW, S<28) is sourced from rapid melt along the ice edge; therefore, the melt water volume is determined by ice contact with the SW front as described by Lu et al. (in

review) but modified by an additional contribution (or removal) of ice to the frontal zone. For example, in the case of southeasterly wind (Figure 2i) the ice edge shifts away from the SW front due to strong northward surface advection. The ice edge contact with the SW front diminishes because the oceanic front is less vulnerable to wind forces than the ice edge itself. In this condition, ice retreat is primarily caused by wind stress rather than melting by the warm Bering Strait inflow.

At the start of the wind forcing, the sea surface near the ice edge is covered by cool MW. Over the course of the 10-day wind event, the spatially averaged ice albedo decreases from 0.65 to 0.51, leading to a SST increase from -1.44°C to -1.26°C around the ice edge (i.e. MWTZ), indicating a modest influence of MW heating. The fast northward ice advection results in less volume and higher salinity of MW (Figure 3e and 3i). In contrast, strong southward advection of ice under northwesterly winds (Figure 2a) increases the MW volume (Figure 3e) due to rapid melt because the ice edge strongly contacts the SW front. This process makes MW even fresher, as shown by the surface salinity in Figure 3a. Figure 3 shows MW salinity ranges from 24 to 28 and that it mixes with both winter water (WW, S~33) and SW (S~30).

Shorter distances between the ice edge and SW front also leads to more mixing between MW and SW, and MW at the ice edge will be relatively fresh (S~26). Conversely, longer distances from the ice edge to the SW front leads to more mixing of SW with WW and further increases salinity of the relatively salty MW (S~28). In the Arctic Ocean, density is dominated by salinity effects and will impact eddy transport generated by baroclinic instabilities on fronts.

3.3 Eddy and vertical heat transport

In this section we assess lateral and vertical heat transport variations relative to the various wind forcing described above.

In the SWTZ, upward fluxes are enhanced for wind directions (blowing from) between 22.5° to 202.5° by Ekman divergence, due to the ice-water drag coefficient being greater than the air-water drag coefficient. In contrast, the winds directions, which are between 0° to 22.5° and 202.5° to 360°, lead to surface Ekman convergence and increased downward fluxes shown as Figure 4a. Similar variations occur in the BSW layer (Figure 4c) of the MWTZ. Figure 4c shows that the vertical heat flux in the BSW layer of the MWTZ is always upward when intruding between the WW and MW layers, but it significantly increases under divergence conditions and decreases under convergence. In the MW layer of the MWTZ shown by Figure 4b, upward fluxes increase with increasing wind speeds, influence of wind directions is relatively small.

Baroclinic instabilities on fronts induce eddy velocities $u_{eddy} = \frac{g}{\rho_0 f}\Delta h \Delta \rho$ that can be evaluated by the difference of the bulk frontal density ($\Delta\rho$) and the difference of frontal layer thickness (Δh) (Haine and Marshall, 1998). Under the influence of wind directions between 22.5° to 202.5°, surface Ekman divergence decreases the MW layer thickness and increases the height difference ($\Delta h \uparrow$) between the MW layer and the unstratified BSW layer in the frontal zone. Meanwhile, less mixing between MW and BSW results in somewhat saltier MW, leading to a smaller density difference ($\Delta\rho \downarrow$) between the MW layer and unstratified BSW layer in the frontal zones. The two major factors, $\Delta\rho$ and Δh, cancel each other (i.e. negative correlations) for each wind forcing magnitude (seen within the dashed ovals of Figure 5a). Overall, eddy heat transport to the ice edge is ~0.6 TW under all wind speeds and directions (Figure 4b and 4c) except for the model tests forced by strong easterly (light orange) and northeasterly (yellow) winds. Eddy heat transport under the influence of strong (8 m/s) northeasterly (yellow) and easterly (light orange) winds enhance the strong mean flows from Bering Strait, and are linked to the lower sea surface height associated with surface divergences discussed in next section.

Figures 5b and 5c show that the eddy heat transport is positively correlated to the mean flow heat transport in both SWTZ and MWTZ.

3.4 Sea Surface Height

The SW and its associated front only weakly respond to wind forcing; enhanced mean flow transport is found only when sea surface heights are lower in the vicinity of the ice edge due to surface divergences driven by strong wind (>8 ms^{-1}, Figure 6c and 6f). The notably larger eddy heat transports shown in Figure 4b and 4c are believed to be a consequence of these relatively strong background flows. In contrast, sea surface height rises significantly when the surface Ekman transport and ice drift are directed toward the inflow direction. In this case, the pressure gradient force impedes the mean flow and lead to a weaker frontal velocity (Figure 6a, 6d, 6g and 6h).

Overall, surface Ekman divergence driven by winds with directions between 22.5° to 202.5° decrease the sea surface height in the vicinity of the ice edge and increase the mean flow transport of the SW front, but this mechanism only becomes significant when the wind magnitude exceeds 8 ms^{-1}.

3.5 Model Results Summary

Two important points follow from the model integrations described above: 1) Wind direction has a significant influence on ice retreat because of the relatively large air-ice drag coefficient. 2) Surface salinity and stratification is a function of the distance between ice edge and SW front. For an ice edge closer to the SW front, the surface layer MW becomes fresher and deeper due to rapid ice melt and mixing with BSW. However, winds also increase vertical mixing (Figure 4b) in the MW layer (i.e. mixing between MW and the underlying WW), which tends to weaken the relationship between the wind-driven ice advection and the surface salinity.

To strengthen and provide further context to the summary points, we conduct model integrations (described in Section 2.1) with oscillating winds, shown as Figure 7a. The corresponding open water area (Figure 7b) increases when the surface Ekman transport is northward and decreases for southward transport. The open water area is only slightly smaller than for the model case without wind (i.e. ice is primarily melted by the Bering Strait inflow) due to the wind-driven southward ice advection after the last 5 days of the applied wind.

Sea surface height (Figure 7c), driven by Ekman divergence and convergence, is lowest under the influence of the strongest southeasterly wind and highest under the strongest northwesterly wind, respectively, due to the difference of drag forces on ice and sea surface. Note that once the winds stop at day 11, the sea surface height recovers to its unforced regime within about three days (dashed line in Figure 7c).

The bulk salinity of MW along the ice edge increases with strengthening southeasterly winds during the first 2.5 days then remains nearly constant, even after the wind forces change to the opposite direction, because the wind continues to enhance vertical mixing between MW and WW. If winds stop at day 11, it takes ~2 days to form a new and fresh MW plume after the ice edge re-contacts the SW front (dotted line). This newly formed MW has lower salinity than that of MW without any wind forcing (dashed line) because it has not yet mixed with BSW.

The eddy transport, which correlates with vertical transport in the absence of wind forcing, has no remarkable variation under wind effects because of the counterbalance between layer thickness and density difference on the fronts. Mechanisms describing the role of wind to ice retreat and hydrography in the vicinity of the ice edge as discussed here can be summarized as the schematic in Figure 8.

4. In situ observations

In this section we utilize real-world observations from satellites and from shipboard hydrography to provide some evidence that supports the model results.

We begin with daily satellite measures of sea ice concentration, comparing daily variations of ice concentration (averaged over the eastern Chukchi Sea) to daily mean wind vectors in July from 1979 to 2017 (Figure 9). Our metric for the response of the sea ice to wind forcing is the day-to-day change in ice concentration.

For wind directions between 22.5° to 202.5° (to the right of the black thick line of Figure 9), the ice concentration often decreases (cold colors) in the following day, indicating increased open water areas due to northward ice advection. On the left half of wind compass, increasing daily ice concentrations are shown with warm colors, indicating shrinkage of the open water area when ice edges were advected southward. These color patterns occur from May to August during the ice melt-back season, are consistent with surface Ekman dynamics, support our model results, and are consistent with the relationship between winds and the daily ice edge displacement shown as Figure 13 from Steele and Ermold (2015).

The shelf hydrography is also impacted by winds. We lack large numbers of hydrographic transects that extend from IFZ to the PIZ over the Chukchi shelf. However, there do exist a few transects that can be assessed as discrete case studies for consistency with the above model results.

The model suggests that very fresh melt water (salinity<28) is present around the ice edge only when winds are persistently weak or dominated by northerly components. The hydrographic cross-section along the Central Channel in 2008 (Figure 10) shows that fresh MW occurred near the ice edge where the ice concentration notably decreased. Substantial northerly components of

daily winds are found throughout 2008 summer (Weingartner et al., 2013; Linders et al., 2017) and are believed to have advected the ice edge close to the warm SW front intermittently, thereby preserving the fresh melt water plume.

In contrast, strong winds with southerly components push ice edge away from Bering Strait inflow, diminishing MW volume and increasing the bulk salinity. Once open water forms, winds enhance vertical mixing between MW and beneath BSW/WW leading to an increasing bulk salinity of MW regardless of wind direction, but possibly enhanced for the case of winds from over the IFZ (southerly winds) because of a larger open water fetch. Compared to the 2008 hydrographic properties (Figure 10), MW was nearly absent in 2012 (note lack of cold fresh water relative to 2008) and suggests more mixing between MW and BSW/WW (Figure 11). This finding is consistent with the model results, because summer 2012 winds were from the southeast on average (Weingartner et al., 2017).

Although we lack sufficient data for an exhaustive comparison of the model results to the real Chukchi shelf, the above case studies provide snapshots that are at least consistent with the modeling and the proposed conceptual functioning of the atmosphere-ice-ocean system. This includes both the net displacement of the ice edge under various wind directions and the associated hydrographic response. We particularly highlight the finding that the MW plume salinity can be directly tied to the relative motion between the wind-forced sea ice and the warm SW that that lies south of the ice edge.

5. Discussion

Our model deduces important roles of the wind on ice retreat and hydrographic variations. The relationship between ice edge displacement and wind direction is found to be consistent with

well-known Ekman dynamics and we are able to provide examples of consistent observations. Our analyses show that the relative direction of the wind to the ice edge may be the controlling factor in regulating the salinity and mixed layer depth thickness of the MW in the SWTZ and the MWTZ. The importance of wind drag forces on ice can be applied widely on any ice-covered region in the Arctic Ocean having ice in free drift. Such investigations may require more attention with increasing seasonality of ice the ice pack and changing wind systems (e.g., Wood et al., 2015).

Variations of surface stratification and the related baroclinic eddy transport under the influence of wind stress are highly dependent on the shelf hydrography prior to the onset of wind. Our model results show that the ice edge can be considered a mobile boundary that fosters surface divergence (upwelling) with wind directions between 22.5° to 202.5° and surface convergence (downwelling) with the other directions, and these are associated with enhanced vertical heat transport. In an ice-covered region, surface convergence increases the ice melt rate for decreasing distances between the warm front and the ice edge, hence the accelerating ice melt freshens the MW plume along the ice edge. Once ice melts and open water forms, enhanced vertical mixing from the underlying BSW or WW will increase the MW salinity. Interactions between ice, surface MW and subsurface BSW/WW may confound the correlations between observed surface salinity and wind directions that are suggested by the model results. Additional field studies will be necessary to fully validate the mechanisms proposed by model results.

In addition to stratification, eddy transport is highly correlated to the mean flow transport from Bering Strait (Lu et al., in review), which in turn is determined by the Pacific-Arctic pressure head and both remote and local winds (Woodgate et al., 2005; Aagard et al., 2006; Danielson et al., 2014). We examined variations of the sea surface height and the mean flow

transport influenced by winds, and find that the change of mean flow transport is only noticeable when the wind speed is larger than 6 ms^{-1}, suggesting that the impact of Bering Strait inflow on ice melt is most responsive to the balance of local wind forcing and the background flow.

Our work has focused on the net displacement of the pack ice edge and the associated hydrographic structure and dynamical responses under the influence of wind forcing. Other studies have more closely examined the nature of ice-edge upwelling (Shuchman et al., 2004; Williams and Carmack, 2008), the relation of between landfast ice and offshore waters (Kasper and Weingartner, 2015) and the relation between hydrographic variations inside versus out of lead systems and polynyas (Rudels, 2015). The Arctic Ocean surface stratification and dynamics are sensitive to ice cover and the ice edge location; in the future, wind effects may be more pronounced because momentum transfer from wind to the ocean is higher when ice covered than when ice free (Chapman and Carmack, 2003).

Similarly, changes in polynya activity due to altered surface atmospheric temperatures or winds may alter the spatial heterogeneity of shelf hydrography, the sea ice, and their effects on the ice edge ecosystem. Divergent surface conditions associated with enhanced polar easterlies (Wood et al., 2013) could reduce ice cover and increase water column illumination, alter the strength of the stratification, and suppresses nutrient exchanges toward the surface due to enhanced downwelling. More observations and coupled biophysical modeling will be necessary to evaluate the effects of vertical wind mixing on biological production in the vicinity of the ice edge.

Acknowledge

This work is funded by North Pacific Research Board (NPRB) project #1743 and supported in part by the high-performance computing and data storage resources operated by the Research Computing Systems Group at the University of Alaska Fairbanks, Geophysical Institute. Dr. Seth Danielson and Dr. Kate Hedstrom were also supported by Bureau of Ocean Energy Management (BOEM) Cooperative Agreement M15AC00011 and National Science Foundation (NSF) grant OCE 1459834.

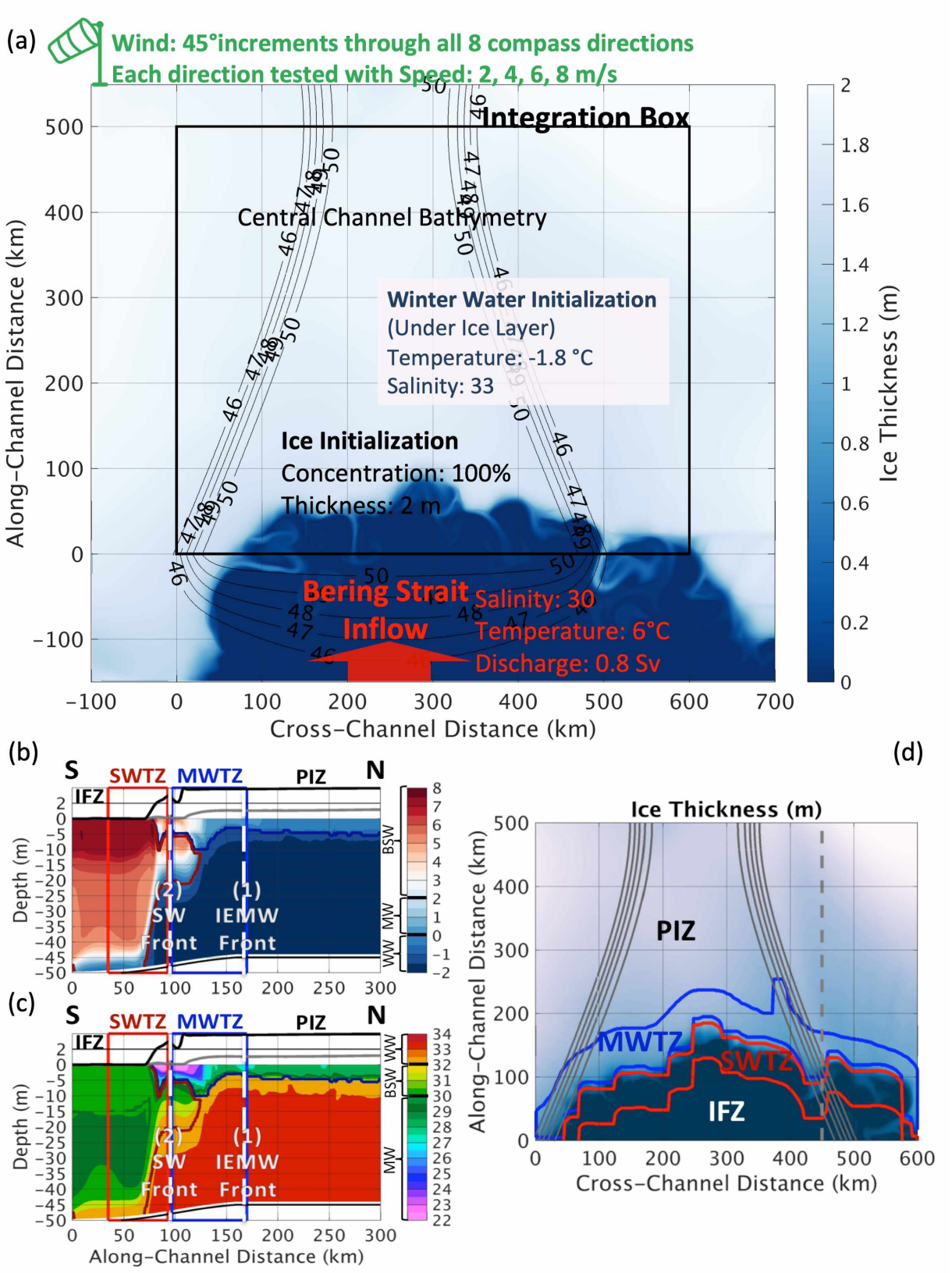

Figure 1. Model configuration (a) with ice thickness plan view from the surface at the beginning

of the analysis integration time (July 1st from model of Lu et al., in review). Temperature (b) and salinity (c) transects across the gray dashed line in (d). Ice and water mass distributions (d) of the four integration domains defined in Lu et al. (in review): Pack Ice Zone (PIZ), Melt Water Transition Zone (MWTZ), Shelf Water Transition Zone (SWTZ) and Ice Free Zone (IFZ), from north to south. Major frontal zones include the Shelf Water (SW) front and the Ice Edge Melt Water (IEMW) front.

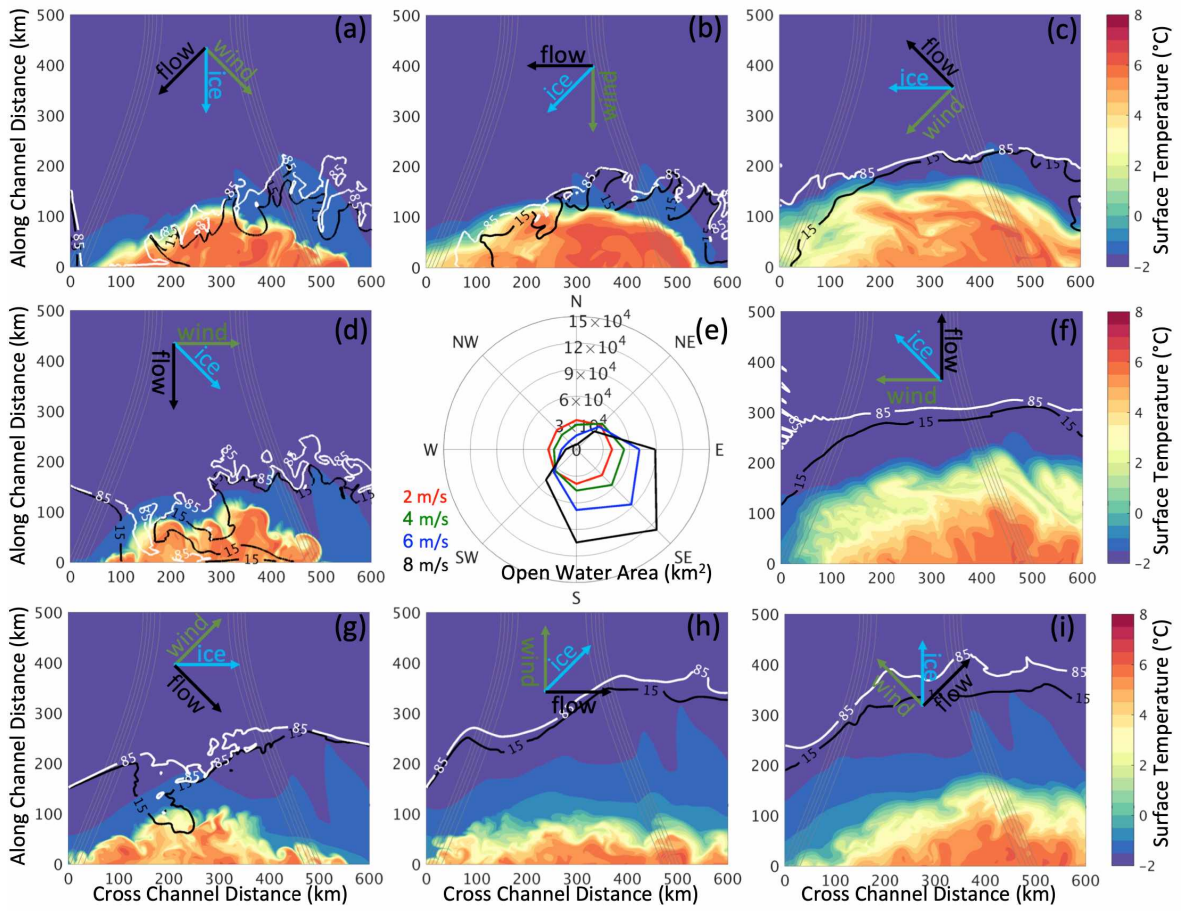

Figure 2. Sea surface temperature (°C) overlapped with 15% and 85% ice concentration contour lines under effects of 8 compass directions winds (green arrows) with speed of 8 ms^{-1}. Panel (e) in the center shows the open water areas in km^2 after 10-days of wind with speeds of 2 (red), 4 (green), 6 (blue) and 8 (black) ms^{-1}.

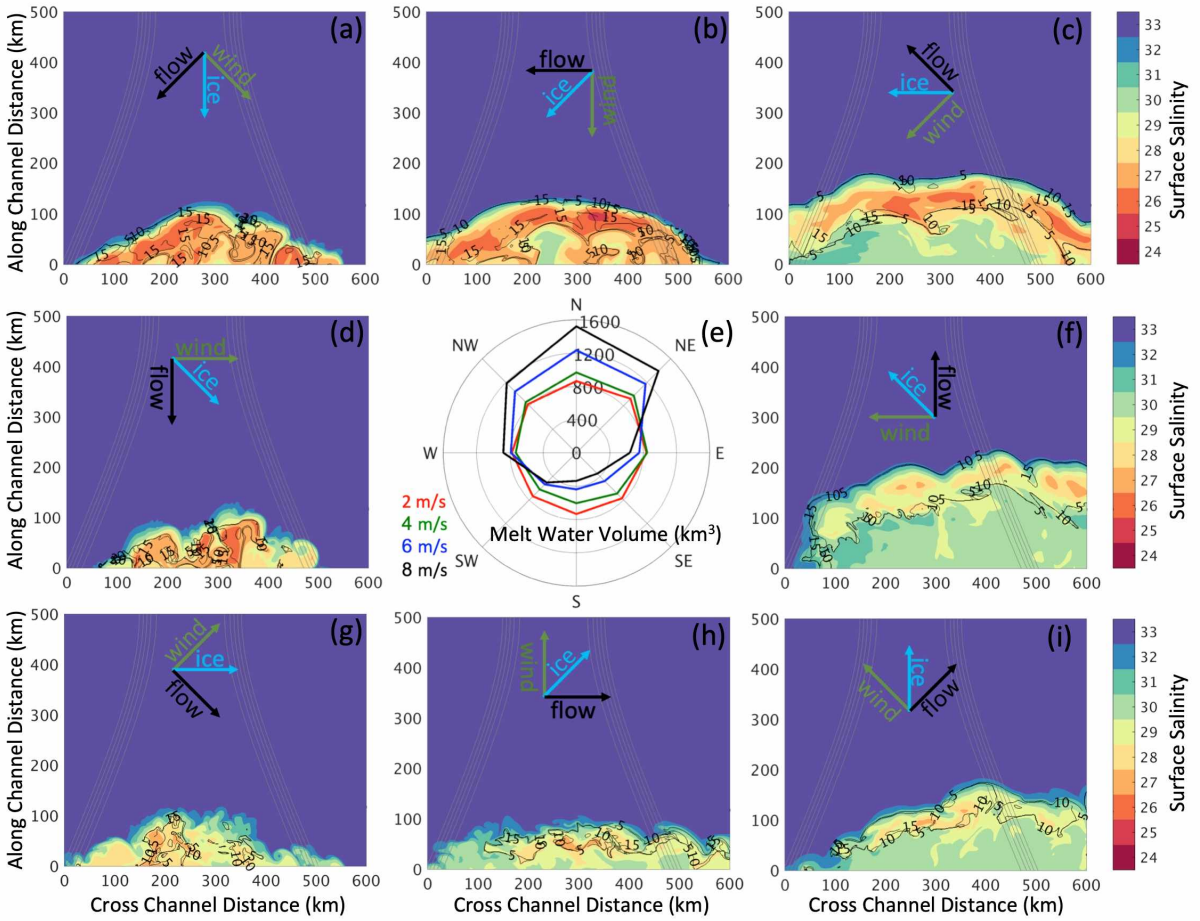

Figure 3. Sea surface salinity overlapped with melt water (MW) layer thickness lines under effects of 8 compass directions winds (green arrows) with speed of 8 ms^{-1}. Panel (e) in center shows melt water volume (km^3) after 10-days wind events having speeds of 2 (red), 4 (green), 6 (blue) and 8 (black) ms^{-1}.

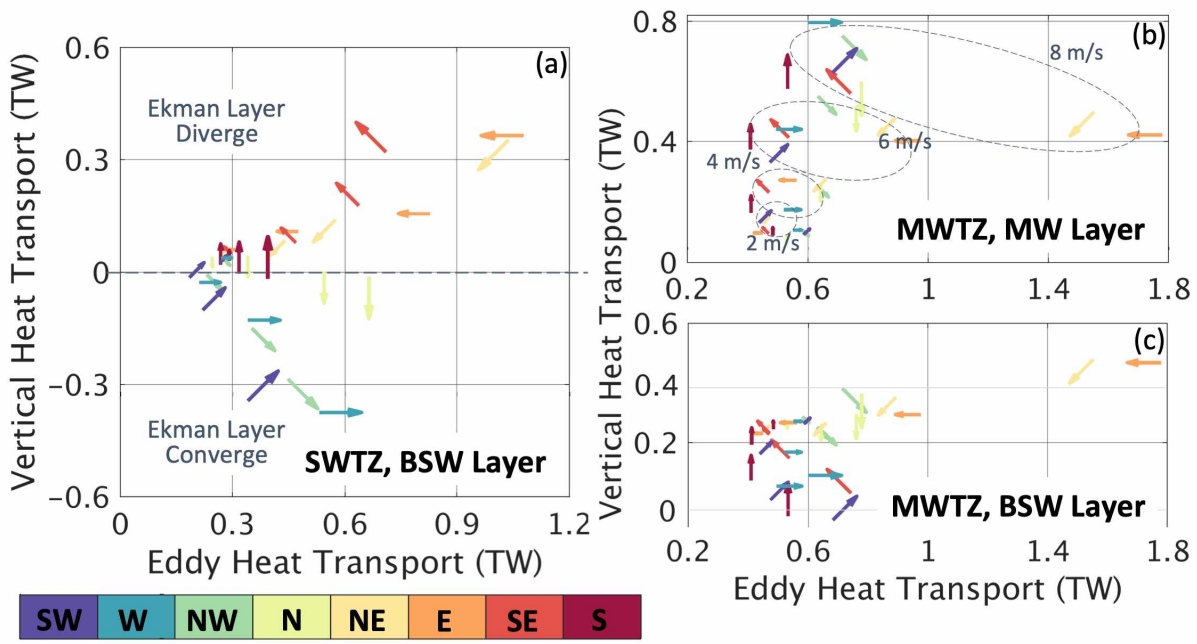

Figure 4. Vertical heat transport and eddy heat transport under the influence of different wind directions and magnitudes in (a) BSW layer in SWTZ, (b) MW layer in MWTZ and (c) BSW Layer in MWTZ. The wind speed is indicated with arrow size and the wind direction is labeled by arrow orientation and the colorbar.

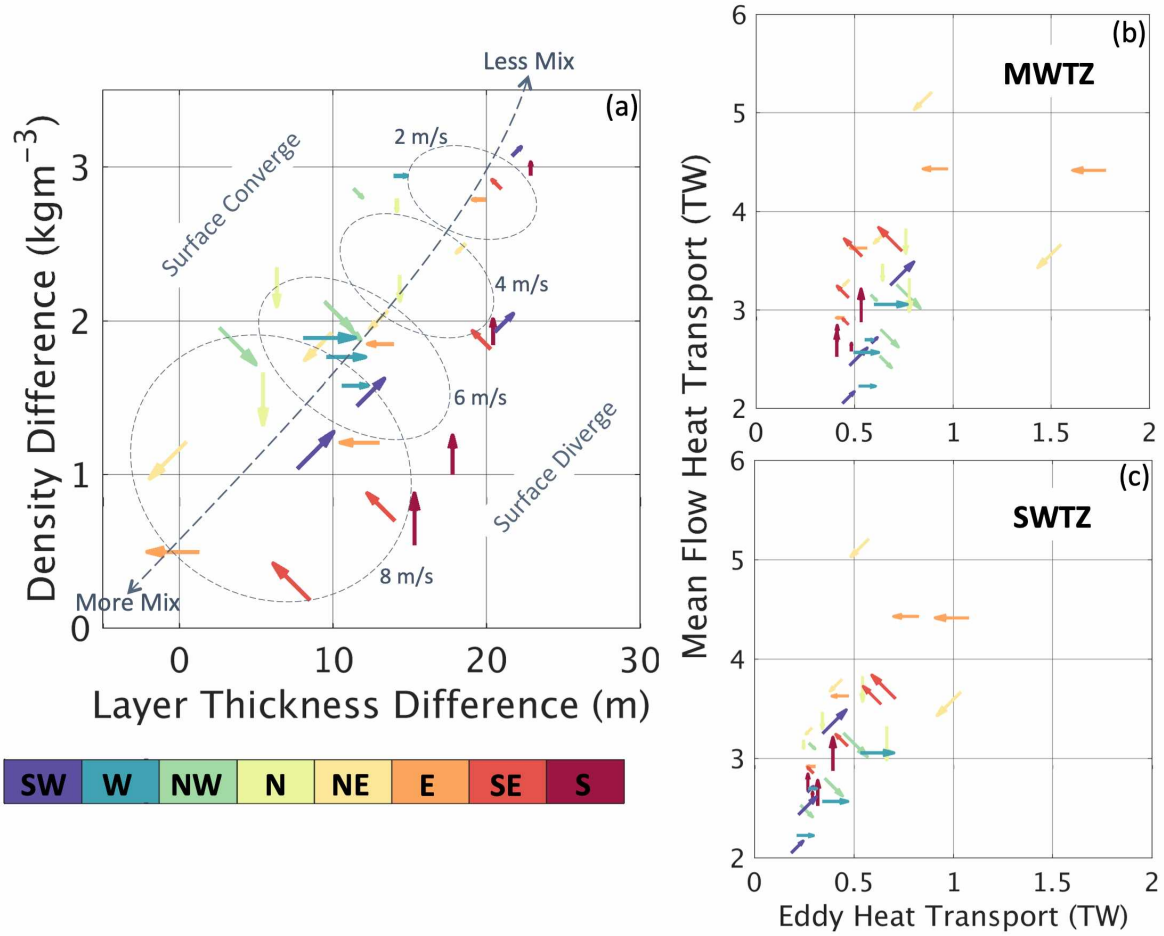

Figure 5. (a) Relation between differences of layer thickness and bulk density across fronts. (b) and (c) shows correlations between mean flow heat transport and eddy heat transport in the MWTZ and SWTZ, respectively. Wind vectors displayed as in Figure 4.

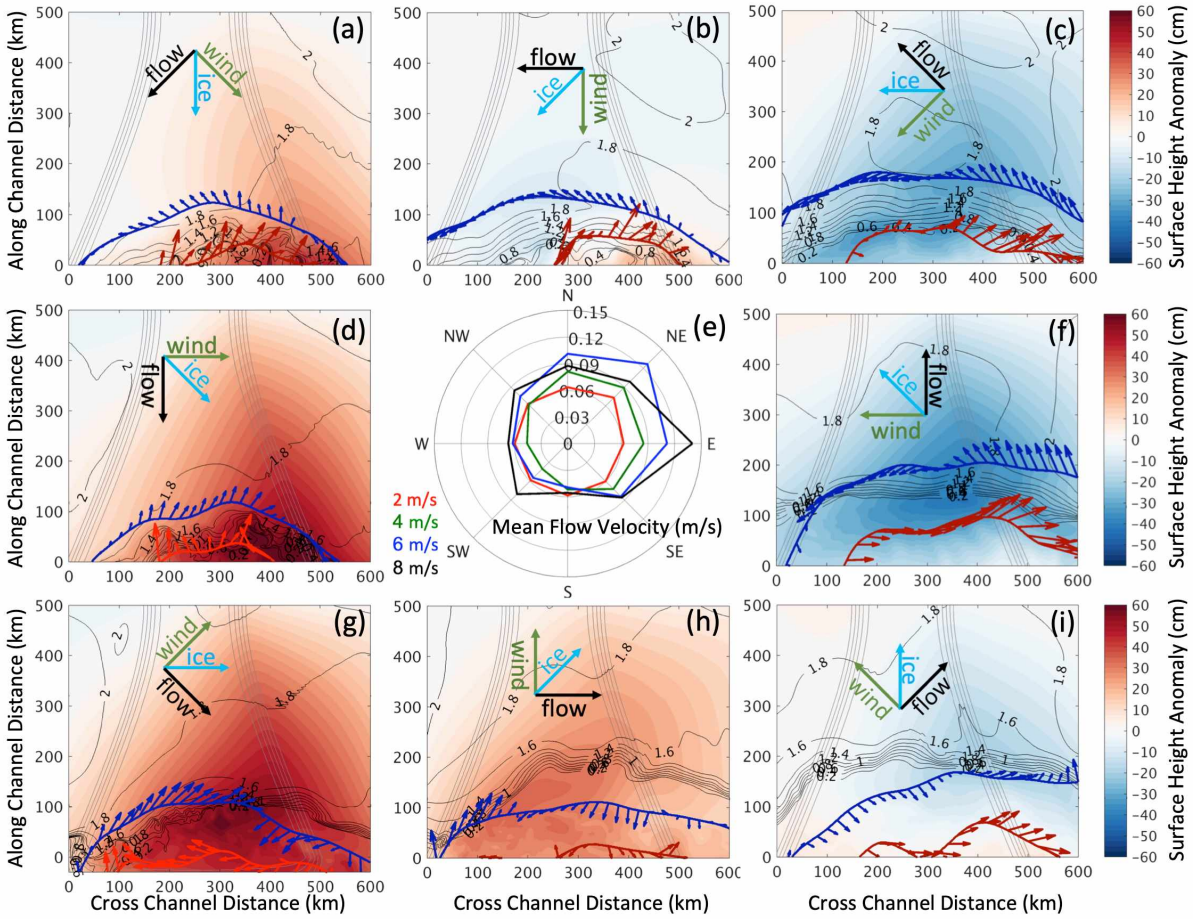

Figure 6. Sea surface height (cm) overlapped with ice thickness (m), SW front velocity (red) and IEMW front velocity (blue) under the effect of 8 compass direction winds (green arrows) having speed of 8 ms^{-1}. Panel (e) in the center is the along-front averaged front velocity (ms^{-1}) after 10-days of wind blowing at 2 (red), 4 (green), 6 (blue) and 8 (black) ms^{-1}.

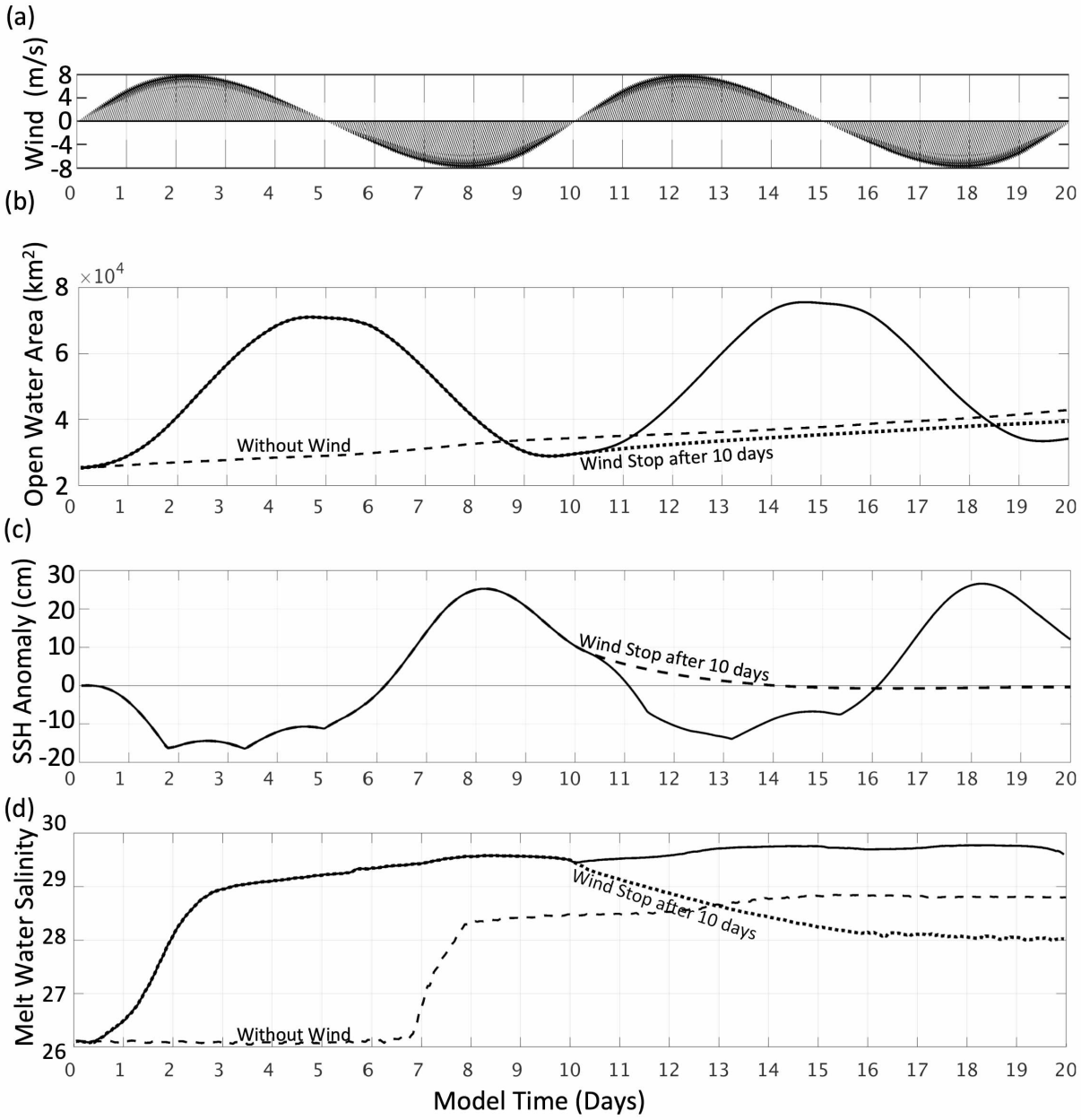

Figure 7. (a) Wind vector time series for the oscillating wind model test. (b) – (d) show variations of the open water area, sea surface height anomaly and bulk salinity of melt water along the ice edge during the 10 day integration.

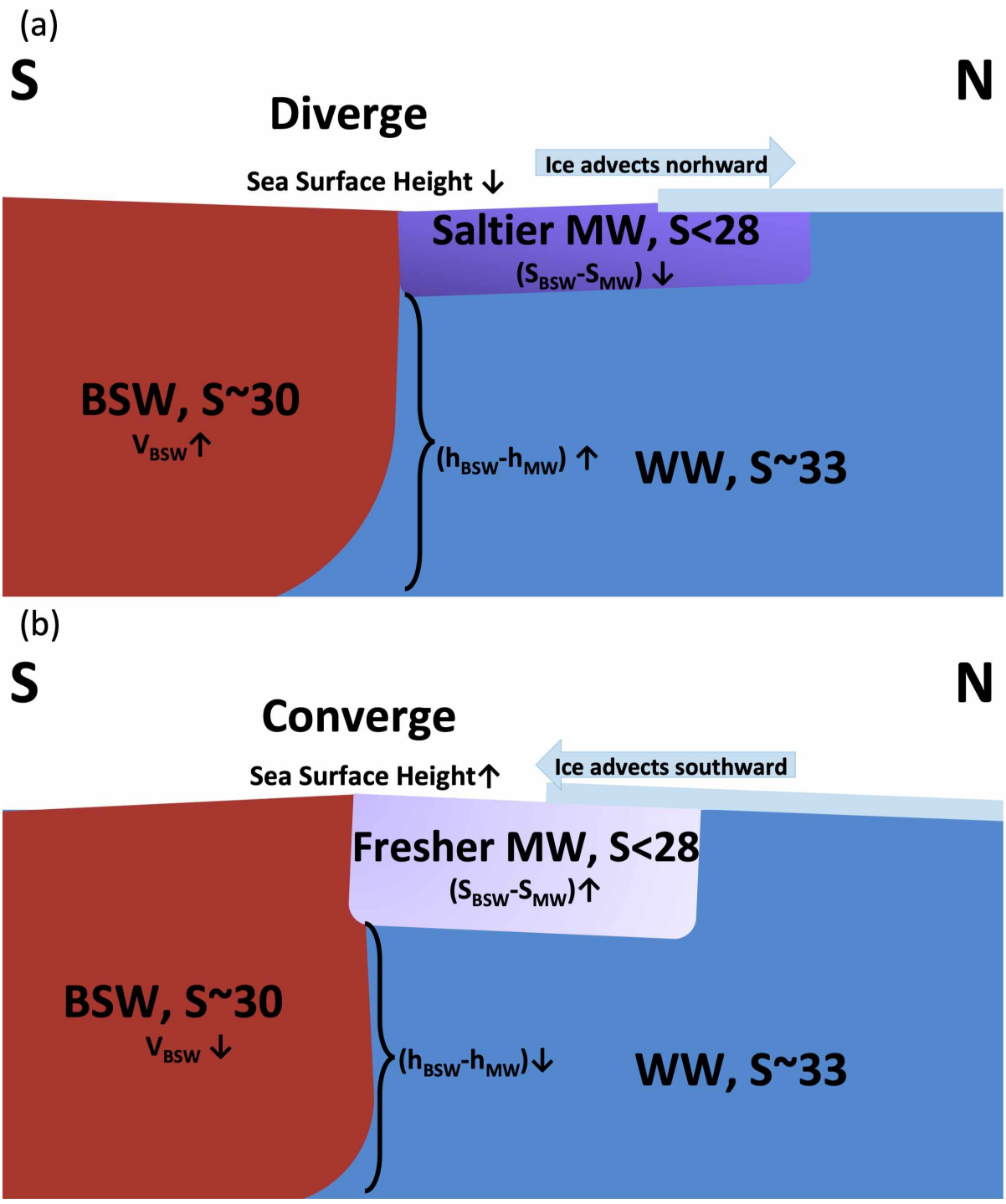

Figure 8. Schematic showing mechanisms of wind effects on ice retreat, stratification, surface dynamics and baroclinic instabilities.

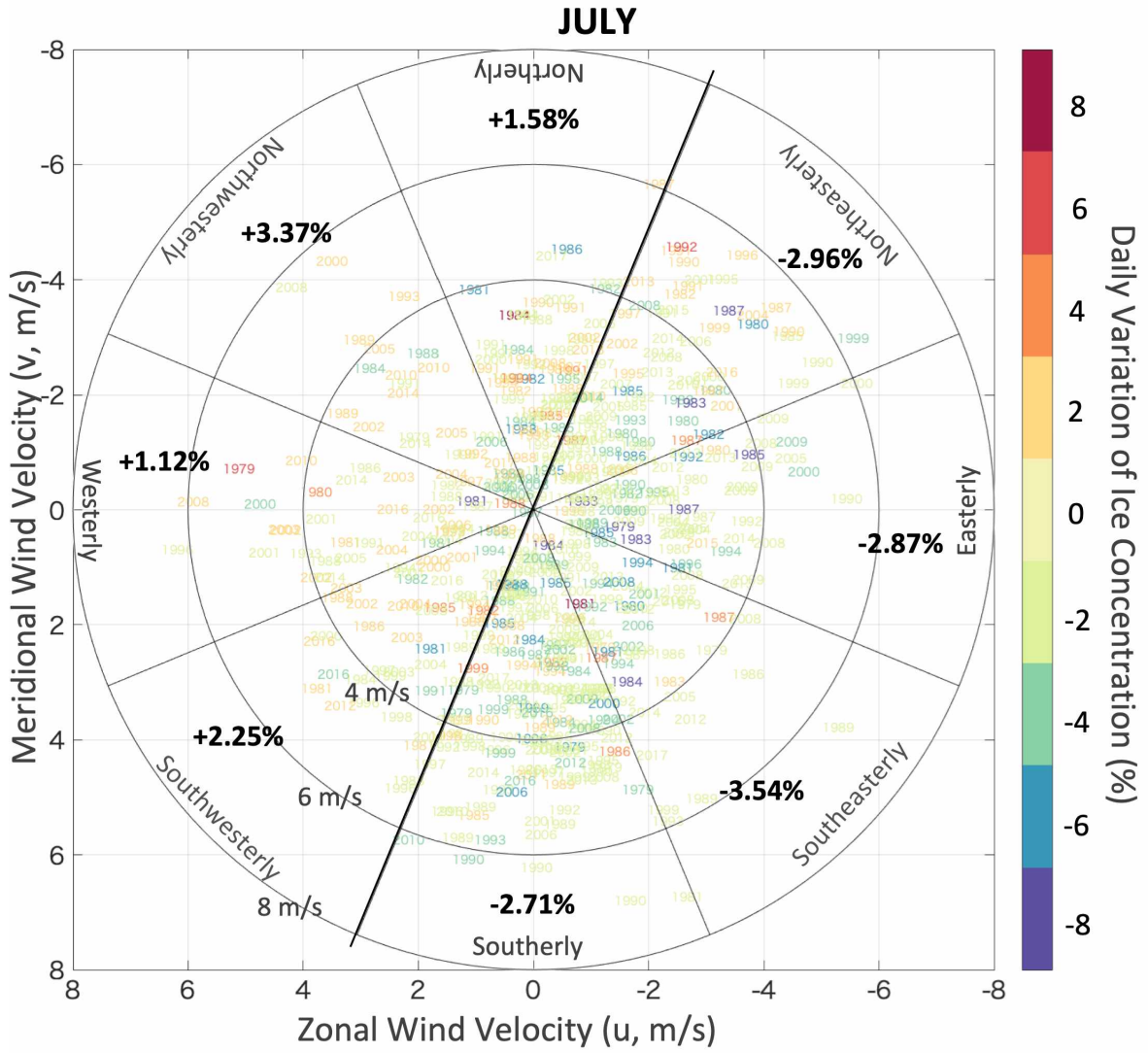

Figure 9. Scatter plot of daily ice concentration variations versus the corresponding daily wind vectors of June over 1979 to 2017.

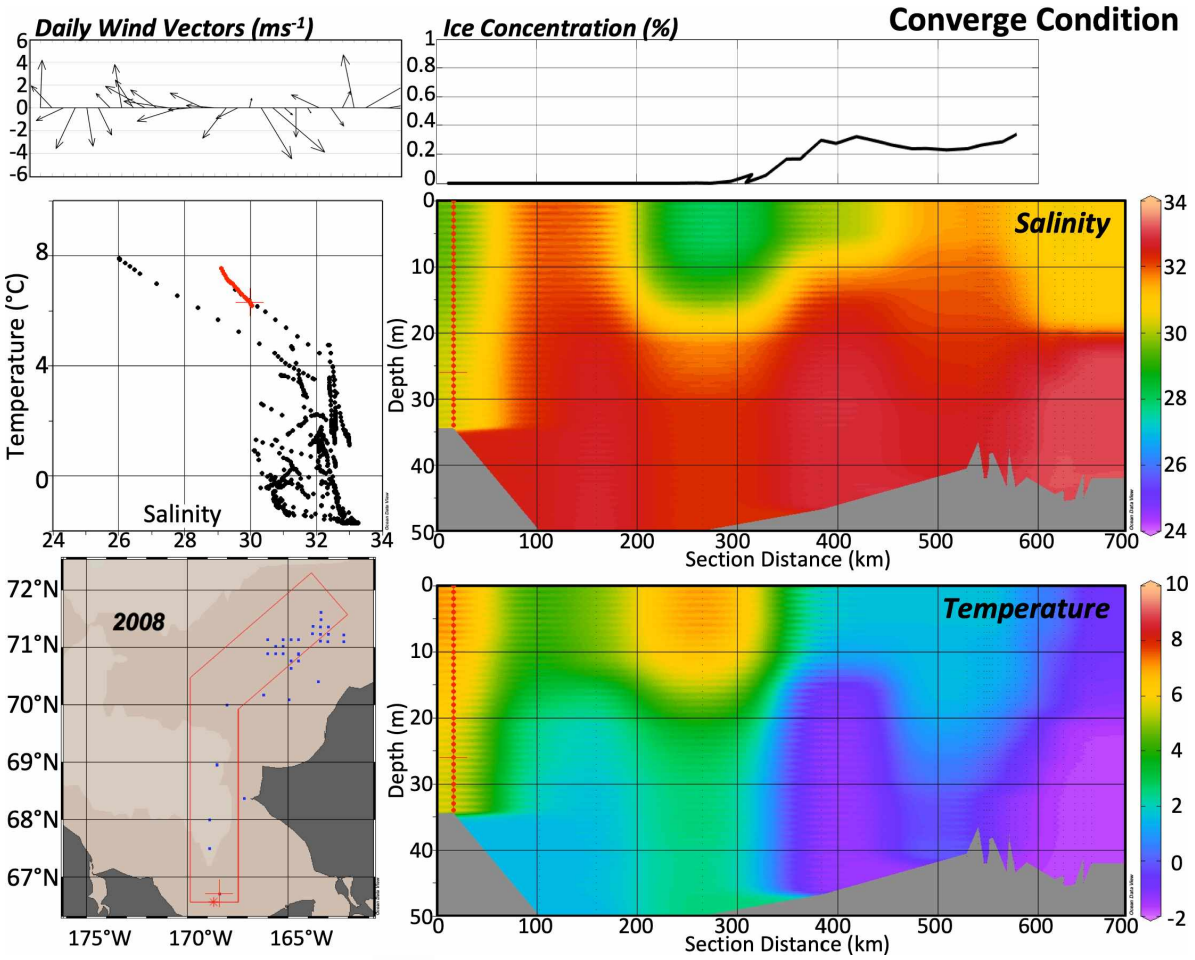

Figure 10. Hydrographic transects (right middle and right lower) and a T-S diagram (left middle) evaluated from CTD casts across the Central Channel within the outlined red polygon (lower left) in the 2008 Summer (June 15 – August 15). The ice concentration (upper right) is the July 2012 average evaluated from the NSIDC NASA team algorithm along 169°W. Daily wind vectors shown in upper-left corner are from the North American Regional Reanalysis for July 2008.

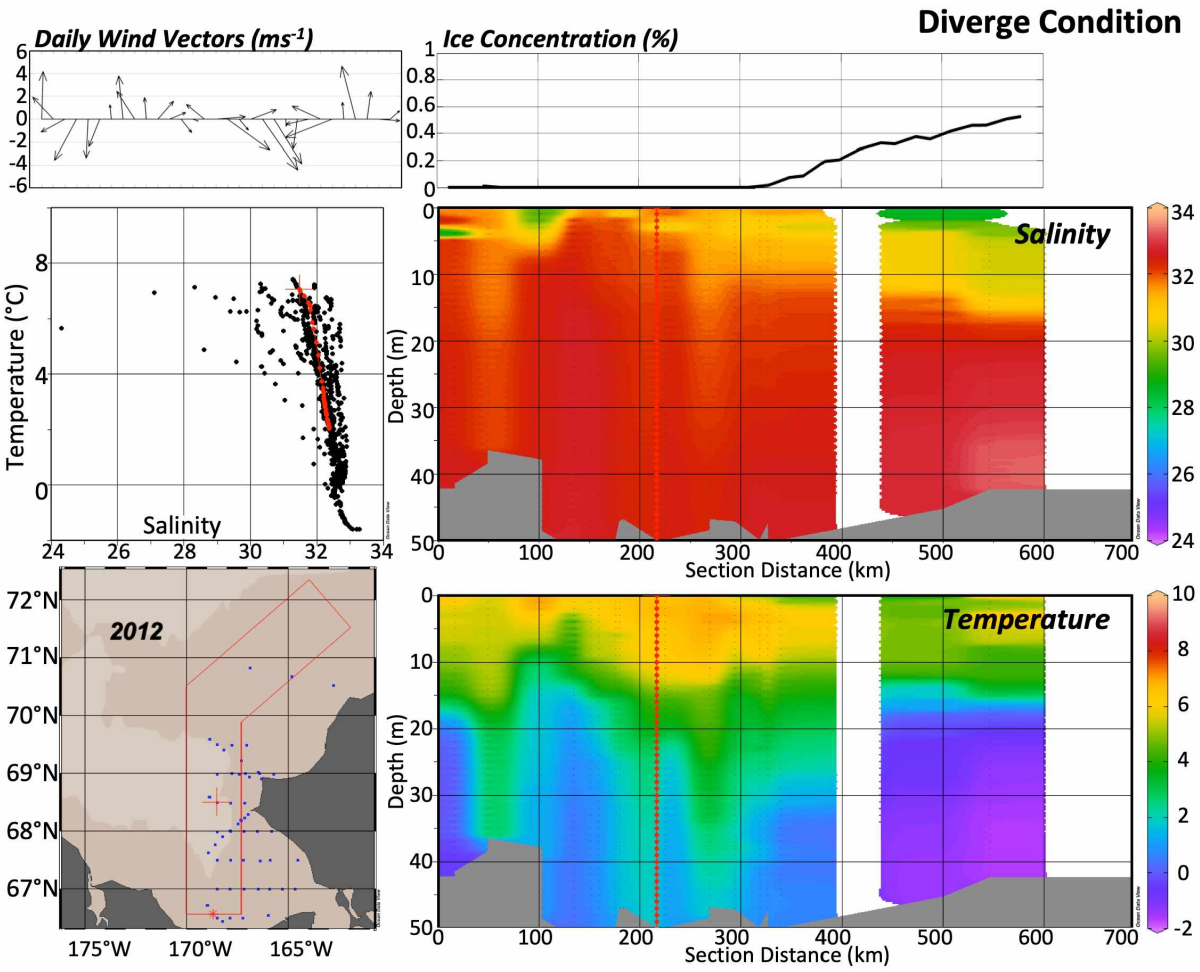

Figure 11. Hydrographic transects (right middle and right lower) and a T-S diagram (left middle) evaluated from CTD casts across the Central Channel within the outlined red polygon (lower left) in the 2012 summer (June 15 – August 15). The ice concentration (upper right) is the July 2012 average evaluated from the NSIDC NASA team algorithm along 169°W. Daily wind vectors shown in upper-left corner are from the North American Regional Reanalysis for July 2012.

Reference

Aagaard, K., Weingartner, T. J., Danielson, S. L., Woodgate, R. A., Johnson, G. C., & Whitledge, T. E. (2006). Some controls on flow and salinity in Bering Strait. *Geophysical Research Letters*, 33(19).

Carmack, E., & Chapman, D. C. (2003). Wind-driven shelf/basin exchange on an Arctic shelf: The joint roles of ice cover extent and shelf-break bathymetry. *Geophysical Research Letters*, 30(14).

Cavalieri, D. J., Parkinson, C. L., Gloersen, P., & Zwally, H. J. (1996). Sea ice concentrations from Nimbus-7 SMMR and DMSP SSM/I-SSMIS passive microwave data. *Boulder, Colorado USA: NASA DAAC at the National Snow and Ice Data Center*, 25.

Danielson, S. L., Weingartner, T. J., Hedstrom, K. S., Aagaard, K., Woodgate, R., Curchitser, E., & Stabeno, P. J. (2014). Coupled wind-forced controls of the Bering–Chukchi shelf circulation and the Bering Strait throughflow: Ekman transport, continental shelf waves, and variations of the Pacific–Arctic sea surface height gradient. *Progress in Oceanography*, 125, 40-61.

Durski, S. M., Glenn, S. M., & Haidvogel, D. B. (2004). Vertical mixing schemes in the coastal ocean: Comparison of the level 2.5 Mellor-Yamada scheme with an enhanced version of the K profile parameterization. *Journal of Geophysical Research: Oceans*, 109(C1).

Galperin, B., Kantha, L. H., Hassid, S., & Rosati, A. (1988). A quasi-equilibrium turbulent energy model for geophysical flows. *Journal of the Atmospheric Sciences*, 45(1), 55-62.

Haine, T. W., & Marshall, J. (1998). Gravitational, symmetric, and baroclinic instability of the ocean mixed layer. *Journal of Physical Oceanography*, 28(4), 634-658.

Hedstrom, K. (2018). Technical Manual for a Coupled Sea-Ice/Ocean Circulation Model (Version 5). *U.S. Dept. of the Interior, Bureau of Ocean Energy Management, Alaska OCS Region. OCS Study BOEM* 2018-007. 182 pp.

Kantha, L. H., & Clayson, C. A. (1994). An improved mixed layer model for geophysical applications. *Journal of Geophysical Research: Oceans*, 99(C12), 25235-25266.

Kasper, J. L., & Weingartner, T. J. (2015). The spreading of a buoyant plume beneath a landfast ice cover. *Journal of Physical Oceanography*, 45(2), 478-494.

Linders, J., Pickart, R. S., Björk, G., & Moore, G. W. K. (2017). On the nature and origin of water masses in Herald Canyon, Chukchi Sea: Synoptic surveys in summer 2004, 2008, and 2009. *Progress in Oceanography*, *159*, 99-114.

Lu, K., Weingartner, T., Danielson, S., Winsor, P., Dobbins, E., Martini, K., & Statscewich, H. (2015). Lateral mixing across ice meltwater fronts of the Chukchi Sea shelf. *Geophysical Research Letters*, 42(16), 6754-6761.

Lu, K., Danielson, S., Hedstrom, K., & Weingartner, T. (in review, 2019). Assessing the role of oceanic heat fluxes on ice ablation on the Chukchi Sea Shelf. *Progress in Oceanography*.

Mellor, G. L., & Yamada, T. (1982). Development of a turbulence closure model for geophysical fluid problems. *Reviews of Geophysics*, 20(4), 851-875.

Mesinger, F., DiMego, G., Kalnay, E., Mitchell, K., Shafran, P. C., Ebisuzaki, W., ... & Ek, M. B. (2006). North American regional reanalysis. *Bulletin of the American Meteorological Society*, 87(3), 343-360.

Ogi, M., Yamazaki, K., & Wallace, J. M. (2010). Influence of winter and summer surface wind anomalies on summer Arctic sea ice extent. *Geophysical Research Letters*, 37(7).

Okkonen, S., Ashjian, C., Campbell, R. G., & Alatalo, P. (2018). The encoding of wind forcing into the Pacific-Arctic pressure head, Chukchi Sea ice retreat and late-summer Barrow Canyon water masses. *Deep Sea Research Part II: Topical Studies in Oceanography*.

Onarheim, I. H., Eldevik, T., Smedsrud, L. H., & Stroeve, J. C. (2018). Seasonal and regional manifestation of Arctic sea ice loss. *Journal of Climate*, 31(12), 4917-4932.

Rudels, B. (2015). Arctic Ocean circulation, processes and water masses: A description of observations and ideas with focus on the period prior to the International Polar Year 2007–2009. *Progress in Oceanography*, 132, 22-67.

Serreze, M. C., Crawford, A. D., Stroeve, J. C., Barrett, A. P., & Woodgate, R. A. (2016). Variability, trends, and predictability of seasonal sea ice retreat and advance in the Chukchi Sea. *Journal of Geophysical Research: Oceans*, 121(10), 7308-7325.

Shuchman, R. A., Onstott, R. G., Johannessen, O. M., Sandven, S., & Johannessen, J. A. (2004). Processes at the ice edge: The Arctic. *Synthetic Aperture Radar marine user's manual*, 373-395.

Spall, M. A., & Thomas, L. N. (2016). Downfront winds over buoyant coastal plumes. *Journal of Physical Oceanography*, 46(10), 3139-3154.

Stabeno, P., Kachel, N., Ladd, C., & Woodgate, R. (2018). Flow patterns in the eastern Chukchi Sea: 2010–2015. *Journal of Geophysical Research: Oceans*, 123(2), 1177-1195.

Steele, M., & Ermold, W. (2015). Loitering of the retreating sea ice edge in the Arctic Seas. *Journal of Geophysical Research: Oceans*, *120*(12), 7699-7721.

Stroeve, J. C., Jenouvrier, S., Campbell, G. G., Barbraud, C., & Delord, K. (2016). Mapping and assessing variability in the Antarctic marginal ice zone, pack ice and coastal polynyas in two sea ice algorithms with implications on breeding success of snow petrels. *The Cryosphere*, 10(4), 1823-1843.

Thomas, L. N. (2008). Formation of intrathermocline eddies at ocean fronts by wind-driven destruction of potential vorticity. *Dynamics of Atmospheres and Oceans*, 45(3-4), 252-273.

Watanabe, E., & Ogi, M. (2013). How does Arctic summer wind modulate sea ice-ocean heat balance in the Canada Basin?. *Geophysical Research Letters*, 40(8), 1569-1574.

Weingartner, T., Dobbins, E., Danielson, S., Winsor, P., Potter, R., & Statscewich, H. (2013). Hydrographic variability over the northeastern Chukchi Sea shelf in summer-fall 2008–2010. *Continental Shelf Research*, *67*, 5-22.

Weingartner, T., Fang, Y. C., Winsor, P., Dobbins, E., Potter, R., Statscewich, H., ... & Borg, K. (2017). The summer hydrographic structure of the Hanna Shoal region on the northeastern Chukchi Sea shelf: 2011–2013. *Deep Sea Research Part II: Topical Studies in Oceanography*, 144, 6-20.

Williams, W. J., & Carmack, E. C. (2008). Combined effect of wind-forcing and isobath divergence on upwelling at Cape Bathurst, Beaufort Sea. *Journal of Marine Research*, 66(5), 645-663.

Wood, K. R., Overland, J. E., Salo, S. A., Bond, N. A., Williams, W. J., & Dong, X. (2013). Is there a “new normal” climate in the Beaufort Sea?. *Polar Research*, 32(1), 19552.

Wood, K. R., Bond, N. A., Danielson, S. L., Overland, J. E., Salo, S. A., Stabeno, P. J., & Whitefield, J. (2015). A decade of environmental change in the Pacific Arctic region. *Progress in Oceanography*, 136, 12-31.

Woodgate, R. A., Aagaard, K., & Weingartner, T. J. (2005). A year in the physical oceanography of the Chukchi Sea: Moored measurements from autumn 1990–1991. *Deep Sea Research Part II: Topical Studies in Oceanography*, 52(24-26), 3116-3149.

Woodgate, R. A. (2018). Increases in the Pacific inflow to the Arctic from 1990 to 2015, and insights into seasonal trends and driving mechanisms from year-round Bering Strait mooring data. *Progress in Oceanography*, 160, 124-154.

Conclusions

Three studies in this thesis are centered on the eddy transport induced by baroclinic instabilities in the vicinity of the Chukchi Sea ice edge. The intrapycnocline eddies transport heat of BSW laterally northward into the Arctic Ocean, the heat transport is comparable to net solar heat flux to ice melt and represents more than 30% of the total oceanic heat transport in the lateral direction. Eddy transport is strongly related to the frontal stratifications caused by Bering Strait Inflow. However, there is no remarkable enhancement of eddy transport by wind forces, because the change of bulk density on front and front layer thickness made by winds tend to cancel each other.

Another vital effect of eddy transport is its influence on the vertical dynamics. Vertical stretching and squeezing of eddies provide the energy for cross-isobath heat transport, and this is especially important for the Chukchi Shelf where the circulations are bathymetric-steered. These motions help spread nutrients and heat and expand the ice melt area. Intrapycnocline eddies are also an important source of heat and nutrients vertically as they are transported from subsurface BSW/WW into the surface mixed layer beneath ice. Heat transported vertically by eddies along the Chukchi ice edge is ~1 TW from subsurface BSW to MW beneath ice and ~0.3 TW from the surface MW to the ice. This constantly vertical heat transport buffers cooling by the atmosphere after summer and delays ice formation in fall months.

Vertical transport is well-correlated to eddy transport in the absence of wind. While under the effect of wind, we find no remarkable variation of eddy transport, although we do note a significant increase of vertical transport with a positive northerly wind component due to surface Ekman divergence between the ice edge and the Bering Strait inflow. The intensification of vertical mixing is may benefit summer plankton blooms by bringing nutrients toward the

euphotic zone following ice breakup. In addition, the salt blended upward from BSW/WW into the MW diminishes the strongly stratified barrier formed by fresh but nutrient-poor MW pool. The response of vertical mixing intensification to wind forces may persist after strong wind event for few days, and regardless of wind directions in the ice-free ocean, more hydrographic observations and model analyses are necessary to further investigate this important mechanism.

Intrapycnocline eddies on Chukchi Shelf are driven by fronts that bridge the shelf waters made up of Bering Strait inflow and winter waters below the sea ice. These play a key role to ice retreat on Chukchi shelf by both thermodynamic and dynamic processes. More than 70% of the heat used to melt the ice edge is transported by BSW. The magnitude of heat transport is influenced by BSW stratification, which is determined by Bering Strait inflow salinity and distance from front to ice edge; this is affected by the regional wind field. In our model studies, the Bering Strait inflow is invulnerable to winds. Wind stress moves ice directly and accelerates the northward ice advection, but has only a weak impact on the modeled lateral transport of the Bering Strait inflow. In strong wind events, the structure change of BSW at the front is due to surface convergence/divergence at the ice edge and not by direct wind mixing. Wind-induced surface divergence lowers sea level around the ice edge and so might increase the pressure gradient and magnify inflow discharge. Nevertheless, in contrast with the real ocean and well-know relations between winds and the Bering Strait through-flow (e.g., Woodgate et al., 2010; Danielson et al., 2014), correlation between inflow discharge changes and short-term regional wind adjustments is not significant in this study.

This research has identified dynamically important frontal zones, the Melt Water Transition Zone (MWTZ) and the Shelf Water Transition Zone (SWTZ), based on their unique ice conditions, hydrographic characteristics and dynamics. These zones represent the

oceanographic equivalent of the Marginal Ice Zone (MIZ). Their characteristics are found to vary with scales that set by density gradients.

We expect more research exploring the particular ecosystems corresponding to each oceanographic zone, including studies about the dependence of specific species to the physical processes in these zones. From the point of view of nutrient dynamics, intrapycnocline eddies can advect dissolved inorganic nutrients laterally and vertically, potentially feeding the euphotic zone with nutrients from below the critical depth. For passively drifting and buoyant eggs, plankton and larvae, frontal zones can behave as aggregation points because subducting plumes of BSW would tend to leave positively buoyant particles near the front. Other ongoing research using ROMS modeling (Vestfals, 2019) has identified the ice edge as a likely location for the accumulation of Arctic Cod larvae. From an evolutionary standpoint, this type of behavior makes sense as these animals are believed to remain near the surface in cool ice melt conditions. This series of investigations provides a dynamical context for the better understanding of this keystone Arctic organism.

Future Perspectives

Although transports across the Chukchi Shelf are dominated by bathymetry, frontal processes occur near the surface and are affected by the relative layer thickness on fronts rather than total water depth. This indicates the influences of inflow properties to eddy transport evaluated in our studies should be able to apply to the other basins, as a connection between subarctic inflow and sea ice cover. To validate this generality and assess the sensitivity to water depths, model tests with different types of bathymetry such as shoals, canyons and continental slope regions within and beyond the Chukchi Sea are necessary.

The Alaskan Coastal Current (ACC) is another branch of Pacific Water making significant contributions of heat to the Arctic Ocean on Chukchi Shelf. The east land boundary and associated boundary current are not included in our models. However, both the fresh water of the ACC and continental boundary alter the surface pressure gradient and modify the pathway of eastward eddy transport from Central Channel. The influences of boundary currents to eddy dynamics in vicinity is also an important and interesting topic for further study.

Several studies show that the bidirectional influences between pressure system and sea ice condition (Wu and Wang, 2002; Inoue et al., 2012). Our study assesses the importance of local wind effects on ice distribution in the ice-ocean model, giving atmospheric condition as external forces; feedback from ice to weather patterns is not integrated and remains unclear, although some recent studies have linked increasing Chukchi sea temperature with reduced ice cover and subsequent warm southerly wind events over the Bering/Chukchi Seas (Tachibana et al., 2019). Under climate change, with more open water area and increasing sea surface temperature, we may expect to see more strong wind events fed by energy from ocean (Lin et al., 2013; D'Asaro et al., 2014) and further impact on ice retreat. Coupling our model with atmospheric model and tracking the change of surface moisture, winds and corresponding pressure system affected by ice variations is critical to long-term ice forecast and weather teleconnections to subpolar regions.

Reference

Danielson, S. L., Weingartner, T. J., Hedstrom, K. S., Aagaard, K., Woodgate, R., Curchitser, E., & Stabeno, P. J. (2014). Coupled wind-forced controls of the Bering–Chukchi shelf circulation and the Bering Strait throughflow: Ekman transport, continental shelf waves, and variations of the Pacific–Arctic sea surface height gradient. *Progress in Oceanography*, 125, 40-61.

D'Asaro, E. A., Black, P. G., Centurioni, L. R., Chang, Y. T., Chen, S. S., Foster, R. C., ... & Lin, I. I. (2014). Impact of typhoons on the ocean in the Pacific. *Bulletin of the American Meteorological Society*, 95(9), 1405-1418.

Inoue, J., Hori, M. E., & Takaya, K. (2012). The role of Barents Sea ice in the wintertime cyclone track and emergence of a warm-Arctic cold-Siberian anomaly. Journal of Climate, 25(7), 2561-2568. Woodgate, R. A., Weingartner, T., & Lindsay, R. (2010). The 2007 Bering Strait oceanic heat flux and anomalous Arctic sea ice retreat. *Geophysical Research Letters*, 37(1).

Lin, I. I., Black, P., Price, J. F., Yang, C. Y., Chen, S. S., Lien, C. C., ... & D'Asaro, E. A. (2013). An ocean coupling potential intensity index for tropical cyclones. *Geophysical Research Letters*, 40(9), 1878-1882.

Tachibana, Y., Komatsu, K. K., Alexeev, V. A., Cai, L., & Ando, Y. (2019). Warm hole in Pacific Arctic sea ice cover forced mid-latitude Northern Hemisphere cooling during winter 2017–18. *Scientific Reports*, 9(1), 5567.

Vestfals, C. (2019). Modeling growth and transport of Arctic cod and saffron cod early life stages in the Pacific Arctic under variable climate forcing. *Alaska Marine Science Symposium*.

Woodgate, R. A., Weingartner, T., & Lindsay, R. (2010). The 2007 Bering Strait oceanic heat flux and anomalous Arctic sea ice retreat. *Geophysical Research Letters*, 37(1).

Wu, B., & Wang, J. (2002). Winter Arctic oscillation, Siberian high and East Asian winter monsoon. *Geophysical Research Letters*, 29(19), 3-1.